DEVCOM DAC-TR-2024-031
March 2024

The Impact and Injury Response of Male and Female PMHS, Hybrid III 50th Percentile ATDs, and WIAMan under Blast-Induced Accelerative Loading

by Warren N. Hardy, David Boyle, Davide Ceritano, Amanda Agnew, John H. Bolte IV, Kerry A. Danelson, Hollie A. Pietsch, and Kathryn L. Loftis

DISCLAIMER

The findings in this report are not to be construed as an official Department of the Army position unless so specified by other official documentation.

WARNING

Information and data contained in this document are based on the input available at the time of preparation.

TRADE NAMES

The use of trade names in this report does not constitute an official endorsement or approval of the use of such commercial hardware or software. The report may not be cited for purposes of advertisement.

DEVCOM DAC-TR-2024-031
March 2024

The Impact and Injury Response of Male and Female PMHS, Hybrid III 50th Percentile ATDs, and WIAMan under Blast-Induced Accelerative Loading

by Warren N. Hardy, David Boyle, and Davide Ceritano
Center for Injury Biomechanics, Virginia Tech

Amanda Agnew and John H. Bolte IV
Injury Biomechanics Research Center, The Ohio State University

Kerry A. Danelson
Dept. of Orthopaedic Surgery, Wake Forest School of Medicine

Hollie A. Pietsch
Wayne State University, Ph.D. candidate

Kathryn L. Loftis
DEVCOM Analysis Center

REPORT DOCUMENTATION PAGE

1. REPORT DATE	2. REPORT TYPE	3. DATES COVERED	
		START DATE	END DATE
March 2024	Technical Report	October 2017	July 2019

4. TITLE AND SUBTITLE
The Impact and Injury Response of Male and Female PMHS, Hybrid III 50th Percentile ATDs, and WIAMan under Blast-Induced Accelerative Loading

5a. CONTRACT NUMBER	5b. GRANT NUMBER	5c. PROGRAM ELEMENT NUMBER
W911NF-14-2-0023		
5d. PROJECT NUMBER	**5e. TASK NUMBER**	**5f. WORK UNIT NUMBER**

6. AUTHOR(S)
Warren N. Hardy, David Boyle, Davide Ceritano, Amanda Agnew, John H. Bolte IV, Kerry A. Danelson, Hollie A. Pietsch, and Kathryn L. Loftis

7. PERFORMING ORGANIZATION NAME(S) AND ADDRESS(ES)
Director
DEVCOM Analysis Center
6896 Mauchly Street
Aberdeen Proving Ground, MD 21005

8. PERFORMING ORGANIZATION REPORT NUMBER
DEVCOM DAC-TR-2024-031

9. SPONSORING/MONITORING AGENCY NAME(S) AND ADDRESS(ES)	10. SPONSOR/MONITOR'S ACRONYM(S)	11. SPONSOR/MONITOR'S REPORT NUMBER(S)

12. DISTRIBUTION/AVAILABILITY STATEMENT
DISTRIBUTION STATEMENT A. Approved for public release: distribution unlimited.

13. SUPPLEMENTARY NOTES

14. ABSTRACT
The Warrior Injury Assessment Manikin (WIAMan), which is representative of a 50th percentile male, is the only anthropomorphic test device (ATD) that is designed to evaluate injury patterns in under-body blast (UBB) conditions. The WIAMan ATD will aid in predicting the injuries sustained by Warfighters in theater and enable the development and implementation of improved vehicle systems and personal protective equipment. This work is being conducted in support of an Analysis of Alternatives to inform future decisions regarding implementation of a valid injury assessment capability for female Soldiers in the UBB environment (i.e., a separate female UBB ATD or the collection of the female biomechanics data needed to map the performance and injury prediction of the existing male ATD to that of the female). This work will determine the path forward for injury prediction and mitigation for the female Warfighter.

15. SUBJECT TERMS
Warrior Injury Assessment Manikin, WIAMan, female, injury risk, underbody blast, injury biomechanics

16. SECURITY CLASSIFICATION OF:			17. LIMITATION OF ABSTRACT	18. NUMBER OF PAGES
a. REPORT	b. ABSTRACT	C. THIS PAGE		
UNCLASSIFIED	UNCLASSIFIED	UNCLASSIFIED	UU	92

19a. NAME OF RESPONSIBLE PERSON	19b. PHONE NUMBER *(Include area code)*
Kathryn Loftis	(410) 306-0344

STANDARD FORM 298 (REV. 5/2020)
Prescribed by ANSI Std. Z39.18

(U) Table of Contents

List of Figures

List of Figures

List of Figures

List of Figures

List of Figures

List of Tables

Executive Summary

The objective of the Third Annual Program Plan (APP3) was to fill in knowledge gaps related to the biomechanical responses of male and female postmortem human surrogates (PMHSs) at the structure level and to define injury mechanism and tolerance differences between males and females in the high-rate vertical-loading environment. APP3 covers the structural-level testing portion of an overall Analysis of Alternatives. These tests collected responses of the foot and ankle (calcaneus-talus-tibia complex), lumbar spine (intact vertebral segments, L2-L4), and sacrum (costal elements and auricular surfaces/SI joints) under axial loading conditions. These tests used a unique cam device to provide repeatable loading and high-speed X-ray to observe time of fracture and fracture propagation. The responses of the tibia to lateral loading via indenter were also collected in support of a bone condition mapping effort. Specimens were drawn from nine 50th percentile male (50M) PMHSs, six 75th percentile female (75F) PMHSs, and five 5th percentile female (5F) PMHSs.

This annual report focuses on five primary efforts:

- Foot/ankle cam testing using high-speed X-ray and data processing/analysis
- Lumbar spine cam testing using high-speed X-ray and processing/analysis
- Tibia drop-tower testing and processing/analysis
- Sacrum/pelvis cam testing using high-speed X-ray and processing/analysis
- Rib testing and processing/analysis

All test results indicate, with statistical significance, the differences in tolerance and loading response between males and females. The general trends (descriptive statistics) for all testing are the same: damage thresholds for 50M are greater than for 75F, which are greater than for 5F. For some structures, the 75F responses are closer to those of the 50M than the 5F. In some cases, the damage patterns differ between the three groups. The experimental repeatability designed into these tests and testing apparatus produced minimal experimental variance, allowing trends and significance to be established using relatively few specimens.

These results show that uniform functions for injury risk prediction and common injury assessment reference values cannot be applied across the sexes, nor within the two female anthropometry categories examined in this study. For additional background on the tests and analyses completed, see DEVCOM DAC-TR-2024-030.[1]

[1] Cristino, D. M., Danelson, K. A., Hardy, W. N., Bolte IV, J. H., Crawford, D. *The Impact and Injury Response of Female and Male PMHS, Hybrid III 50th and 5th Percentile ATDs, and WIAMan under Blast-Induced Accelerative Loading* (Report No.: DEVCOM DAC-TR-2024-030). DEVCOM Analysis Center; 2024.

1. INTRODUCTION

The overall purpose of these tests is to collect responses of both female and male postmortem human surrogates (PMHS) under various high-rate, vertical-loading conditions using a cam loading mechanism. The intent of these experiments is to investigate how fracture propagates under vertical-loading condition. The design of the current test fixture allows for a large amount of energy transfer from the system to the isolated body region. The data from these tests will provide information on failure loads and fracture patterns. The objective of the current phase of the research effort is to fill in knowledge gaps related to the biomechanical responses of female and male PMHS and to define response envelopes for females in the under-body blast (UBB) environment. These comparisons, in combination with whole body testing, will inform decisions regarding the need for a new, separate, female anthropomorphic test device (ATD) for use in the UBB environment versus the potential ability to map female injury prediction to the response of the male Warrior Injury Assessment Manikin (WIAMan). The objectives covered in this report include the following:

- Collect response data for female and male PMHSs.
- Characterize the response of the foot/ankle, pelvis, and lumbar spine.
- Determine the extent of, and timing associated with, the damage sustained by the PMHS.
- Determine whether any differences in response are as a result of size, shape, anatomy, and/or tolerance.

2. TESTING AND SPECIMEN SUMMARY

The (right) foot/ankle, lumbar spine, and sacrum/pelvis loading tests were conducted using a cam loading mechanism. The (left) tibia impact tests were conducted using a drop-tower fixture. The cam mechanism (Figure 1) was designed to deliver 25.4-mm stroke reaching 5 m/s within 10 ms. The high-speed x-ray images were typically captured using a 16-bit monochrome video camera operated at 2000 fps with 20-µs exposure. A minimum of 1200-pixel horizontal resolution was used.

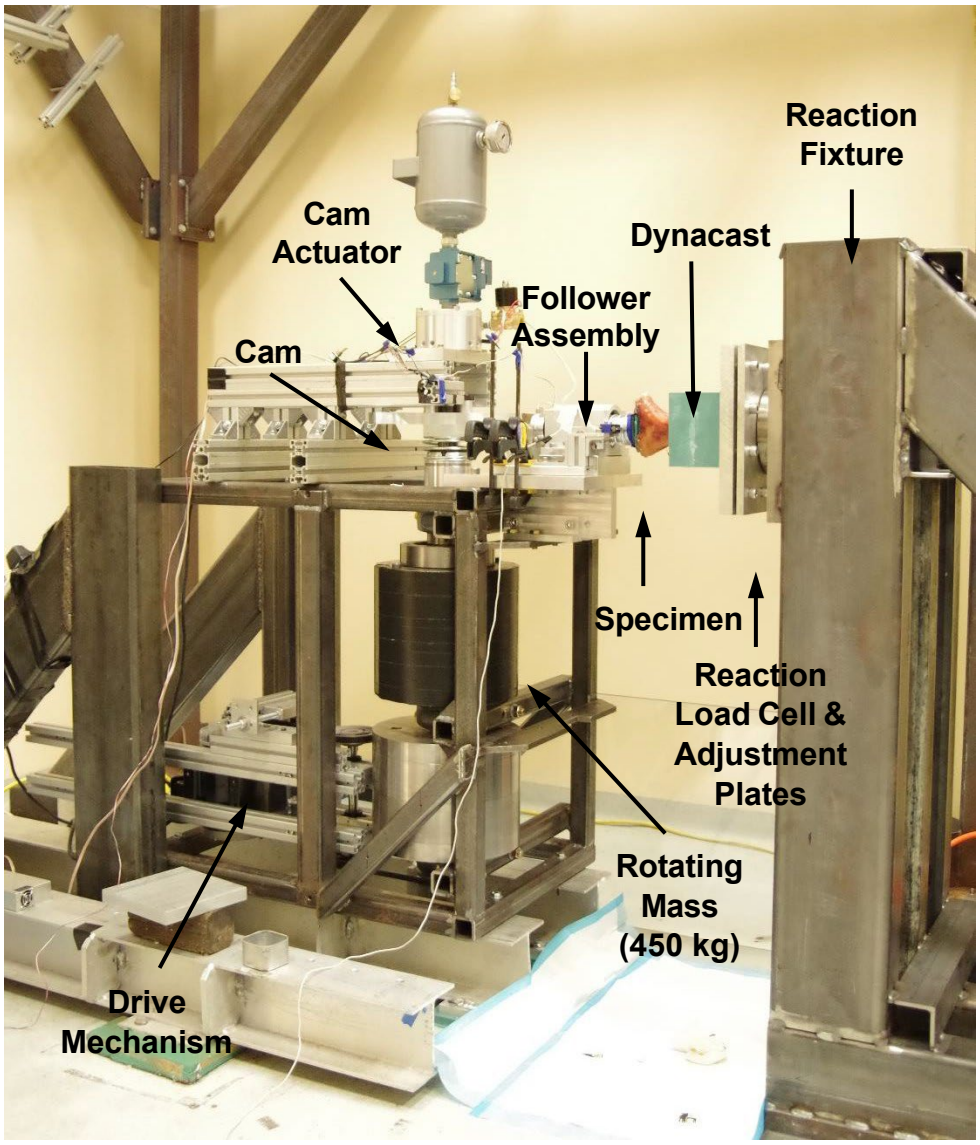

Figure 1. The cam loading mechanism used for foot/ankle, lumbar spine, and sacrum/pelvis testing

Table 1 summarizes the specimens for which the test data have been processed and analyzed for the ankle, lumbar spine, pelvis, and tibia. An “X” indicates data that are provided and reviewed herein. A blank entry denotes pending results. A “-” indicates an unavailable specimen (found to be unsuitable during screening). All lumbar spines were used in cam testing, so no additional individual vertebral bodies were tested using the drop tower. The 50th percentile males are denoted by “50M,” while 75th and 5th percentile females are denoted by “75F” and “5F,” respectively. There were 18 right foot/ankle specimens tested, in addition to 15 lumber spine segments, 13 sacrum/pelvis preparations, and 20 left tibia samples. Not all tests produced usable results. Visual examples of exclusionary events are provided in Appendix A.

Table 1. Summary of testing and processed/analyzed results

Specimen		X-ray/Cam			Drop Tower	
Category %ile-M/F	**PMHS #**	**Right Ankle**	**Lumbar Spine (L4-L2)**	**Pelvis**	**Left Tibia**	**VB (L4)**
	7409	X	X	-	X	-
	7575	X	X	X	X	-
	7542	X	X	X	X	-
	7805	X	-	-	X	-
50M	7406	X	X	X	X	-
	7849	X	X	X	X	-
	9584M	TRR4	-	-	TRR1	TRR3
	7654	-	X	X	X	-
	7282	-	X	X	X	-
	7469	X	X	-	X	-
	7380	X	X	X	Bad test	-
75F	7618	X	-	X	X	-
	7058	X	X	-	X	-
	7834	X	X	X	X	-
	2366	X	TRR6	-	X	-
	7607	X	X	X	X	-
	7630	X	-	X	X	-
5F	0509	TRR5	-	-	TRR2	-
	7727	X	X	X	X	-
	L7034	X	X	X	X	-

Note: An “X” indicates data that are provided and reviewed herein. A blank entry denotes pending results. A “-” indicates an unavailable specimen (found to be unsuitable during screening).

For ease of inspection, all load curves are presented herein with the major peaks being positive. This polarity is opposite to the SAE J211 standard and Western Regional Strain Gage signal convention, for which cranially directed loading and axial compression are negative.

3. FOOT/ANKLE CAM TESTING USING HIGH-SPEED X-RAY

There are now 17 usable ankle tests (excluding one failed Test Readiness Review [TRR] test). Six specimens were 50M, six were 75F, and five were 5F. The calcaneus was fractured in all cases. The talus was fractured twice resulting in substantial disruptions of the bone. Other tests resulted in minor talus damage. One pilon fracture was observed. Figure 2 shows a representative foot and ankle from PMHS7469 installed in the cam device prior to testing. Figure 3 shows the right calcaneus fracture of PMHS7805 as it progresses and a right talus fracture developing after the onset of calcaneus fracture for PMHS7630.

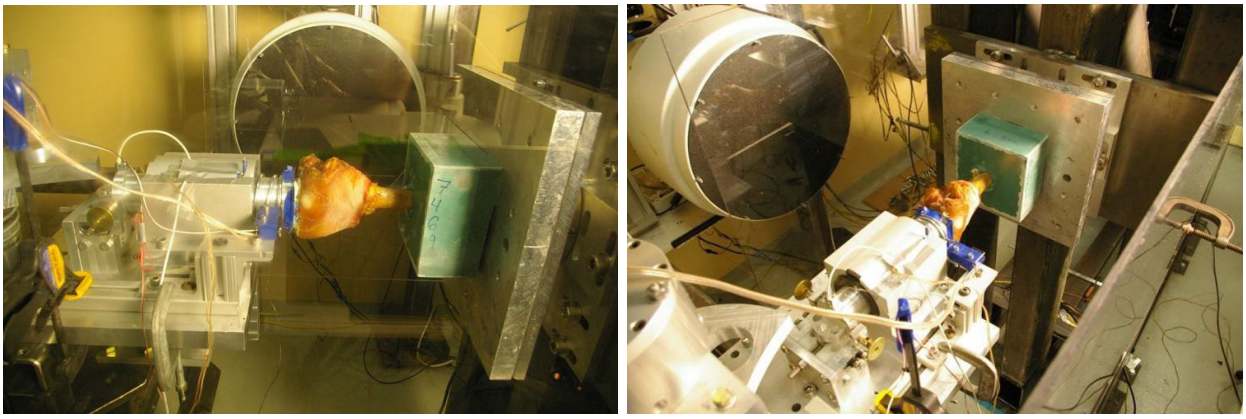

Figure 2. The right ankle preparation of PMHS7469 installed in the cam/X-ray apparatus

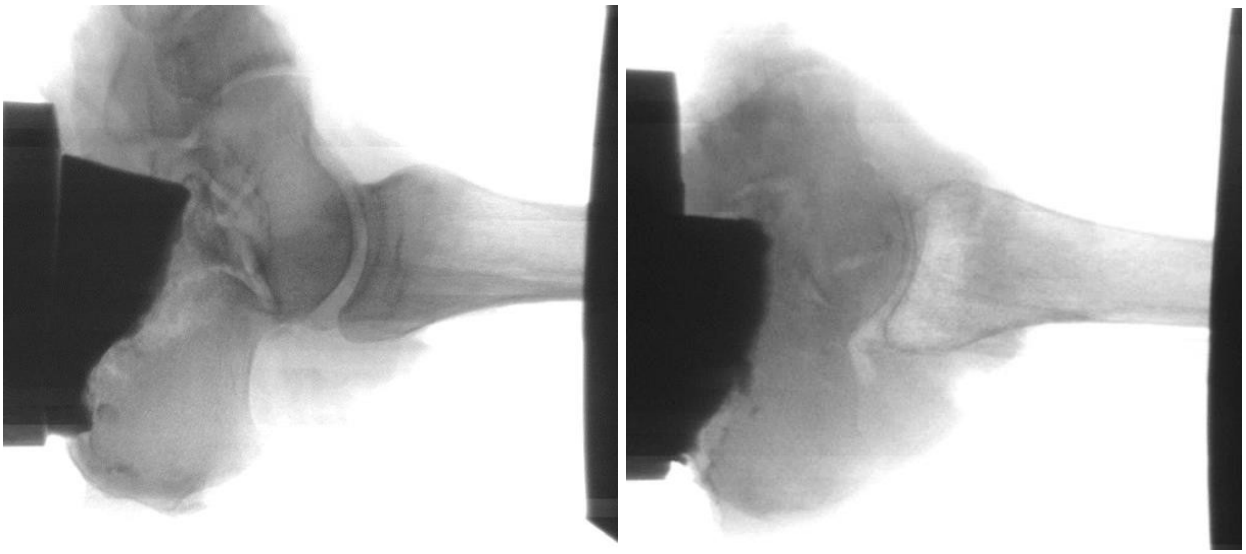

Figure 3. Right calcaneus fracture of PMHS7805 in progress (left) and a right talus fracture developing after the onset of calcaneus fracture for PMHS7630 (right)

Figure 4 shows the load-time histories for 50M PMHS ankle testing. The loads follow similar patterns and are tightly grouped. Figure 5 shows the load-time histories for 75F PMHS ankle testing. Again, all traces show similar shapes and durations. However, the range between the calcaneus fracture loads is larger than that of the 50M. As noted in previous reporting, PMHS2366 experienced a talus fracture (first peak) prior to the calcaneus fracture (and in the absence of a distal tibia fracture), obfuscating the determination of the calcaneus fracture load. Data from this test are not included in the statistical analyses. Figure 6 shows the load-time histories for 5F PMHS ankle testing. These traces exhibit the least degree of between-test similarity and the most variation in calcaneus fracture load for the three anthropometric categories/groups examined as part of this study. PMHS7630 experienced a late talus fracture, while the calcaneus was continuing to crush. Data from this test are included in the statistics.

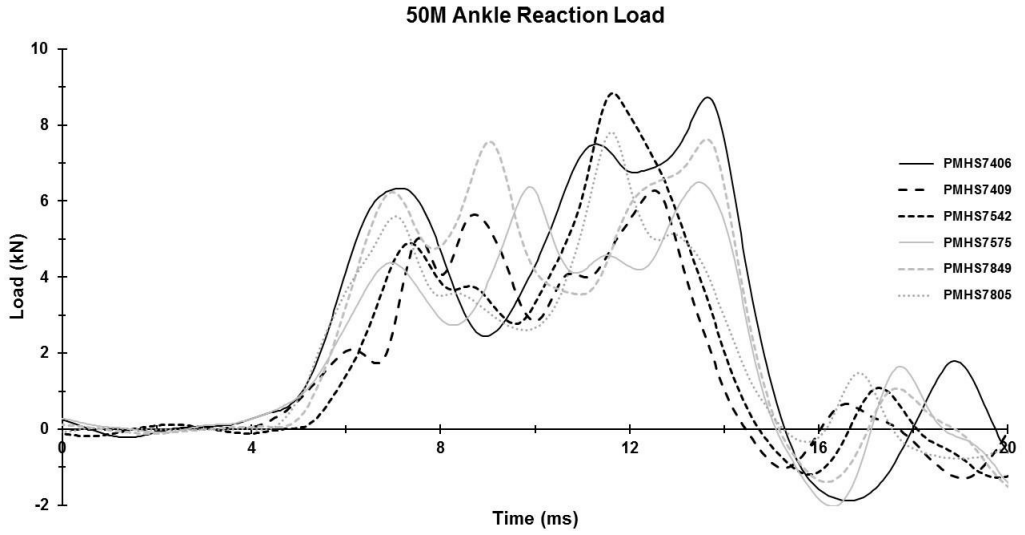

Figure 4. 50th percentile male (50M) reaction loads from cam testing of right ankles

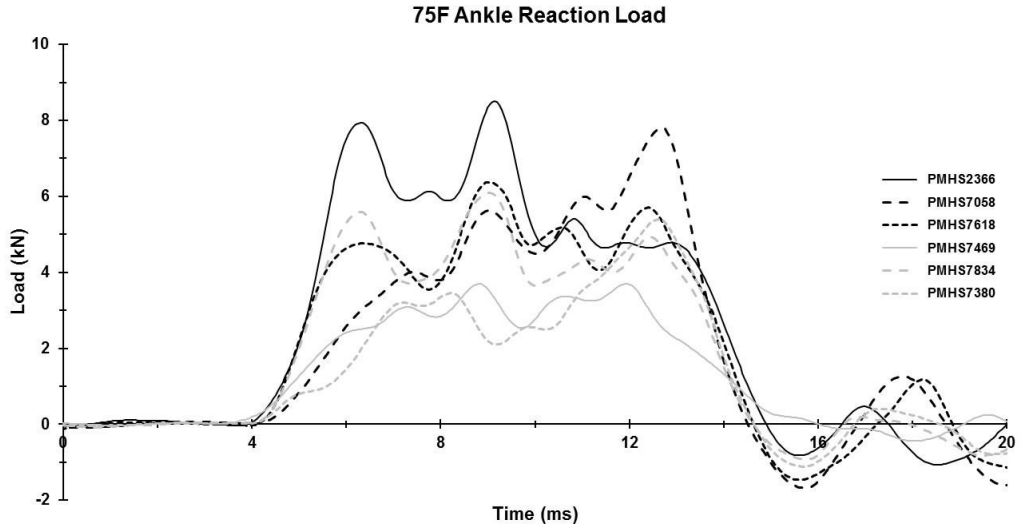

Figure 5. 75th percentile female (75F) reaction loads from cam testing of right ankles

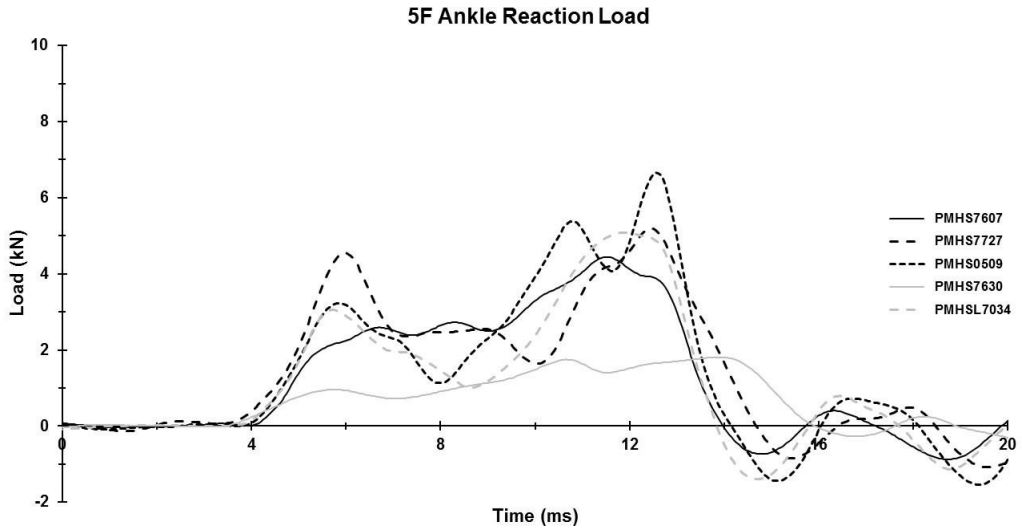

Figure 6. 5th percentile female (5F) reaction loads from cam testing of right ankles

Table 2 catalogs the calcaneus fracture loads for all ankle tests. The onset of fracture is determined by inspection of the high-speed X-ray images. All data are Channel Frequency Class 600 Hz.

Table 2. Summary of calcaneus fracture loads from ankle testing using the cam device

50M		75F		5F	
PMHS #	**Fx Load (N)**	**PMHS #**	**Fx Load (N)**	**PMHS #**	**Fx Load (N)**
7409	5,032	7469	3,088	7607	2,589
7575	4,372	7380	3,202	7630	960
7542	4,891	7618	4,763	0509	3,218
7805	5,578	7058	4,003	7727	4,544
7406	6,333	7834	5,593	L7034	3,055
7849	6,229	2366	8,504		
Average	**5,406**	**Average**	**4,130**	**Average**	**2,873**
Std. Dev.	**±780**	**Std. Dev.**	**±1,061**	**Std. Dev.**	**±1,293**

Note: The gray values are the fracture loads obtained after a conformation shift (slip) of the calcaneus. These numbers are inaccurate.

The 50M calcaneus fracture loads average 5.4 kN. The 75th percentile female calcaneus fracture loads average 4.1 kN. The 5th percentile female calcaneus fracture loads average 2.9 kN. The pilon fracture of PMHS7469 occurred at 3.7 kN. The early talus fracture of PMHS2366 (75F) occurred near 7.9 kN (during calcaneus fracture), while the late talus fracture of PMHS7630 (5F) occurred at 2 kN. The standard deviations are all relatively small, with the 50M data having the smallest (780 N).

The foot/ankle and concomitant damage response are cataloged in Appendix B.

Various statistics were evaluated to compare the calcaneus fracture loads for the three anthropometric groups. Table 3 summaries the statistical results (excluding PMHS2336). One-way analysis of variance (ANOVA) across the groups shows the differences between them are significant. Two other ANOVA approaches that do not assume similar standard deviations between the groups also showed the differences to be significant. Using unpaired Student's t-tests, both female groups were found to be different than the male group with statistically significance ($p < 0.05$). The small females are very significantly different (**) than the males. While the two female groups were not found to be statistically different, the important overall trend is that the 50M calcaneus fractures at higher load than the 75F calcaneus, which fractures at higher load than the 5F calcaneus. This trend is seen readily in Figure 7, which summarizes the means.

Table 3. Statistical analyses of the calcaneus fracture loads

Statistical Test		p		Notes
ANOVA	One-Way	0.0054	**	Assumes same std. dev.
	Brown-Forsythe	0.0091	**	Assumes different std. dev.
	Welch's	0.0156	*	
Unpaired Student's t-test	5F vs. 50M	0.0030	**	
	75F vs. 50M	0.0469	*	
	5F vs. 75F	0.1315	ns	Not significant

Note: * = significantly different; ** = very significantly different.

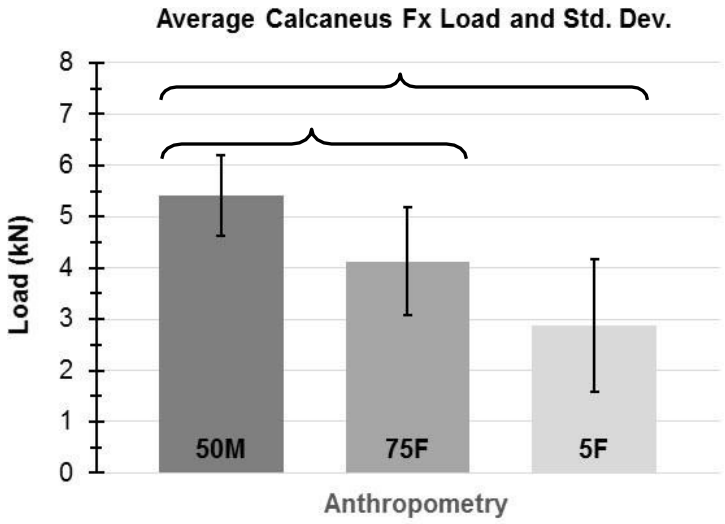

Figure 7. Comparison of averages and standard deviations for the ankle tests

4. LUMBAR SPINE CAM TESTING USING HIGH-SPEED X-RAY

Figure 8 shows the lumbar spine (exposed L4-L2) from PMHS7409 (50M) installed in the cam device. The cam strokes 25 mm, reaching 5 m/s in 10 ms. Results from 14 tests are presented. Figure 9 shows two representative fracture patterns observed during these tests. Figure 10 shows that the 50M lumbar spines' load responses are very similar in magnitude, shape, and duration. Figure 11 shows the same comparison for the 75F lumbar spines, as does Figure 12 for the 5F lumbar spines. Table 4 summarizes the lumbar spine fracture loads for the three anthropometries. The 50M specimens had the highest average fracture loads and standard deviations, while the 5F specimens had the lowest. The different fracture thresholds and fracture patterns suggest that the vertebral bodies and intervertebral discs of females respond differently to axial compression than do those of males.

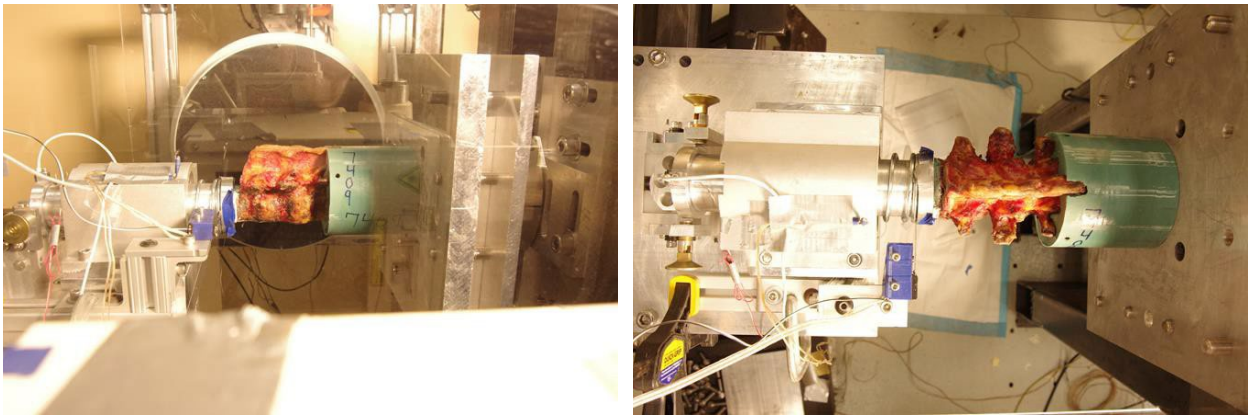

Figure 8. The lumbar spine preparation of PMHS7409 ready for cam/X-ray testing

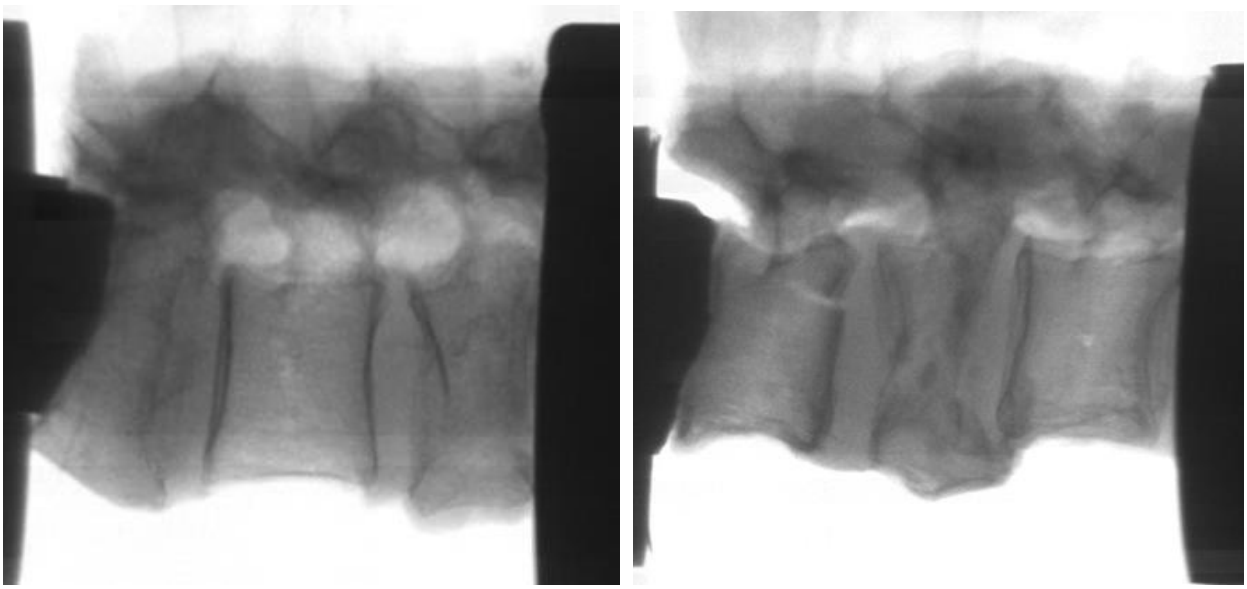

Figure 9. Compression burst fractures of L4 and L2 in PMHS7607 (left) and a compression/burst fracture of L3 in PMHS7849 (right), which also has an associated posterior element separation (pedicles) of L4

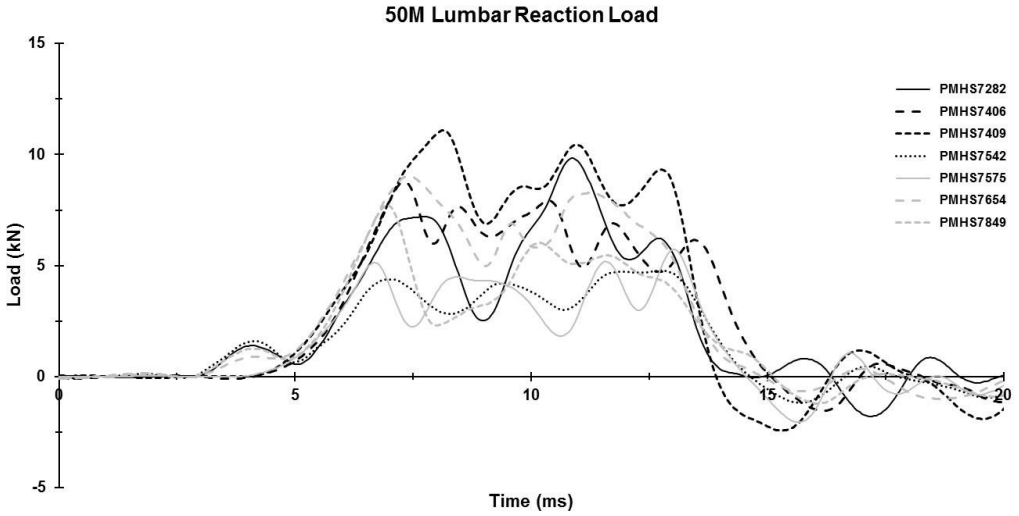

Figure 10. 50th percentile male (50M) reaction loads from cam testing of lumbar spines

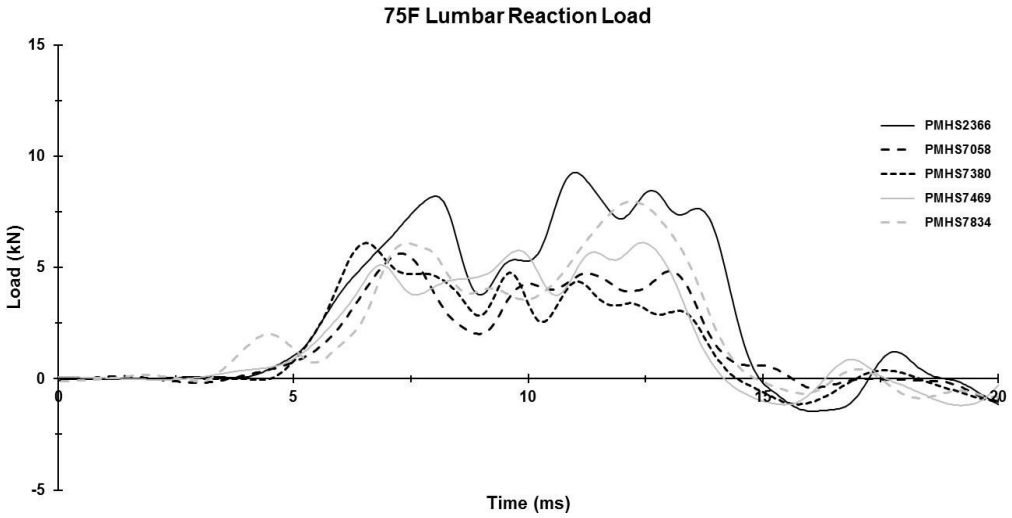

Figure 11. 75th percentile female (75F) reaction loads from cam testing of lumbar spines

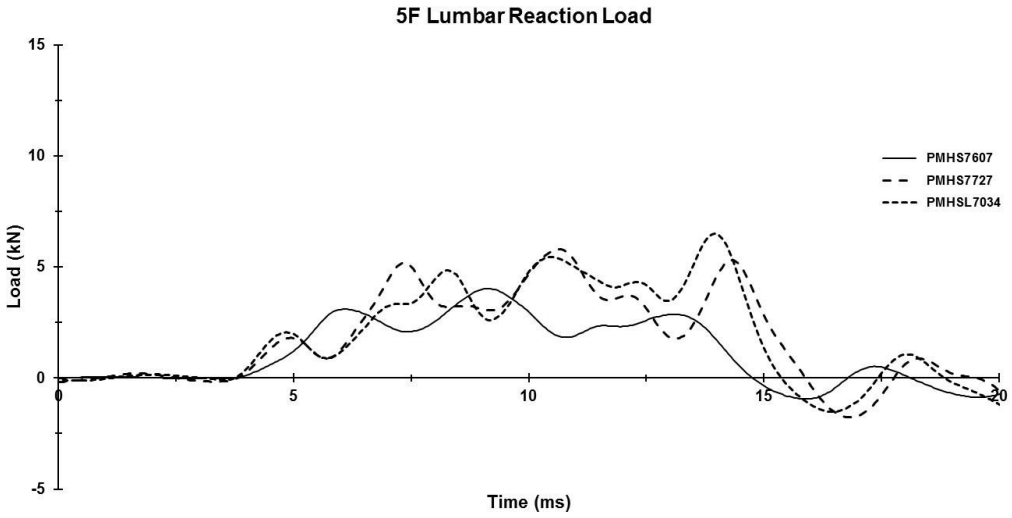

Figure 12. 5th percentile female (5F) reaction loads from cam testing of lumbar spines

Table 4. Summary of L2-L4 fracture loads from lumbar spine testing using the cam device

50M			75F			5F		
PMHS #	**Fx Load (N)**	**Peak (N)**	**PMHS #**	**Fx Load (N)**	**Peak (N)**	**PMHS #**	**Fx Load (N)**	**Peak (N)**
7409	11,084		7469	5,110		7607	4,026	
7575	5,133		7380	6,096		7727	5,190	
7542	4,215	4,390	7058	4,273	5,626	L7034	3,330	
7406	8,772		7834	6,083				
7849	7,713		2366	8,208				
7654	6,891	9,026						
7282	9,835							
Average	**7,663**	**7,993**	**Average**	5,954	**6,225**	**Average**	**4,182**	
Std. Dev.	**±2,468**	**±2,445**	**Std. Dev.**	±1,471	**±1,180**	**Std. Dev.**	**±940**	

Note: The gray values are the fracture loads obtained after a conformation shift (slip) of the lumbar spine. These numbers are inaccurate. The peak numbers shown are used in their place as at least these loads were tolerated before fracture. These values, used in the statistical analyses that follow, are censored but are more accurate than the fracture loads for an incorrect conformation. Filled cells indicate that there is no data in those locations.

Table 5 shows the statistical analyses associated with these tests. Looking at the values derived from comparisons assuming both equal and unequal standard deviations (Table 4 shows them to be very different), significance is shown for ANOVA, and for individual comparisons between 5F and 50M, and 5F and 75F. While the 50M not found to be statistically different from the 75F for the individual comparisons, the important overall trend is that the 50M lumbar spine fractures at higher load than the 75F lumbar spine, which fractures at higher load than the 5F lumbar spine. This trend is seen readily in Figure 13, which summaries the means. This descriptive statistic trend is the same as for the calcaneus.

Table 5. Statistical analyses of the lumbar spine fracture loads

Statistical Test		p		Notes
ANOVA	One-Way	0.0365	*	Assumes same std. dev.
	Brown-Forsythe	0.0135	*	Assumes different std. dev.
	Welch's	0.0217	*	
Unpaired Student's t-test	5F vs. 50M	0.0344	*	
	75F vs. 50M	0.1686	ns	Not significant
	5F vs. 75F	0.0447	*	
Welch's t-test	5F vs. 50M	0.0074	**	
	75F vs. 50M	0.1350	ns	Assumes different std. dev.
	5F vs. 75F	0.0409	**	

Note: * = significantly different; ** = very significantly different.

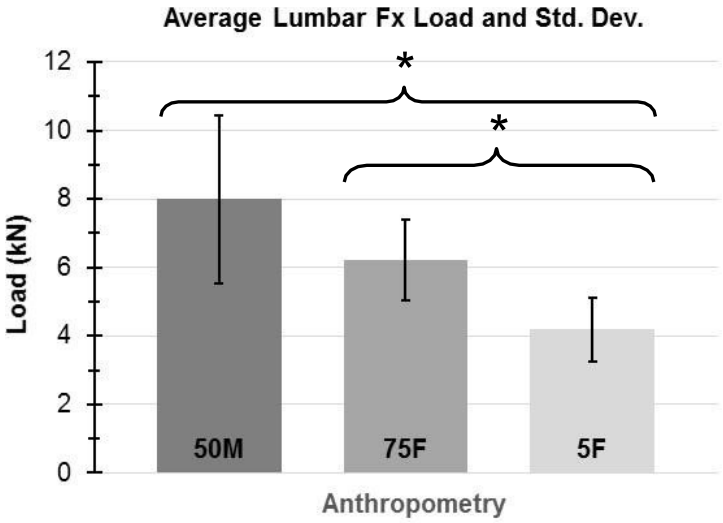

Figure 13. Comparison of averages and standard deviations for the lumbar spine tests

Lumbar spine damage results are cataloged in Appendix C.

5. TIBIA DROP-TOWER TESTING

The TRR tests were conducted with the tibia potting blocks rigidly fixed to the load platforms. This resulted in the appropriate fracture response in one of two tests. Subsequently, a hinge mechanism was added to the bottom of the potting blocks, allowing the blocks to swing toward the center of the bone (probe impact location). This did not produce the required fracture response/pattern. Therefore, the approach was modified again to allow the potting blocks to rotate at the top. This resulted in the required fracture response/pattern and did not damage the bone at the potting locations. Earlier tests that did not work resulted in complex fractures starting away from the probe impact site. This always resulted in very low peak impact loads, which do not reflect the bone tolerance.

Figure 14 shows the revised fixture pieces. Square frames suspend the potting blocks via “overhead” pivots. With this configuration, the tibias fracture mid shaft and are not damaged at the potting locations. The blocks swing away from the incoming probe after fracture. This method always produced usable results.

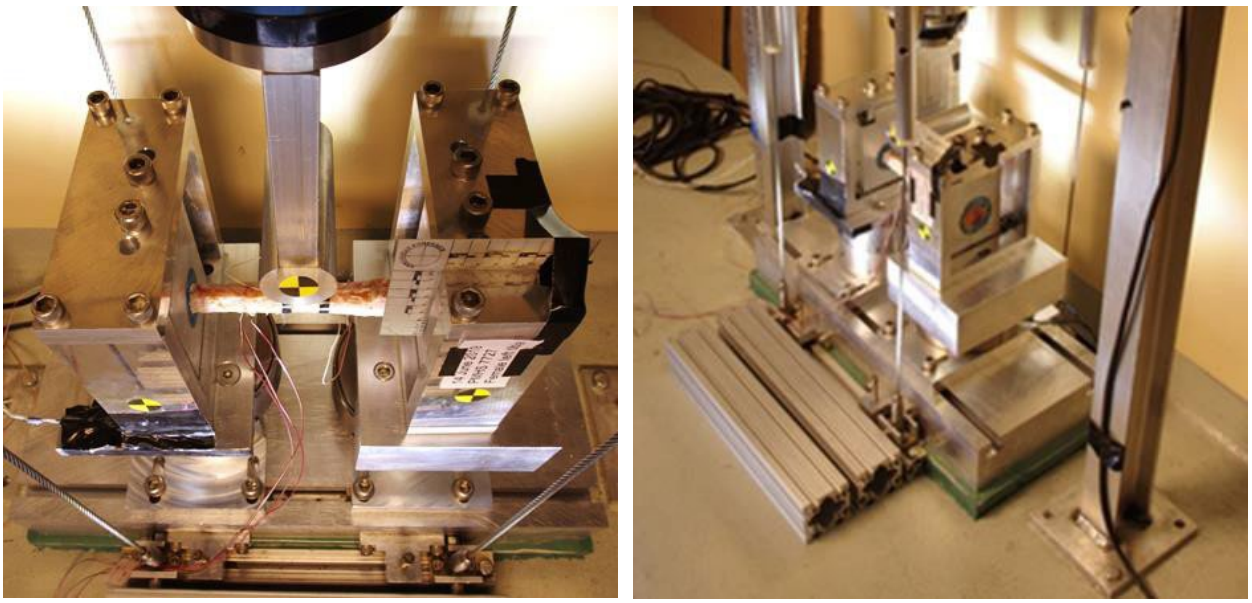

Figure 14. Fixtures and testing apparatus for the tibia drop tests, showing the revised frames that suspend the mounting blocks using an overhead-pivot/hinge approach. The bottom of the blocks swings away from center after the tibia fractures.

Figure 15 shows a pretest configuration using the revised drop-tower fixtures. The probe of the 24-kg pendulum was set to impact the lateral aspect of the bone at the middle of the shaft. The impact speed was set to 5 m/s. A medium-sized (50-mm diameter) indenter was used. High-resolution, high-speed video was used to document each impact. Strain gages fixed to the bones corroborated fracture timing. Using the

revised fixtures, all bones fractured mid-shaft similarly, without compromising the bone at the potting margins, as represented in Figure 16. Figure 17 shows a representative posttest tibia configuration. The potting blocks swung away from the probe, resulting in repeatable fracture results. The details of the suspension frame and top-pivot apparatus are shown on the right of Figure 17. Each frame was supported by a six-axis load cell. However, the impact generated severe resonance in the cells, particularly in the direction of impact. Fracture load was determined using inertia compensation of the pendulum load. This was compared to pendulum mass multiplied by the average of the two pendulum acceleration measurements. The comparisons were excellent. Seatbelt webbing was used to arrest the pendulum after it passed completely through the bone, which did not influence impact load measurement. This part of the event was used to confirm compensation.

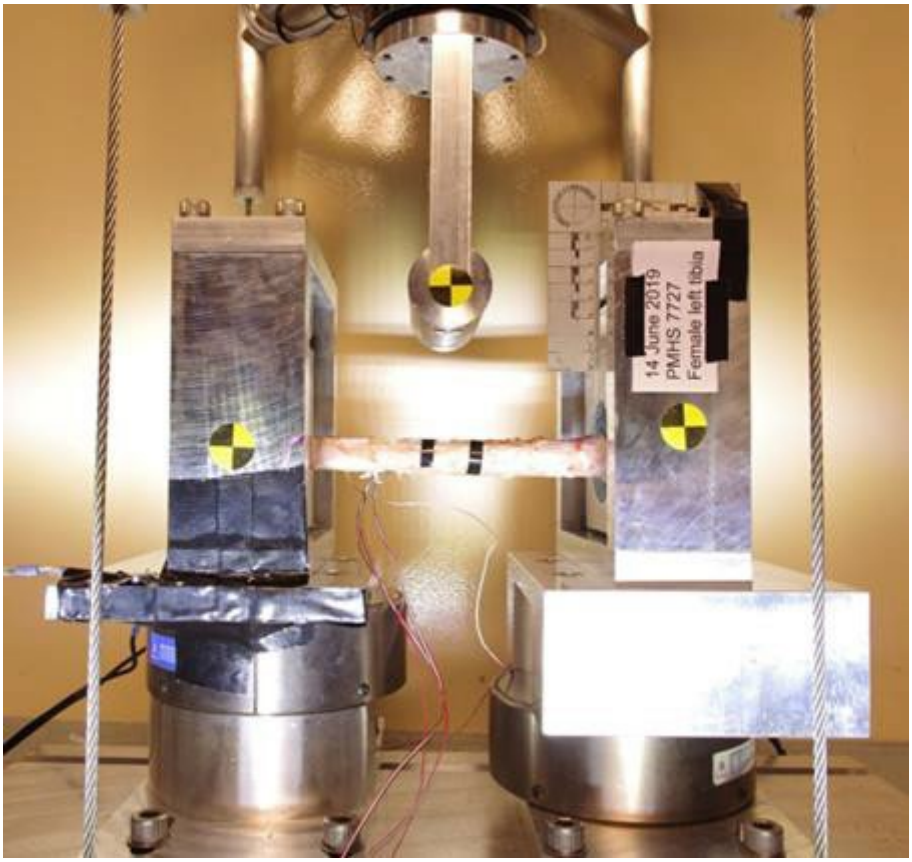

Figure 15. A representative left tibia specimen from PMHS7727 installed in the drop tower for three-point impact testing

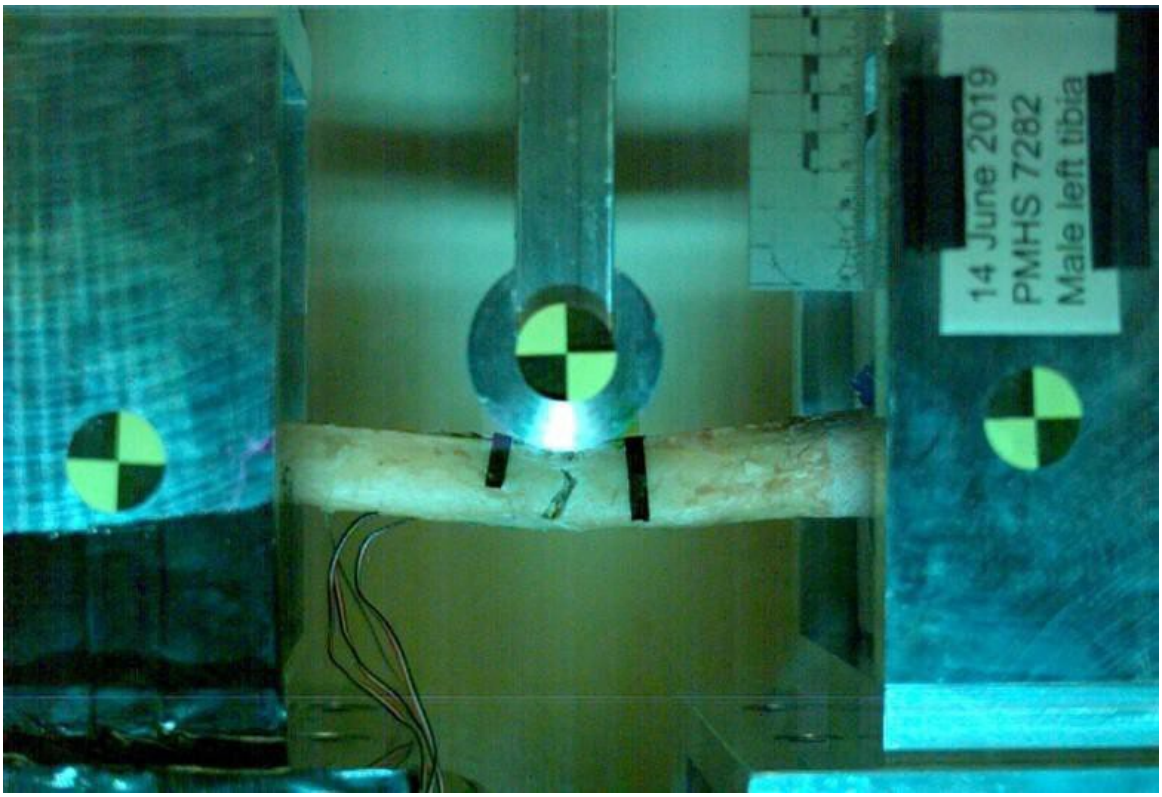

Figure 16. High-speed video frame showing a representative mid-shaft left tibia fracture. The crack forms directly beneath the probe. The potting blocks pivot after the fracture.

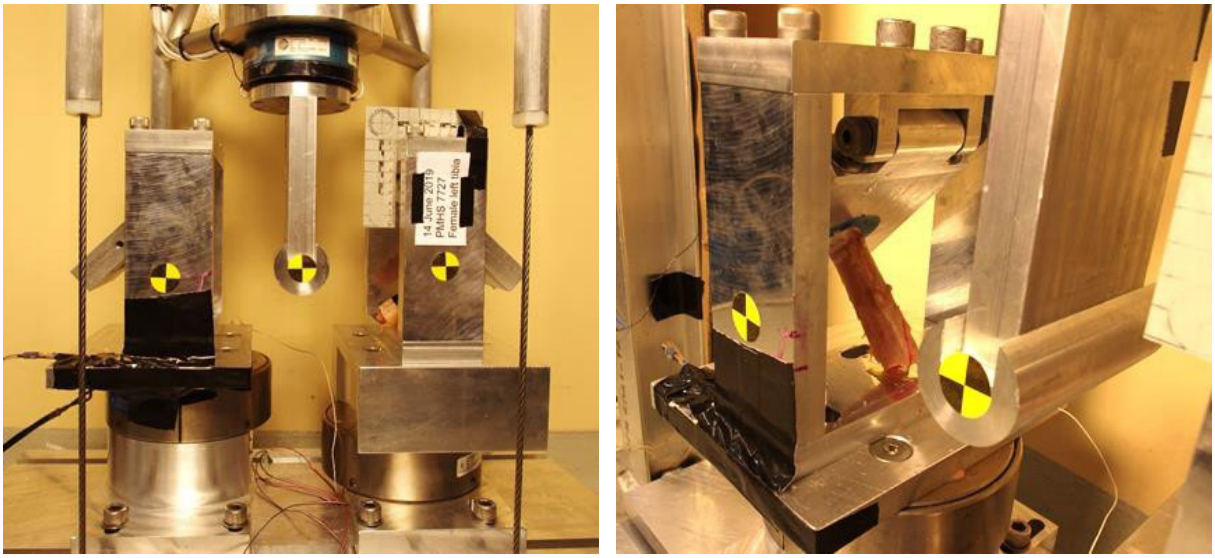

Figure 17. Posttest images showing the resting conformation of the tibia bone halves and probe for PMHS7727. The potting blocks are shown to have swung away from the center/probe. The details of the suspension frame and pivot mechanism are shown on the right.

Figure 18 shows the impact loads for the 50M tibia tests. All of the magnitudes, shapes, and durations are consistent, except for two tests. One of these tests was from the TRR (fixed potting blocks), and one was from early testing using the bottom pivot approach. Both tests resulted in complex fractures originating away from the probe impact point. The load traces are characterized by low magnitude and unusual shape. These are not considered valid tests. For all tests, after the initial fracture load (beginning ~1 ms later), there is a second smaller but longer loading phase resulting from continued interaction between the probe and the bones as the fracture propagates through the bone.

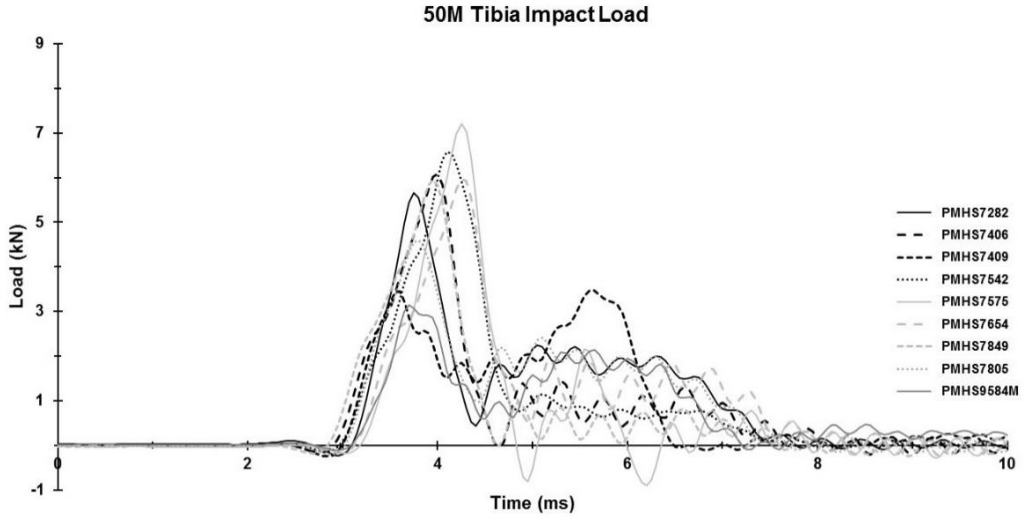

Figure 18. 50th percentile male (50M) reaction loads from drop/impact testing of left tibias

Figure 19 shows the impact loads for the 75F tibia tests. All the magnitudes, shapes, and durations are consistent, except for one test, which was from early testing using the bottom pivot approach. Again, this test resulted in complex fractures originating away from the probe impact point and is not considered valid. While the shapes and durations of these loads are similar to those from the 50M, the magnitudes are considerably less. The consistency of the 50M and 75F results is remarkable within both groups.

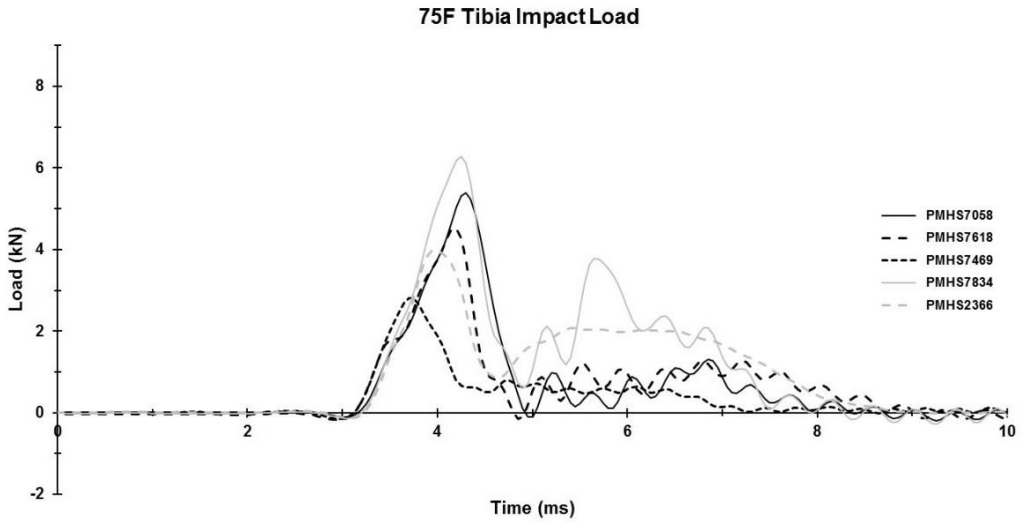

Figure 19. 75th percentile female (75F) reaction loads from drop/impact testing of left tibias

Figure 20 shows the impact loads for the 5F tibia tests. There is greater variation within these results than for the 50M and 75F tests. However, the magnitudes, shapes, and durations are still similar. The peak (fracture) loads are less than those for both the 50M and 75F tests.

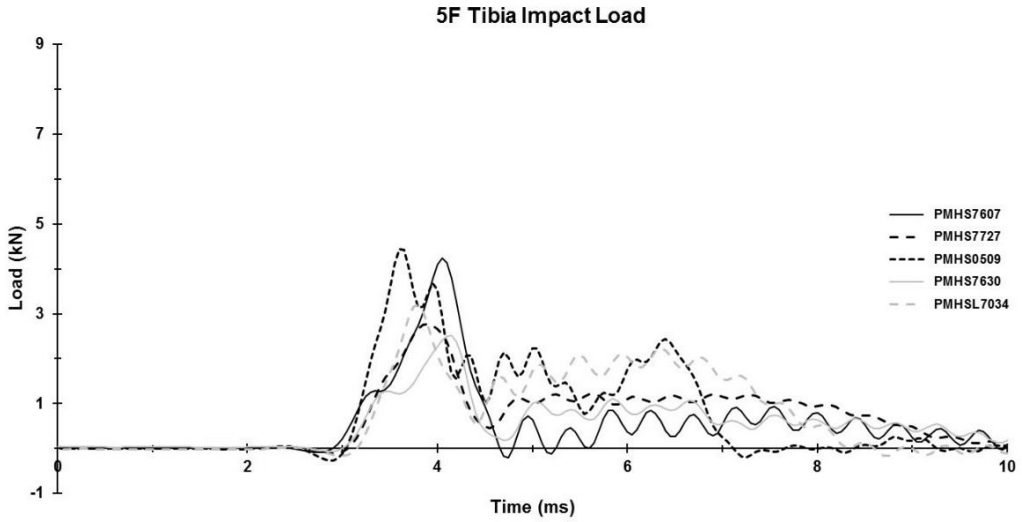

Figure 20. 5th percentile female (5F) reaction loads from drop/impact testing of left tibias

Table 6 summarizes the tibia fracture loads for the three anthropometries. The 50M specimens had the highest average fracture loads and standard deviations, while the 5F specimens had the lowest. The different fracture thresholds and fracture patterns suggest that the tibias of females respond differently to lateral impact than do those of males. With the exclusion of the invalid tests, the standard deviations of the tests within the three groups is nearly identical (800–1,005 N), demonstrating repeatability of these tests. This is important to the statistical testing when only limited specimens are available.

Table 6. Summary of fracture loads from impact of the lateral aspect of left tibias

50M		75F		5F	
PMHS #	**Fx Load (N)**	**PMHS #**	**Fx Load (N)**	**PMHS #**	**Fx Load (N)**
7409	3,473	7469	2,817	7607	4,242
7575	7,293	7618	4,522	7630	2,512
7542	6,585	7058	5,382	0509	4,451
7805	4,599	7834	6,278	7727	2,769
7406	6,086	2366	3,984	L7034	3,201
7849	5,947				
9584M	3,136				
7654	5,967				
7282	5,660				
Average	**6,020**	**Average**	**5,042**	**Average**	**3,435**
Std. Dev.	**±827**	**Std. Dev.**	**±1,005**	**Std. Dev.**	**±871**

Note: The gray values are the fracture loads obtained after a conformation shift (slip) of the tibia. These numbers are inaccurate. Filled cells indicate that there is no data in those locations.

Table 7 shows the statistical analyses associated with these tests. Values shown in gray in Table 6 are excluded (invalid). Significance is shown for ANOVA and for individual comparisons between 5F and 50M and 5F and 75F, similar to the lumbar spine results. While the 50M was not found to be statistically different from the 75F for the individual comparisons, the important overall trend is that the 50M lumbar spine fractures at higher load than the 75F lumbar spine, which fractures at higher load than the 5F lumbar spine. This trend is seen readily in Figure 21, which summaries the means. This is the same trend as shown by the descriptive statistics for the calcaneus and the lumbar spine.

Table 7. Statistical analyses of the tibia impact fracture loads

Statistical Test		p		Notes
ANOVA	One-Way	0.0009	***	Assumes same std. dev.
	Brown-Forsythe	0.0026	**	Assumes different std. dev.
	Welch's	0.0051	**	
Unpaired Student's t-test	5F vs. 50M	0.0004	***	
	75F vs. 50M	0.1136	ns	Not significant
	5F vs. 75F	0.0369	*	

Note: */**/*** = statistically significant to different degrees.

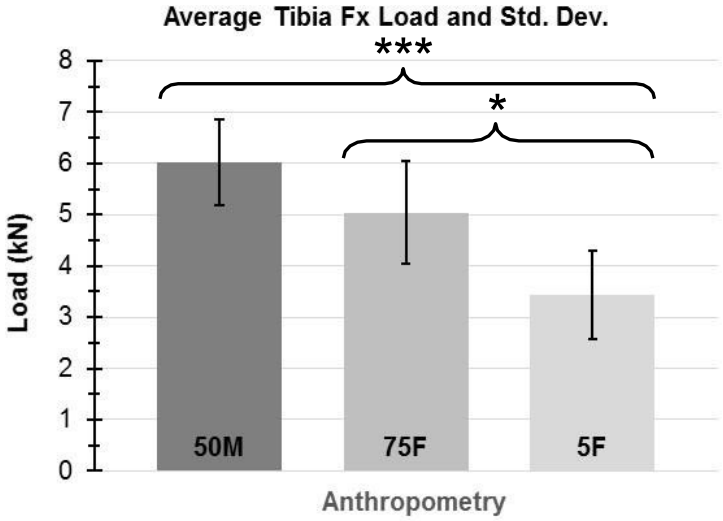

Figure 21. Comparison of averages and standard deviations for the tibia impact/drop-tower tests

Initiation of left tibia mid-diaphysis fractures are cataloged in Appendix D.

6. SACRUM/PELVIS CAM TESTING USING HIGH-SPEED X-RAY

Initially, it was planned to load the ischium of hemi-pelvises using the cam follower, with the ilium potted and mounted to the reaction load cell structure. However, concerns over large loads, and producing an essentially bending mechanism of fracture, resulted in rethinking the approach. Further, there was interest in generating more theater-relevant damage, such as disruption of the sacral alae, proximal to the sacrum (medial fractures). Therefore, a new concept was implemented. The new approach involves loading L5 with the cam follower, with each ilium potted. This required new fixtures that allowed the pelvis to be potted symmetrically, as only one side could be potted at a time. Figure 22 shows a completed preparation. A threaded rod is used to maintain distance between the ilia. The trabecular bone of L5 is evacuated and filled with potting compound. L5, the potting, and the posterior elements are cut to be flush. The lateral processes are removed from L5 to avoid interaction with the alae.

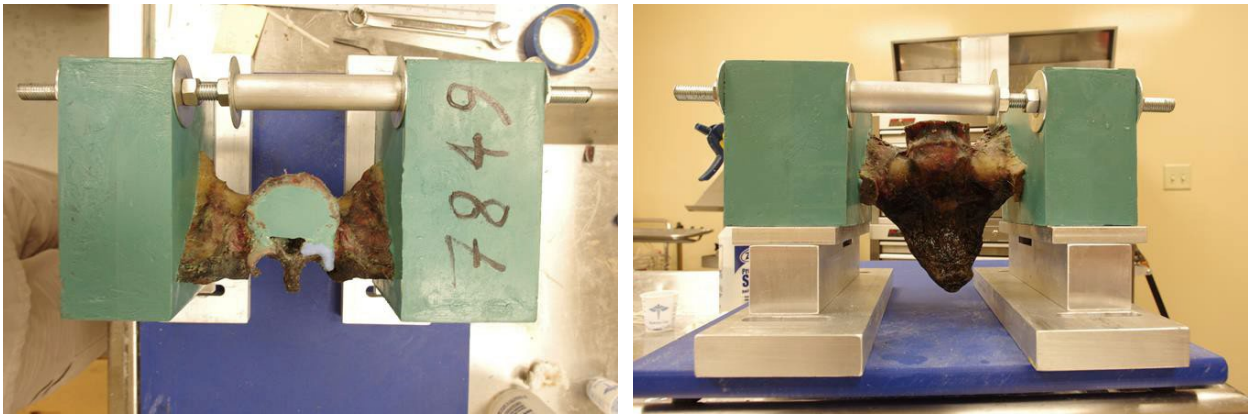

Figure 22. A finished pelvis preparation showing the potting in L5 being flush with the pedicles/laminae

Figure 23 shows a representative pelvis preparation installed in the cam apparatus. The cam follower is located to the left of each image and the reaction block is to the right. The cam follower interfaces with the potting in L5 and the posterior elements of L5. Loading the entire column (body and posterior elements) is important to producing the correct repeatable damage pattern. Similarly, not allowing the ilia to splay during the test is important, necessitating a truss/spacer be placed between the ilia, through the potting compound. Figure 24 shows a representative resulting damage pattern. The sacral alae are shear from the bodies of the sacrum, near their junction with the sacral bodies. This occurs bilaterally or unilaterally. The costal elements arising from S1-S3 comprise the sacral alae. Additional costal elements branching from S4 and S5 give rise to the sacral foramena. Fractures typically begin near the more caudal costal elements

and propagate to the alae. The characteristics of sacral fracture and the propagation sequences are cataloged in Appendix E.

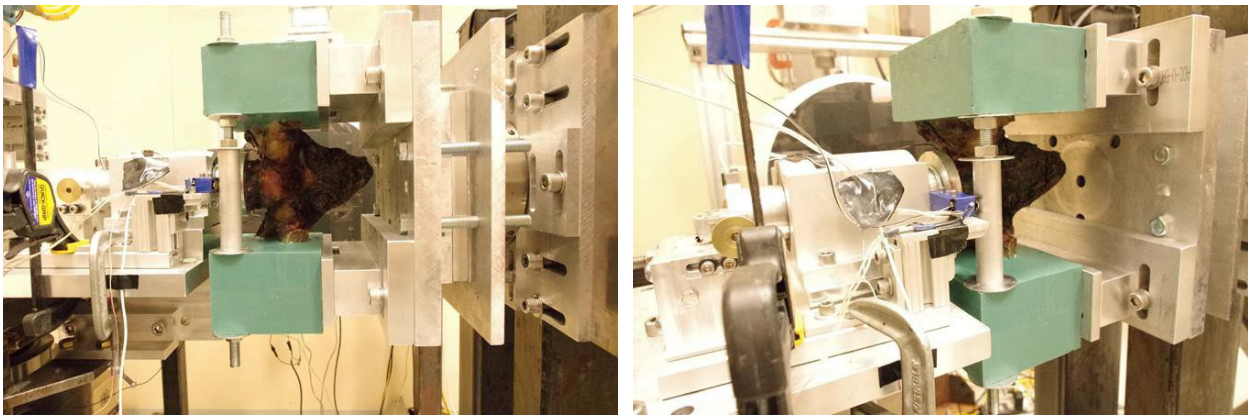

Figure 23. A representative pelvis preparation installed in the cam device in front of the X-ray system

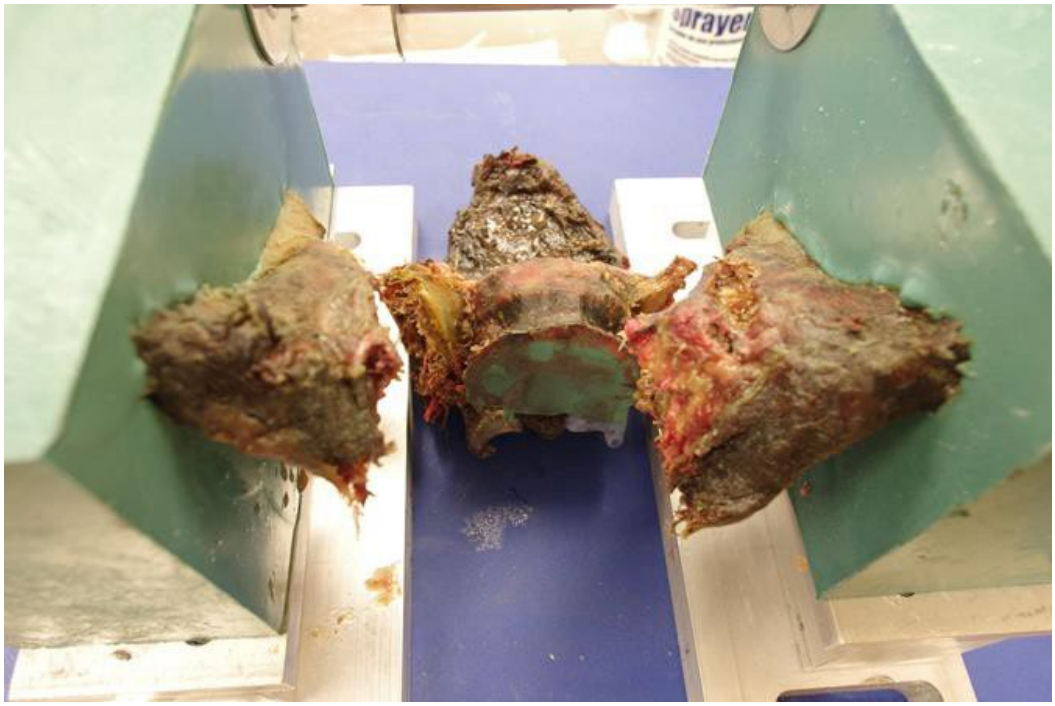

Figure 24. Representative bilateral sacral alae damage resulting from a pelvis test

Figure 25 shows the high-speed X-ray from two tests. The X-ray is directed anteroposteriorly. Bilateral damage is shown on the left (PMHS7607, 5F), and unilateral damage is shown on the right (PMHS7575, 50M). A quasi-static test (PMHS7282) was conducted prior to the dynamic tests to confirm the desired damage pattern results would be achieved and that the reaction loads would not exceed the limits of the cam follower (40 kN). A peak load of 5,160 N was observed. This sacrum/pelvis was initially

tested in a preparation involving an intact pelvis and potting of the ischial tuberosities (10,229-N peak load). Figure 26 shows the reaction loads for the 50M sacrum/pelvis tests. All of the magnitudes, shapes, and durations are consistent, except for PMHS7654, which demonstrated a pronounced second peak. Figure 27 shows the reaction loads for the 75F sacrum tests. Again, the shapes and durations are consistent, with one test (PMHS7380) having substantially smaller magnitude than the other two tests. Figure 28 shows the reaction loads for the 5F tibia tests. There is greater magnitude variation within these results than for the 50M tests. However, the shapes and durations are very similar. The fracture load magnitudes are not appreciably different than those from the tests.

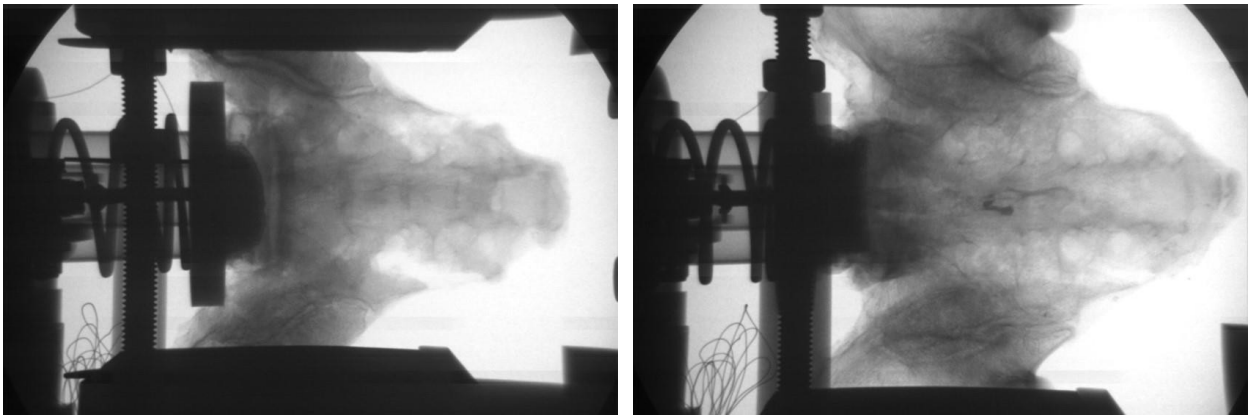

Figure 25. Initiation of bilateral sacral alae damage (left, PMHS7607, 5F) and unilateral sacral alae damage (right, PMHS7575, 50M), as imaged using high-speed X-ray during testing in the cam device

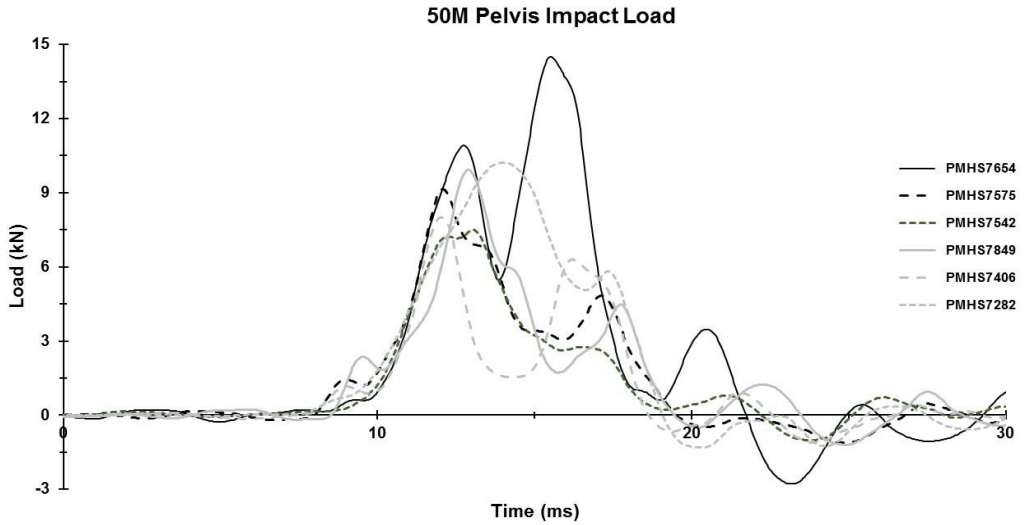

Figure 26. 50th percentile male (50M) pelvis reaction loads from cam testing of the sacrum

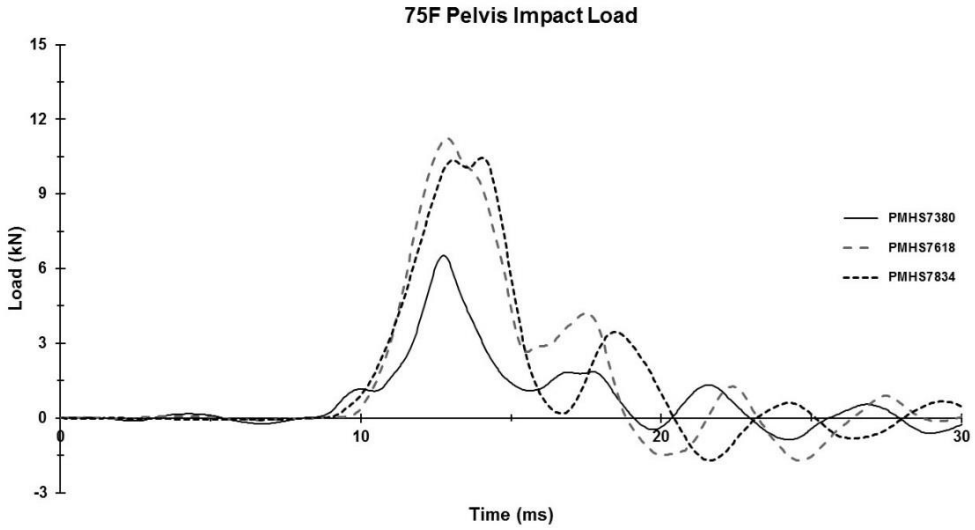

Figure 27. 75th percentile female (75F) pelvis reaction loads from cam testing of the sacrum

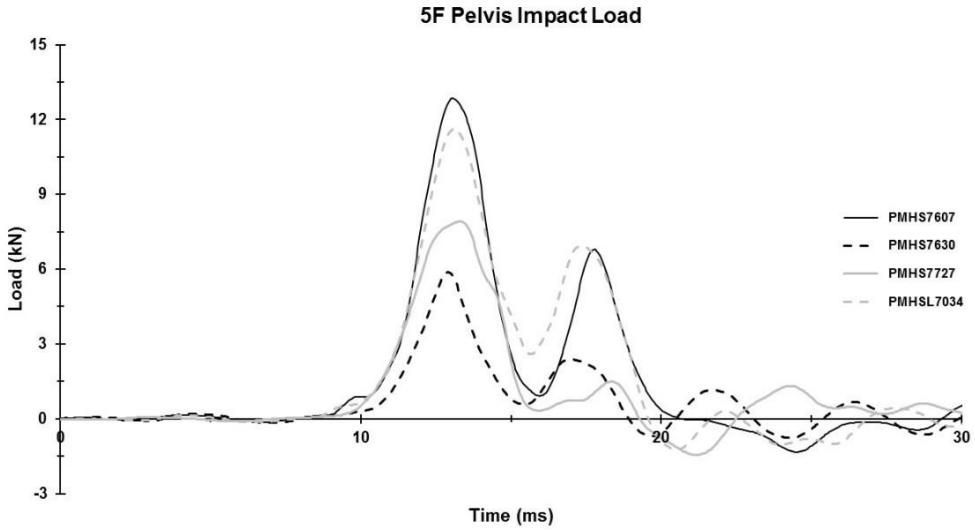

Figure 28. 5th percentile female (5F) pelvis reaction loads from cam testing of the sacrum

Table 8 summarizes the sacrum fracture loads for the three anthropometries. The 50M specimens had the highest average fracture load, while the 75F specimens had the lowest. The average fracture load for the 5F group was nearly identical to the 75F group. The standard deviations are of the same order across all three groups.

Table 8. Summary of sacrum fracture (pelvis reaction) loads from loading of L5 using the cam device

50M		75F		5F	
PMHS #	**Fx Load (N)**	**PMHS #**	**Fx Load (N)**	**PMHS #**	**Fx Load (N)**
7654	14,494	7380	6,526	7607	12,857
7575	9,139	7618	11,230	7630	5,885
7542	7,226	7834	10,353	7727	7,922
7849	9,924			L7034	11,636
7406	7,995				
7282	10,229				
Average	**10,196**	**Average**	**9,370**	**Average**	**9,575**
Std. Dev.	**±3,081**	**Std. Dev.**	**±2,501**	**Std. Dev.**	**±3,234**
Including gray values and underlined values halved (alternate analyses)					
Average	**9,835**	**Average**	**6,557**	**Average**	**6,513**
Std. Dev.	**±2,551**	**Std. Dev.**	**±4,159**	**Std. Dev.**	**±978**

Note: Gray values are loads reached without sacrum fracture. Underlined values are associated with simultaneous bilateral fracture.

The values shown in gray in Table 8 are loads reached without sacrum fracture. These data are censored, but it is known that at least these loads could be supported in the absence of fracture. The values underlined in Table 8 are those associated with simultaneous bilateral fracture. The descriptive statistics and analyses for significance were performed using two different approaches. First, the averages and tests for significance were evaluated when excluding the values in gray (Table 9 and Figure 29). Little difference was disclosed between the groups. They are statistically similar. Second, the averages and tests for significance were evaluated while including the values in gray and using one-half of each value underlined (Table 10 and Figure 30). The rationale for using half of the load for the simultaneous bilateral fracture cases is that each side of the sacrum/pelvis complex was supporting one-half of the load at the time of fracture initiation. Using this alternate approach, statistical significance is demonstrated between the 50M and 5F groups, with the males having substantially higher fracture loads. The similarity between the 75F and 5F groups confounds establishing significance via ANOVA. While there are few specimens within each group, it seems reasonable that the bone within the costal elements might be organized such that strength is similar for all females. For example, while larger females might have more bone, it is distributed within a larger volume, and while smaller females might have less bone, it is distributed within a smaller volume. These two different amounts and distributions of bone could result in common fracture thresholds. This bears further investigation.

Table 9. Statistical analyses of the pelvis reaction loads for sacrum fracture

Statistical Test		p		Notes
ANOVA	One-Way	0.9287	ns	Assumes same std. dev.
	Brown-Forsythe	0.9254	ns	Assumes different std. dev.
	Welch's	0.9317	ns	
Unpaired Student's t-test	5F vs. 50M	0.7904	ns	Not significant
	75F vs. 50M	0.7211	ns	
	5F vs. 75F	0.9312	ns	

Note: "ns" is not significant.

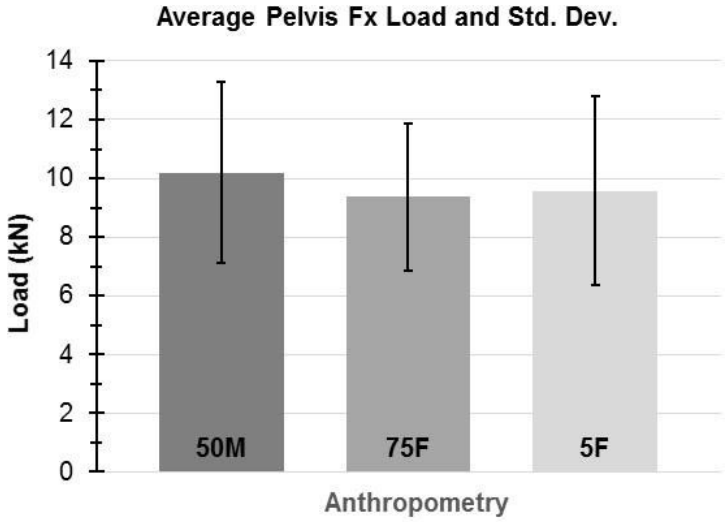

Figure 29. Comparison of averages and standard deviations for the sacrum/pelvis cam tests

Table 10. Alternate statistical analyses of the pelvis reaction loads for sacrum fracture

Statistical Test		p		Notes
ANOVA	One-Way	0.1302	ns	Assumes same std. dev.
	Brown-Forsythe	0.2661	ns	Assumes different std. dev.
	Welch's	0.1190	ns	
Unpaired Student's t-test	5F vs. 50M	0.0402	*	
	75F vs. 50M	0.1781	ns	Not significant
	5F vs. 75F	0.9843	ns	Not significant

Note: * is statistically significant / "ns" is not significant.

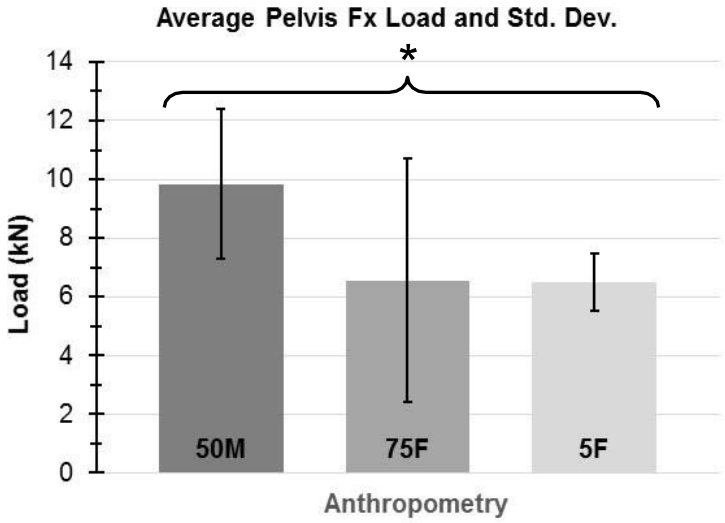

Figure 30. Alternate comparison of averages and standard deviations for the sacrum/pelvis cam tests

7. CATALOG OF TESTING SPEEDS

Table 11 catalogs the peak speeds associated with all testing for which the data have been processed/analyzed. These results show the extent of repeatability for each loading mode. Variation in peak speed for the cam tests is related to how the specimens fracture and subsequent variation in the cam follower motion. During fracture, the follower can lose intimate contact with the cam for a fraction of a millisecond, resulting in lower apparent peak follower speed. Conversely, when a structure fractures early in the stroke cycle, resistance to the follower's motion decreases, and the cam can "throw" the follower, resulting in higher speeds. This occurs during some of the sacrum/pelvis tests.

Table 11. Summary of test peak speeds

%ile & Sex	PMHS #	Left Tibia (m/s)	Lumbar (m/s)	Right Ankle (m/s)	Pelvis (m/s)
50M	7409	4.8	5.0	4.6	…
	7575	5.1	5.1	5.1	4.8
	7542	5.1	4.6	4.5	5.2
	7805	5.0	-	4.5	…
	7406	5.2	4.9	4.2	4.4
	7849	5.3	4.5	5.0	4.6
	9584M	4.6	…	…	…
	7654	4.9	5.1	…	5.4
	7282	4.9	4.6	…	4.8
75F	7469	5.1	4.6	4.7	…
	7380	…	5.4	4.7	4.9
	7618	5.2	…	4.8	5.3
	7058	5.1	4.7	4.9	…
	7834	5.0	4.2	5.2	5.5
	2366	5.1	4.8	4.9	…
5F	7607	5.2	5.1	4.5	4.6
	7630	5.4	…	4.5	4.8
	0509	5.3	…	4.4	…
	7727	5.0	4.9	4.8	5.6
	L7034	5.2	4.9	4.7	4.7
	Average	**5.1**	**4.8**	**4.7**	**5.0**
	Std. Dev.	**0.2**	**0.3**	**0.3**	**0.4**

8. RIB TESTING

The complete collection of rib data has been reduced from 33 tests. The rib specimens and mechanical properties are summarized in Table 12. These results, in combination with the tibia impact results, support the sex/bone condition mapping effort.

Table 12. Catalog of rib mechanical properties

PMHS/Test Info			Demographics			Structural Properties		
PMHS ID	Project	Test ID	Sex	Age (yrs)	Stature (cm)	Peak Force in X (*FPEAK*) (N)	Linear Structural Stiffness (*K*) (N/mm)	Total Energy to Fracture (*Utot*) (N*mm)
7082	WB ALF	Hrb247	M	58	185.4	87.09	2.31	3282.41
7099	WB ALF	Hrb249	M	54	182.9	95.51	3.62	1667.95
7081	WB ALF	Hrb250	M	73	182.9	101.89	2.83	4230.51
7115	WB ALF	Hrb251	M	69	186.7	87.65	3.06	2261.93
7089	WB ALF	Hrb259	F	54	162.6	64.05	2.07	1362.61
6906	WB ALF	Hrb260	F	45	166.4	99.69	2.77	3250.01
6989	WB ALF	Hrb264	F	57	175.3	52.34	1.42	1794.21
7320	WB ALF	Hrb285	F	57	162.6	73.64	1.97	2551.08
LL16-07017	WB ALF	Hrb289	F	55	165.1	98.68	2.28	5056.28
7219	WB ALF	Hrb292	F	66	165.1	48.79	1.09	1887.67
LL16-11053	WB ALF	Hrb347	F	75	167.6	33.89	1.01	788.31
7385	WB ALF	Hrb348	M	55	172.7	129.32	3.36	2940.67
7253	WB ALF	Hrb349	M	50	180.3	202.76	5.65	5281.97
MC1610787F	WB ALF	Hrb355	F	50	162.5	73.67	1.53	2650.18
7312	WB ALF	Hrb356	F	36	160.0	112.59	3.22	3655.30
7594	WB ALF	Hrb361	M	29	182.9	120.40	2.17	13338.86
7282	Component	Hrb346	M	68	167.6	159.68	4.97	4444.43
7375	Component	Hrb360	M	68	177.8	159.06	4.46	5653.96
7654	Component	Hrb362	M	58	177.8	99.15	2.71	2449.52
7542	Component	Hrb365	M	49	165.1	93.64	2.03	4178.97
7409	Component	Hrb366	M	54	175.3	128.14	3.17	5296.96
7406	Component	Hrb368	M	68	170.2	144.47	5.22	3105.89
7618	Component	Hrb369	F	62	162.6	123.84	4.09	2109.20
7469	Component	Hrb371	F	58	167.6	69.63	2.37	919.67
7630	Component	Hrb372	F	64	165.1	65.83	2.21	1068.80
7607	Component	Hrb374	F	79	162.6	34.28	1.94	552.33
7575	Component	Hrb375	M	69	175.3	161.99	3.46	6148.47
7380	Component	Hrb376	F	67	162.6	110.93	3.96	1674.87
7058	Component	Hrb378	F	41	168.9	50.31	1.04	2498.21
7849	Component	Hrb386	M	74	180.3	119.56	5.32	2328.30
7805	Component	Hrb387	M	68	185.4	104.19	3.44	2069.02
7727	Component	Hrb388	F	61	165.1	54.76	1.35	1524.93
7834	Component	Hrb390	F	64	167.6	89.48	2.62	2162.66

9. CONCLUSION

All test results indicate, with statistical significance, the differences in tolerance and loading response between males and females. The experimental repeatability designed into these tests and testing apparatus produced minimal experimental variance, allowing trends and significance to be established using relatively few specimens. The general trends for all testing are the same: damage thresholds for 50M are greater than for 75F, which are greater than for 5F. In some cases, the damage patterns differ between the three groups. While the source of these differences has not yet been specifically identified, it appears there is a fundamental difference in the female response to load. It is hypothesized this could be due to variations in anatomy, bone distribution, and tissue material properties.

These results show that uniform functions for injury risk prediction and common injury assessment reference values cannot be applied across the sexes, nor within the two female anthropometry categories examined in this study. Further experimental work would be necessary to create female specific injury data.

Appendix A – Examples of Events Excluded from Statistical Analyses

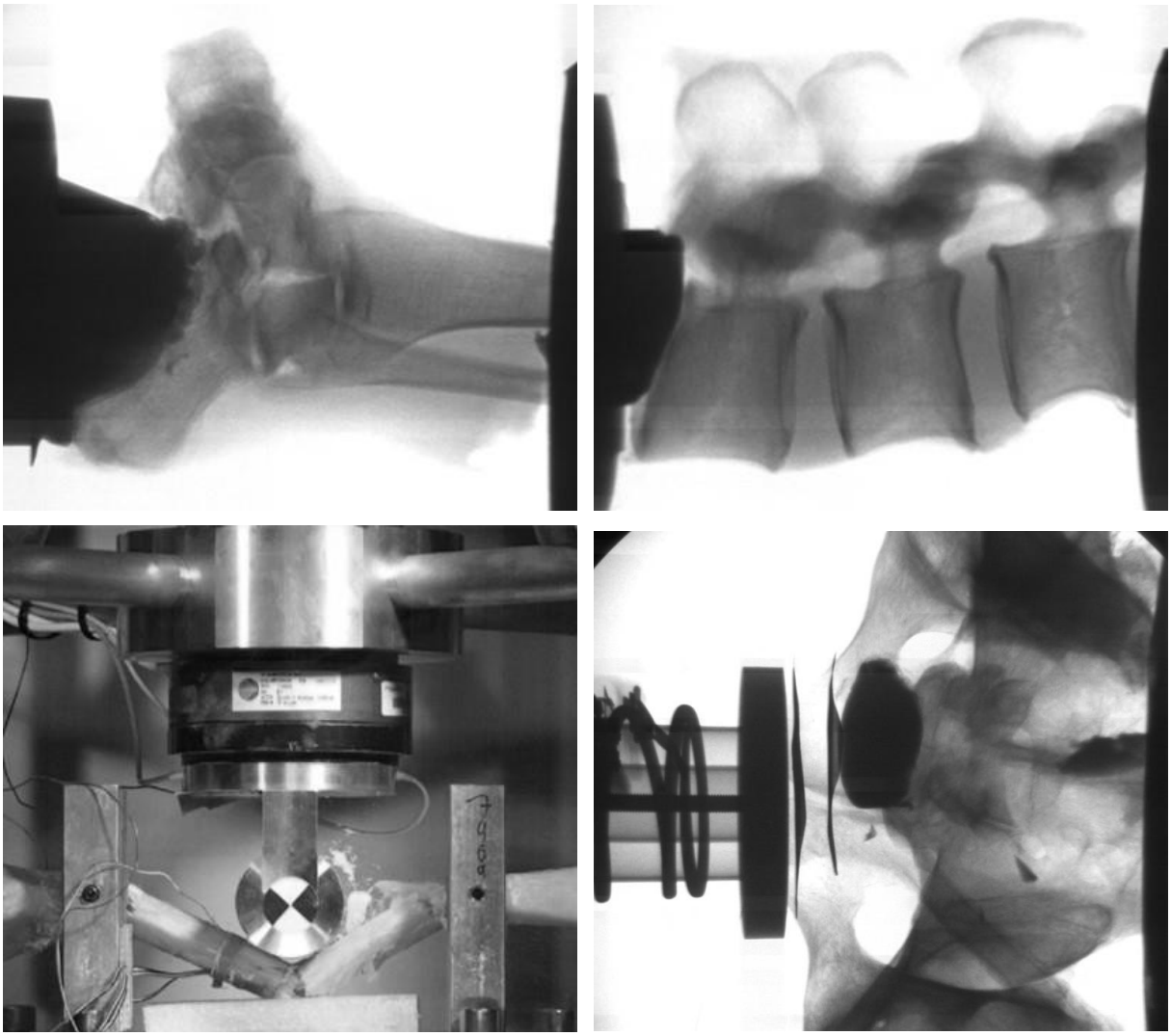

Figure A-1. An ankle test of PMHS2366 involving talus fracture concurrent with calcaneus fracture (top left); a lumbar spine test of PMHS7654 showing slipping of L4 from the potting compound, creating a local load maxima (top right); a left tibia drop test of PMHS7469 showing multi-segment damage resulting from fixed end supports (lower left); and a sacrum test of PMHS7282 showing disruption of the preparation and fracture of the left ischium and inferior ramus (lower right)

Appendix B – Catalog of Right Calcaneus Fracture Characteristics

Table B-1. Concomitant fractures associated with ankle/foot testing

Specimen PMHS #	Concomitant Damage
2366	Talus
7469	Pilon
7630	Talus

Figure B-1. Fracture of the right calcaneus plantar view (left) and sagittal view (right) of PMHS7409

Figure B-2. Fracture of the right calcaneus plantar view (left) and sagittal view (right) of PMHS7575

Figure B-3. Fracture of the right calcaneus plantar view (left) and sagittal view (right) of PMHS7542

Figure B-4. Fracture of the right calcaneus plantar view (left) and sagittal view (right) of PMHS7805

Figure B-5. Fracture of the right calcaneus plantar view (left) and sagittal view (right) of PMHS7406

Figure B-6. Fracture of the right calcaneus plantar view (left) and sagittal view (right) of PMHS7849

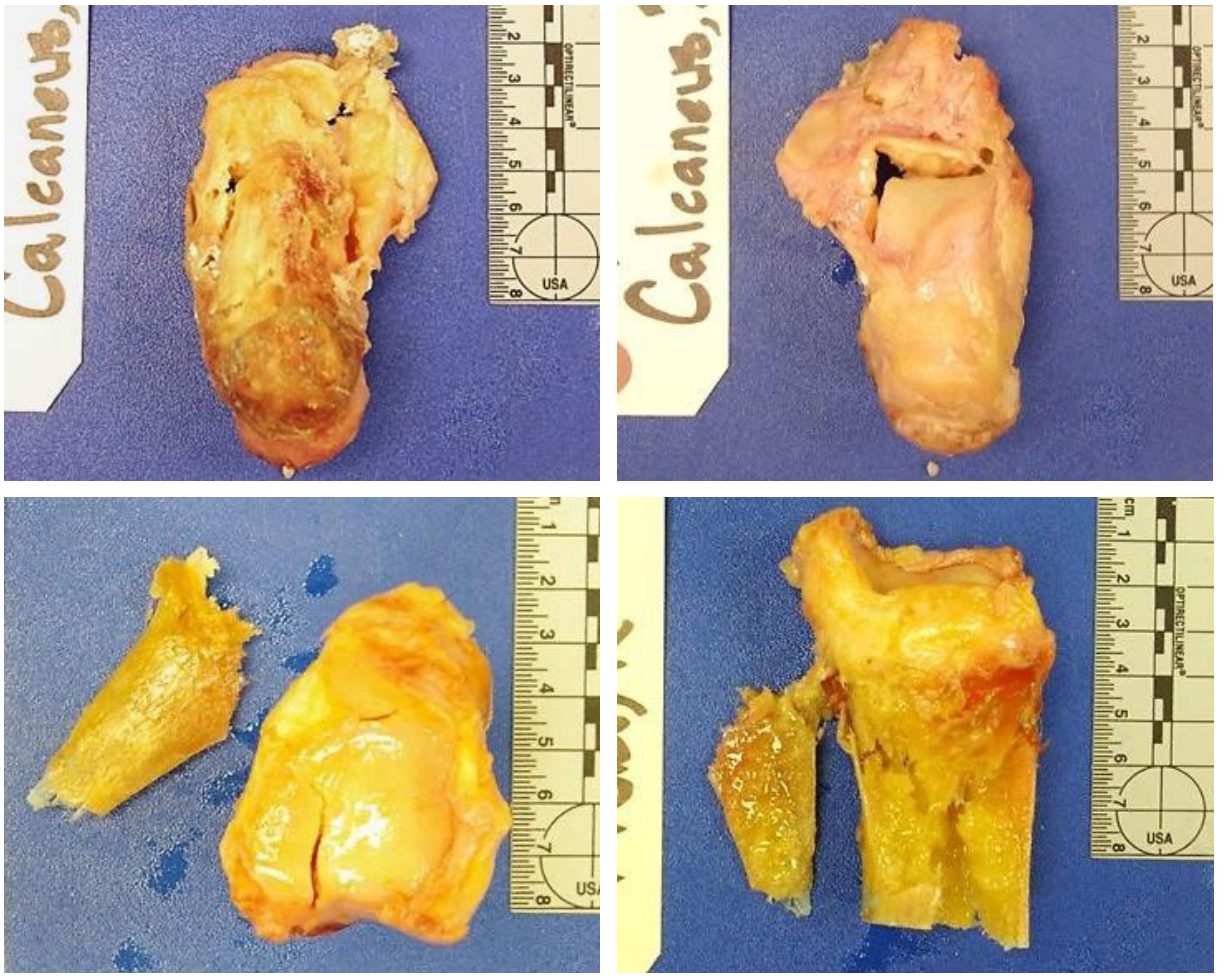

Figure B-7. Fracture of the right calcaneus plantar view (top left) and sagittal view (top right) of PMHS7469. Pilon fracture of PMHS7469 axial view (bottom left) and anterior view (bottom right).

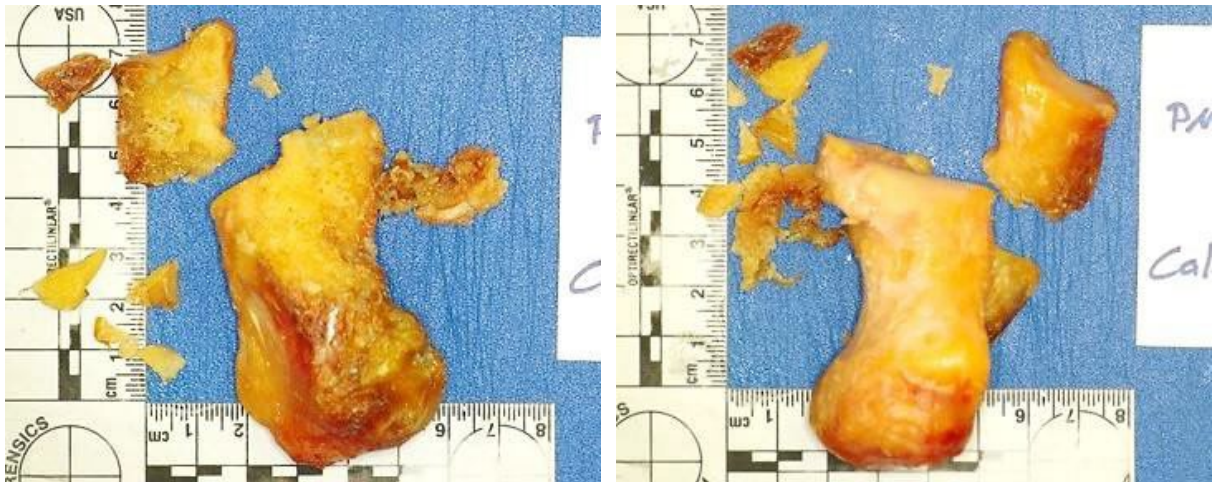

Figure B-8. Fracture of the right calcaneus plantar view (left) and sagittal view (right) of PMHS7380

Figure B-9. Fracture of the right calcaneus plantar view (left) and sagittal view (right) of PMHS7618

Figure B-10. Fracture of the right calcaneus oblique view of PMHS7058

Figure B-11. Fracture of the right calcaneus plantar view of PMHS7834

Figure B-12. Fracture of the right calcaneus plantar view (top) of PMHS2366 and the right talus of PMHS2366 (bottom left and right)

Figure B-13. Fracture of the right calcaneus plantar view (left) and sagittal view (right) of PMHS7607

Figure B-14. Fracture of the right calcaneus plantar view (left) of PMHS7630 and the right talus of PMHS7630 (right)

Figure B-15. Fracture of the right calcaneus oblique view (left) of PMHS0509 (TRR5)

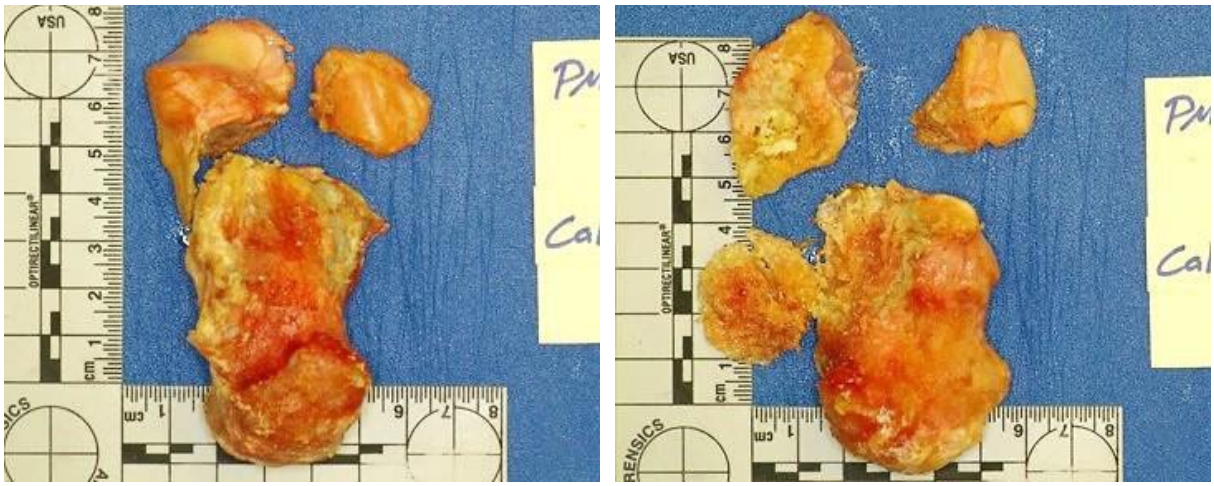

Figure B-16. Fracture of the right calcaneus plantar view (left) and sagittal view (right) of PMHS7727

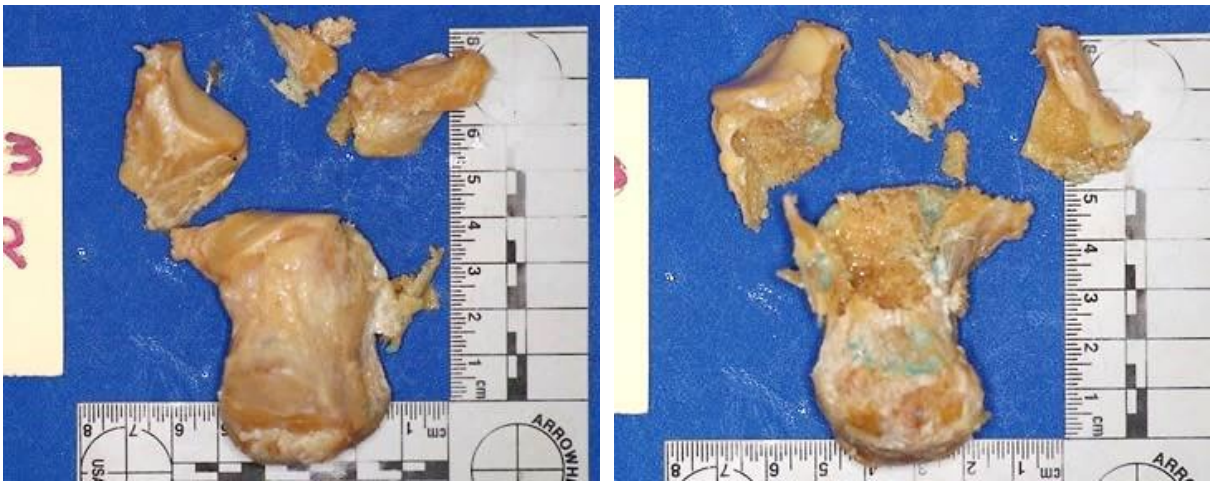

Figure B-17. Fracture of the right calcaneus plantar view (left) and sagittal view (right) of PMHSL7034

Appendix C – Catalog of Lumbar Spine (L2-L4) Fracture Characteristics

Table C-1. Details of lumbar spine damage

Specimen		Damage
PMHS #	Level	
7409	L2	NA
	L3	NA
	L4	Burst, inferior end plate, partial superior midline split near process
7575	L2	Superior and inferior end plates
	L3	NA
	L4	Burst, minor inferior aspect of left pedicle
7542	L2	Minor superior end plate
	L3	Minor superior end plate
	L4	Compression, superior end plate
7406	L2	NA
	L3	Burst, bilateral pedicle, spinous process
	L4	Bilateral pedicle, right lamina
7849	L2	NA
	L3	Burst, right lamina, spinous process
	L4	Compression, superior end plate, separation of pedicles, left lamina, spinous process
7654	L2	Burst
	L3	NA
	L4	Inferior end plate
7282	L2	NA
	L3	Pedicle separation
	L4	Burst
7469	L2	Minor bilateral pedicle
	L3	Burst
	L4	NA
7380	L2	NA
	L3	Compression, superior and inferior end plate
	L4	Burst
7058	L2	Burst
	L3	NA
	L4	Inferior end plate
7834	L2	Burst
	L3	NA
	L4	Inferior end plate
2366	L2	Burst
	L3	NA
	L4	NA
7607	L2	Burst
	L3	NA
	L4	Burst

Table C-1. Details of lumbar spine damage

Specimen		Damage
PMHS #	Level	
7727	L2	Burst
	L3	NA
	L4	Compression, superior and inferior end plate
L7034	L2	Compression, inferior end plate
	L3	Compressive, superior and inferior end plate
	L4	Compression, inferior end plate

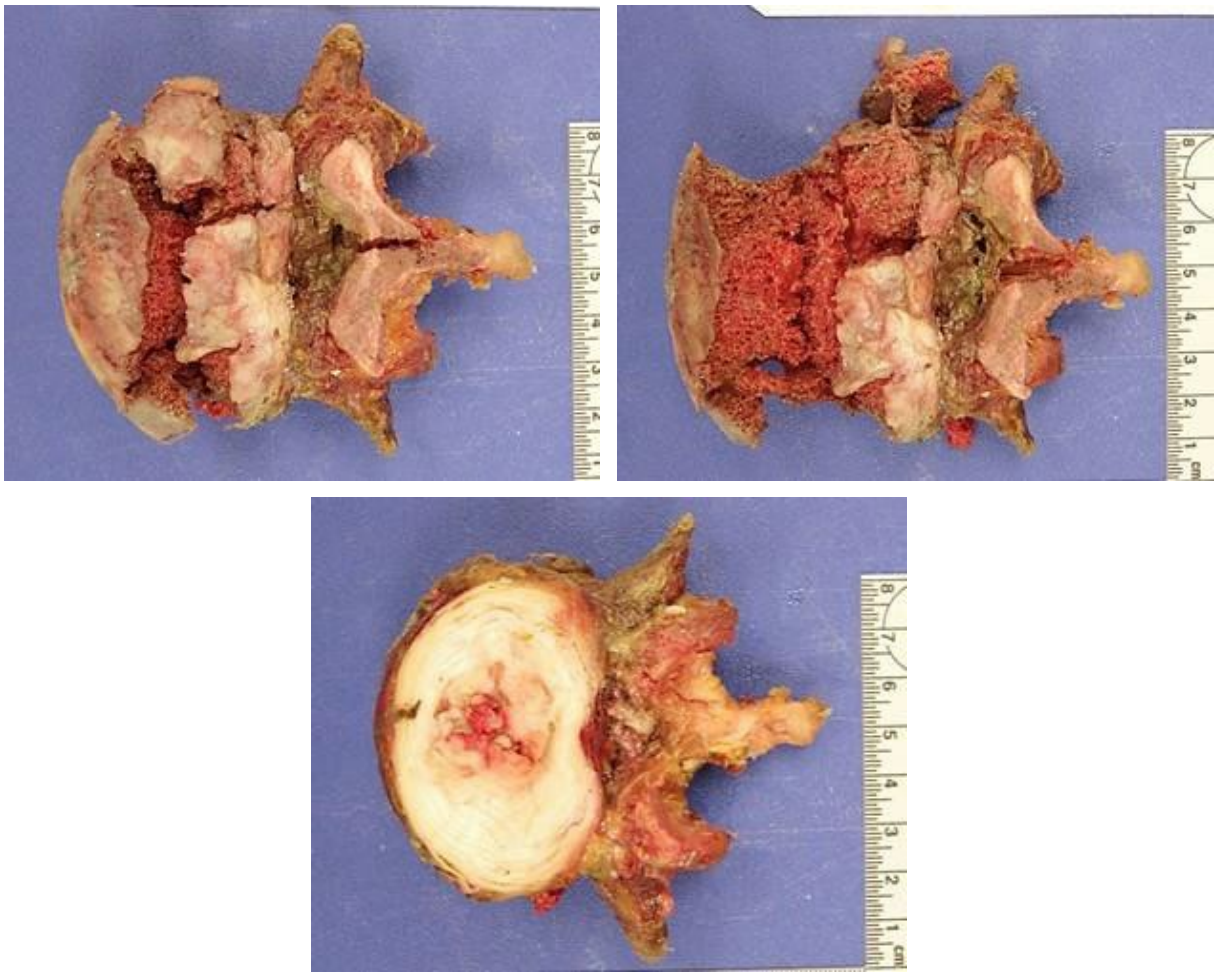

Figure C-1. Lumbar spine damage to PMHS7409: L4 inferior perspectives (top left and right) and inferior perspective (bottom)

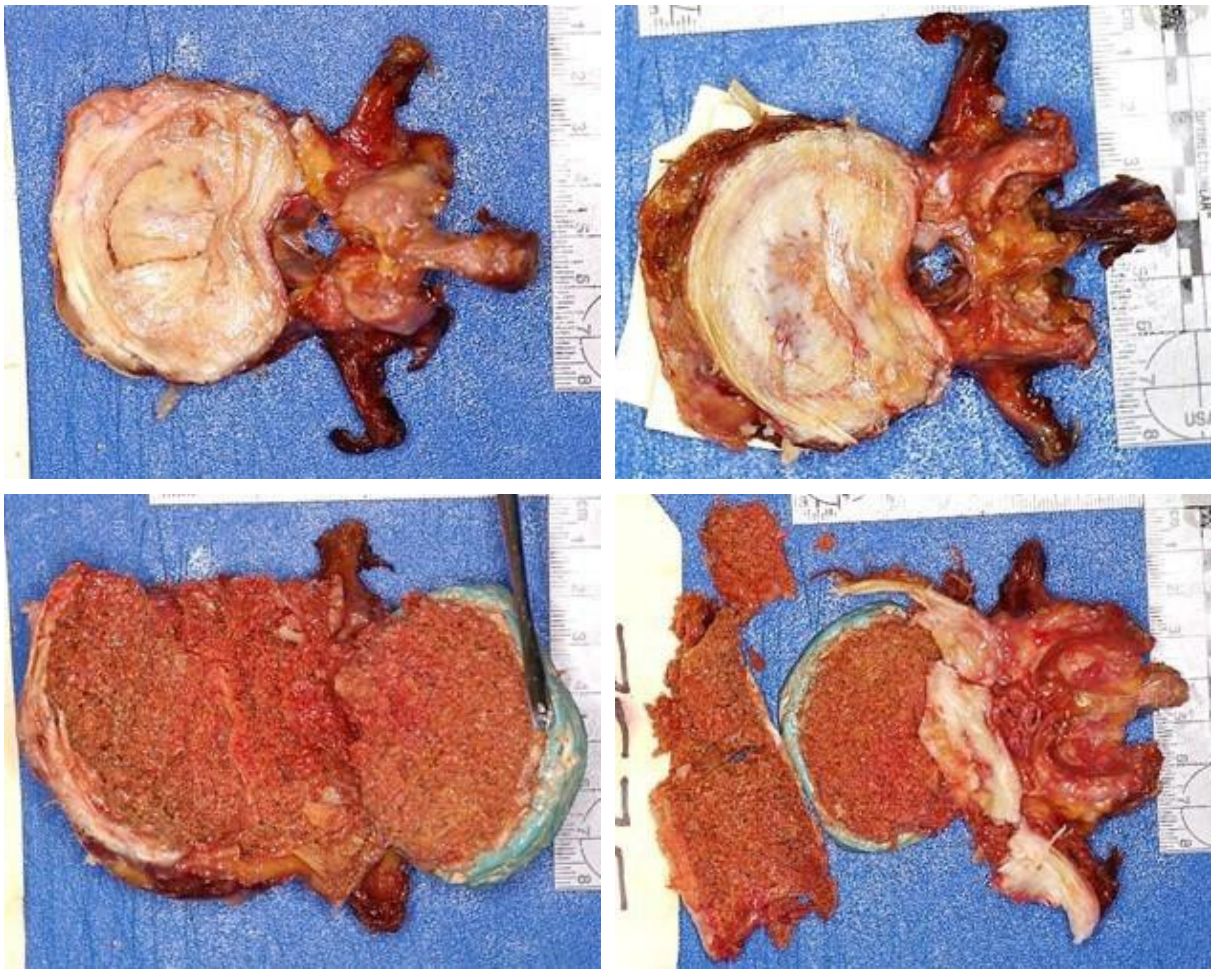

Figure C-2. Lumbar spine damage to PMHS7575: L2 inferior and superior perspectives (top left and right) and L4 inferior and superior perspectives (bottom left and right)

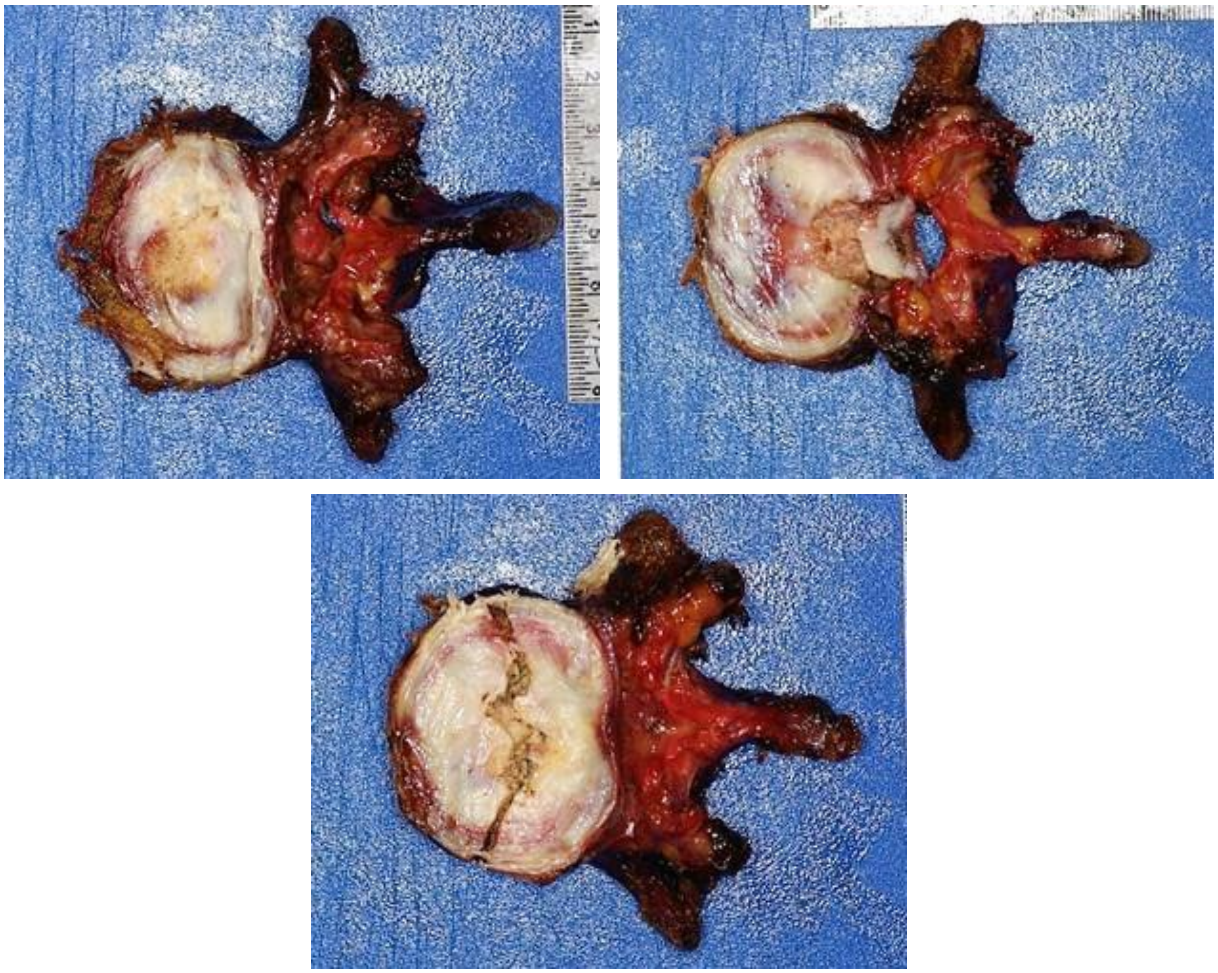

Figure C-3. Lumbar spine damage to PMHS7542: L2 superior perspective (top left), L3 inferior perspective (top right), and L4 superior perspective (bottom)

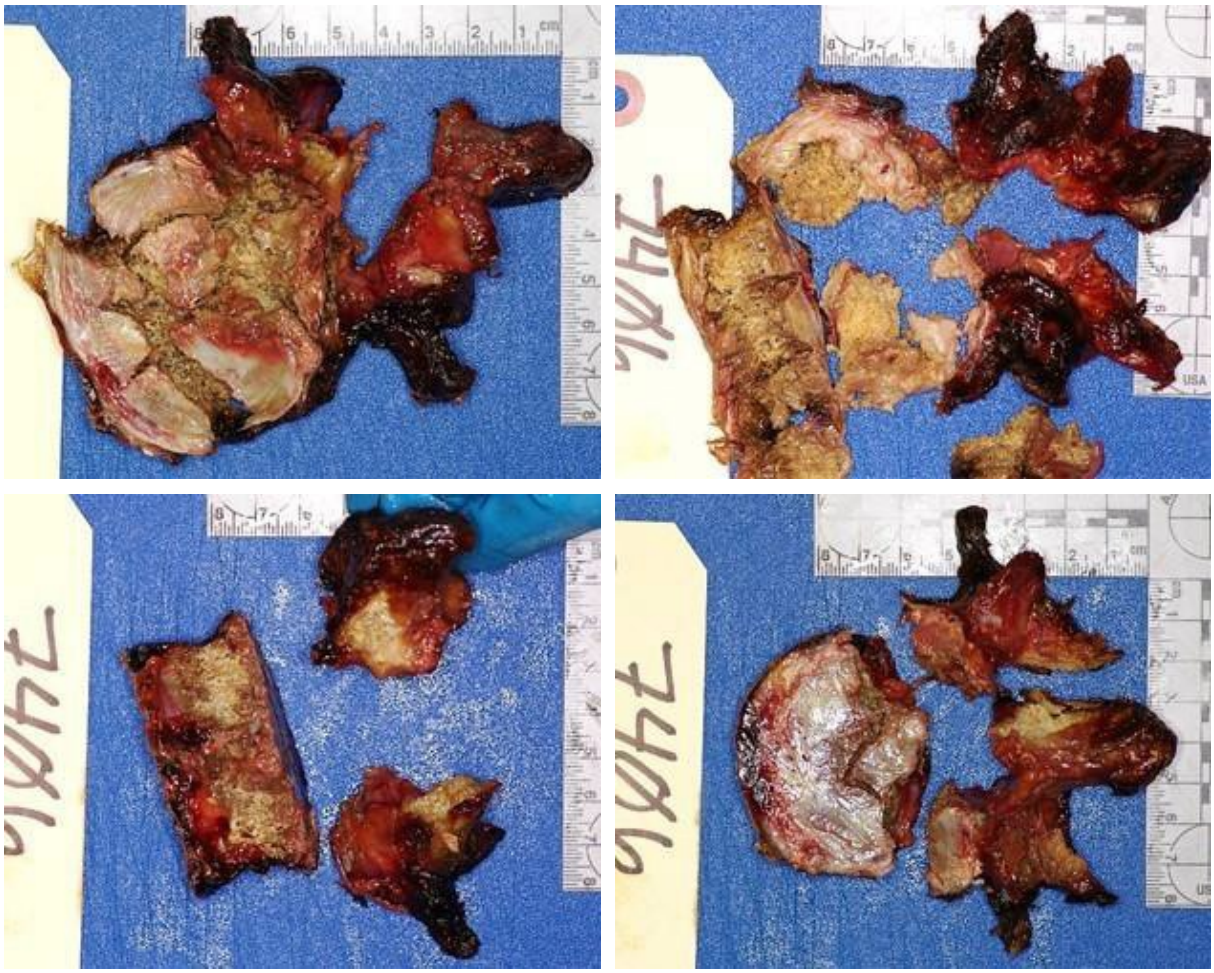

Figure C-4. Lumbar spine damage to PMHS7406: L3 inferior and section perspectives (top left and right) and L4 section and superior perspectives (bottom left and right)

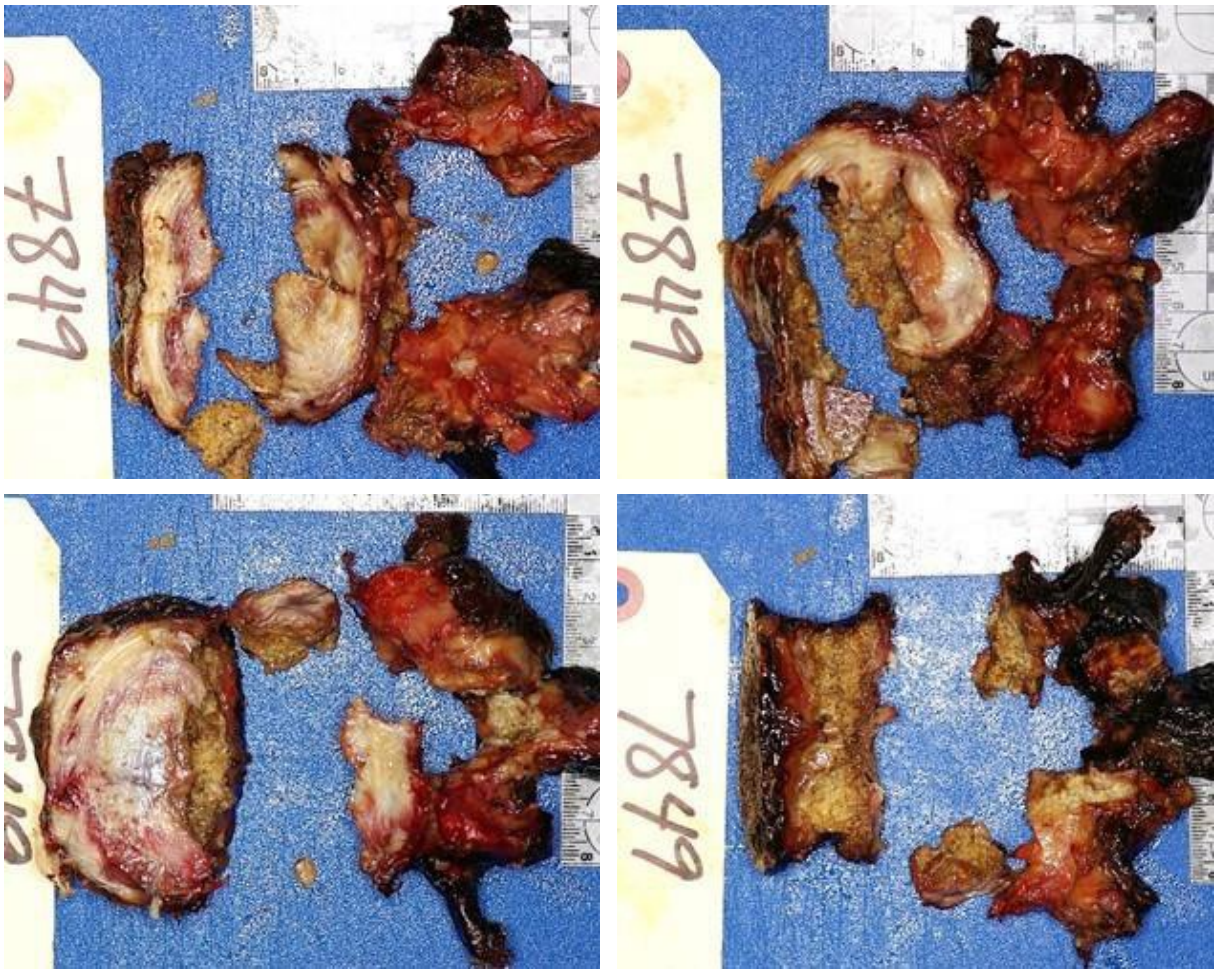

Figure C-5. Lumbar spine damage to PMHS7575: L3 inferior and superior perspectives (top left and right) and L4 inferior and section perspectives (bottom left and right)

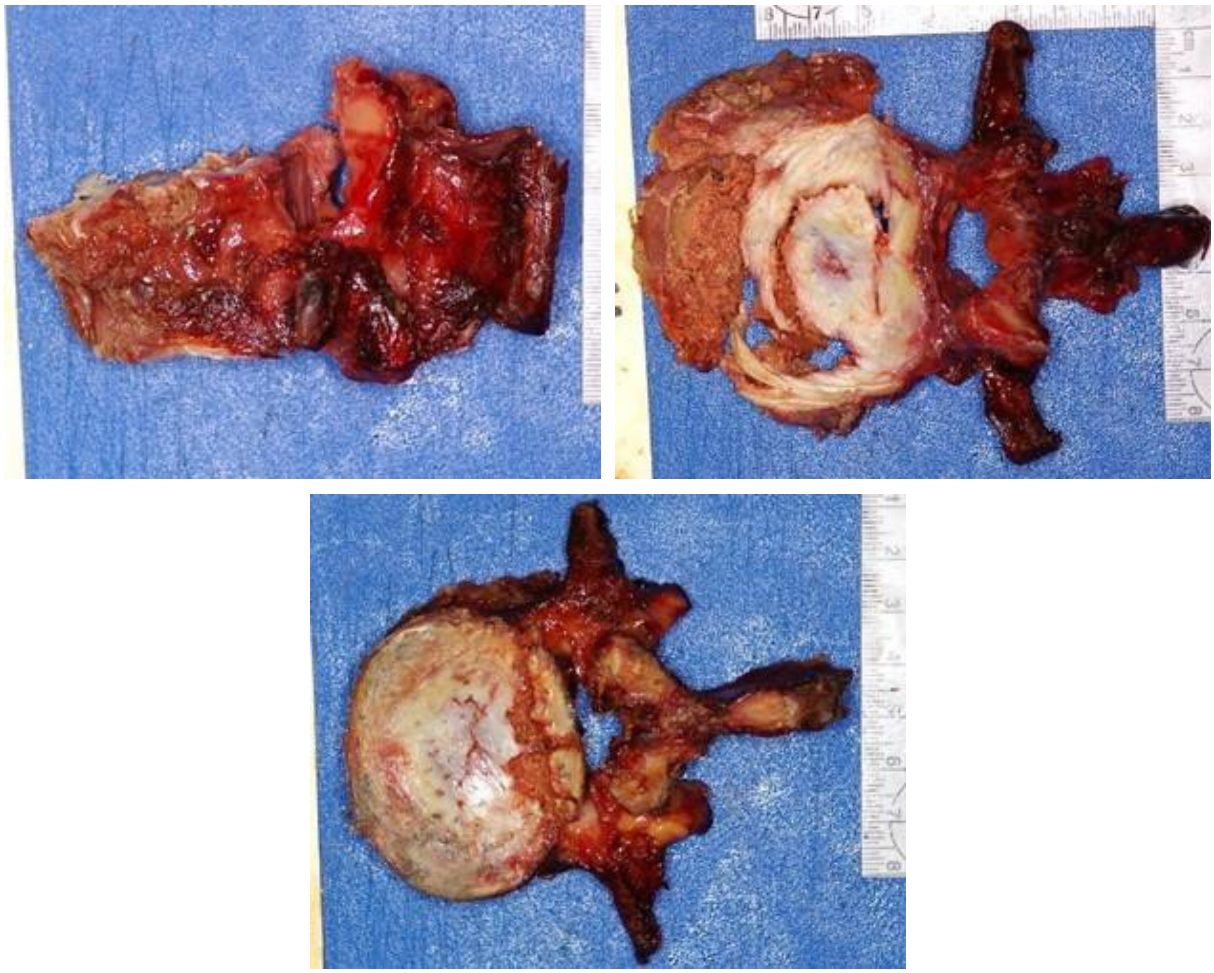

Figure C-6. Lumbar spine damage to PMHS7654: L2 section and superior perspectives (top left and right) and L4 inferior perspective (bottom)

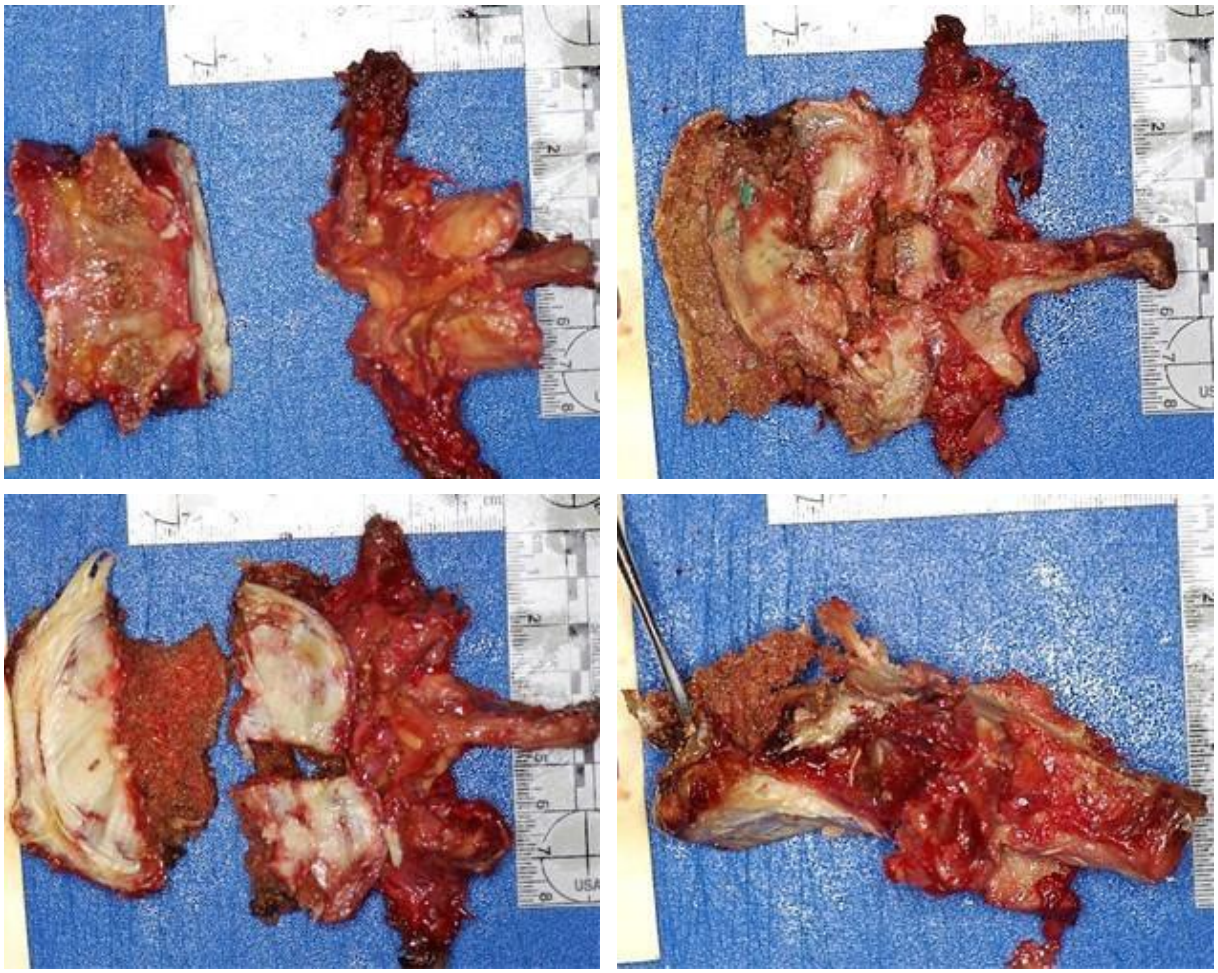

Figure C-7. Lumbar spine damage to PMHS7282: L3 section and superior perspectives (top left and right) and L4 inferior and section perspectives (bottom left and right)

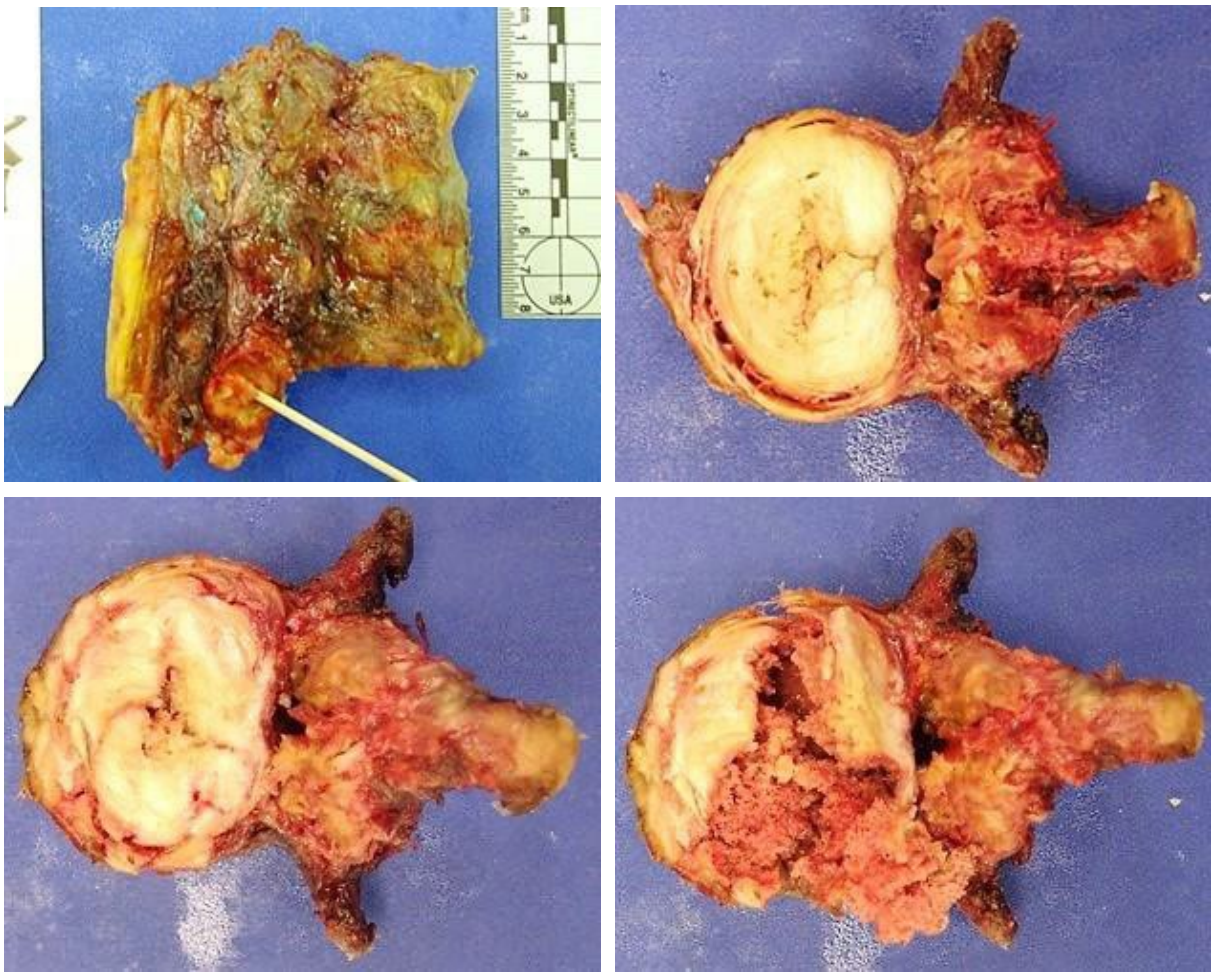

Figure C-8. Lumbar spine damage to PMHS7469: L2 superior perspective (top left), L3 superior (top right), and two L3 inferior perspectives (bottom left and right)

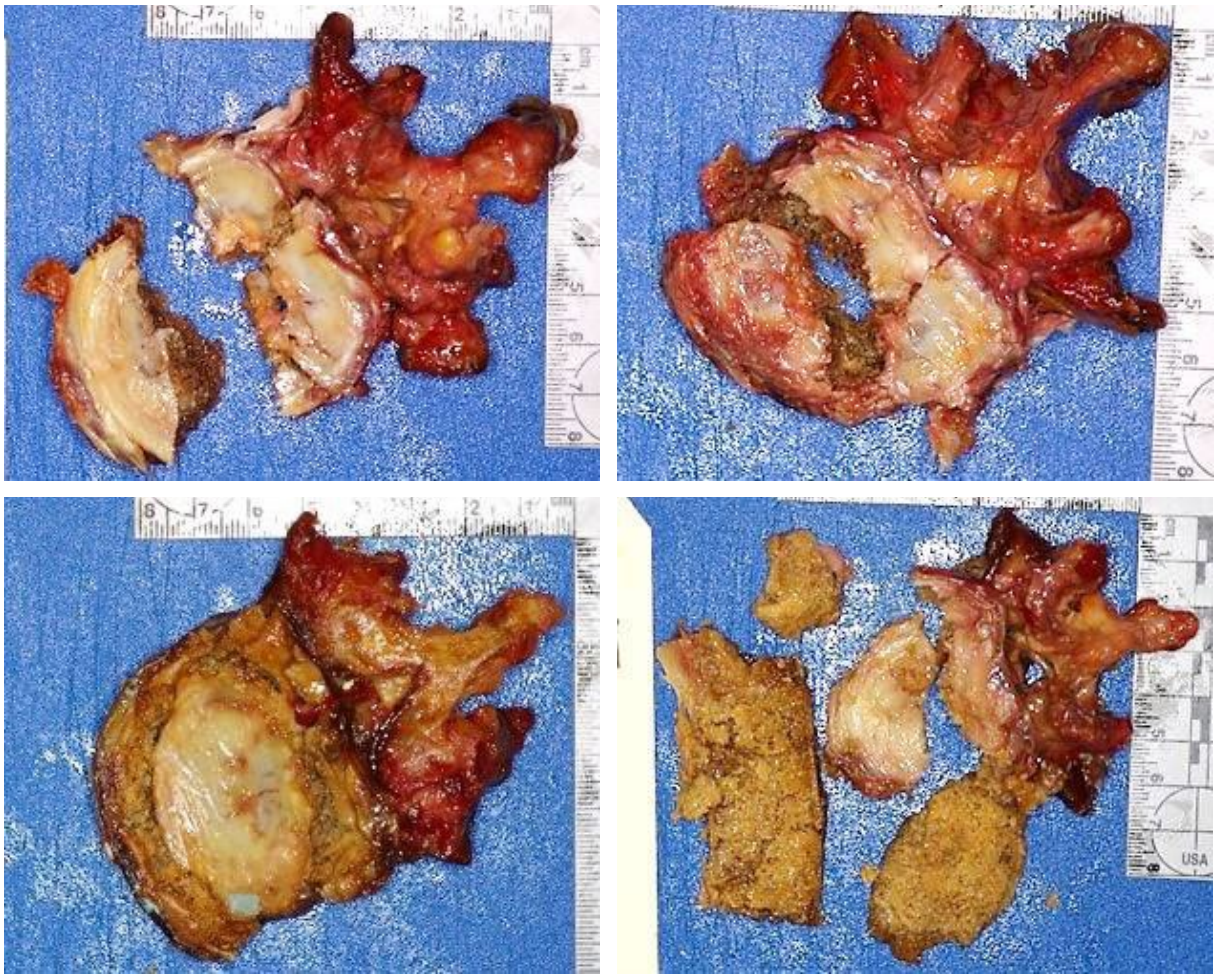

Figure C-9. Lumbar spine damage to PMHS7380: L3 inferior and superior perspectives (top left and right), and L4 inferior and superior perspectives (bottom left and right)

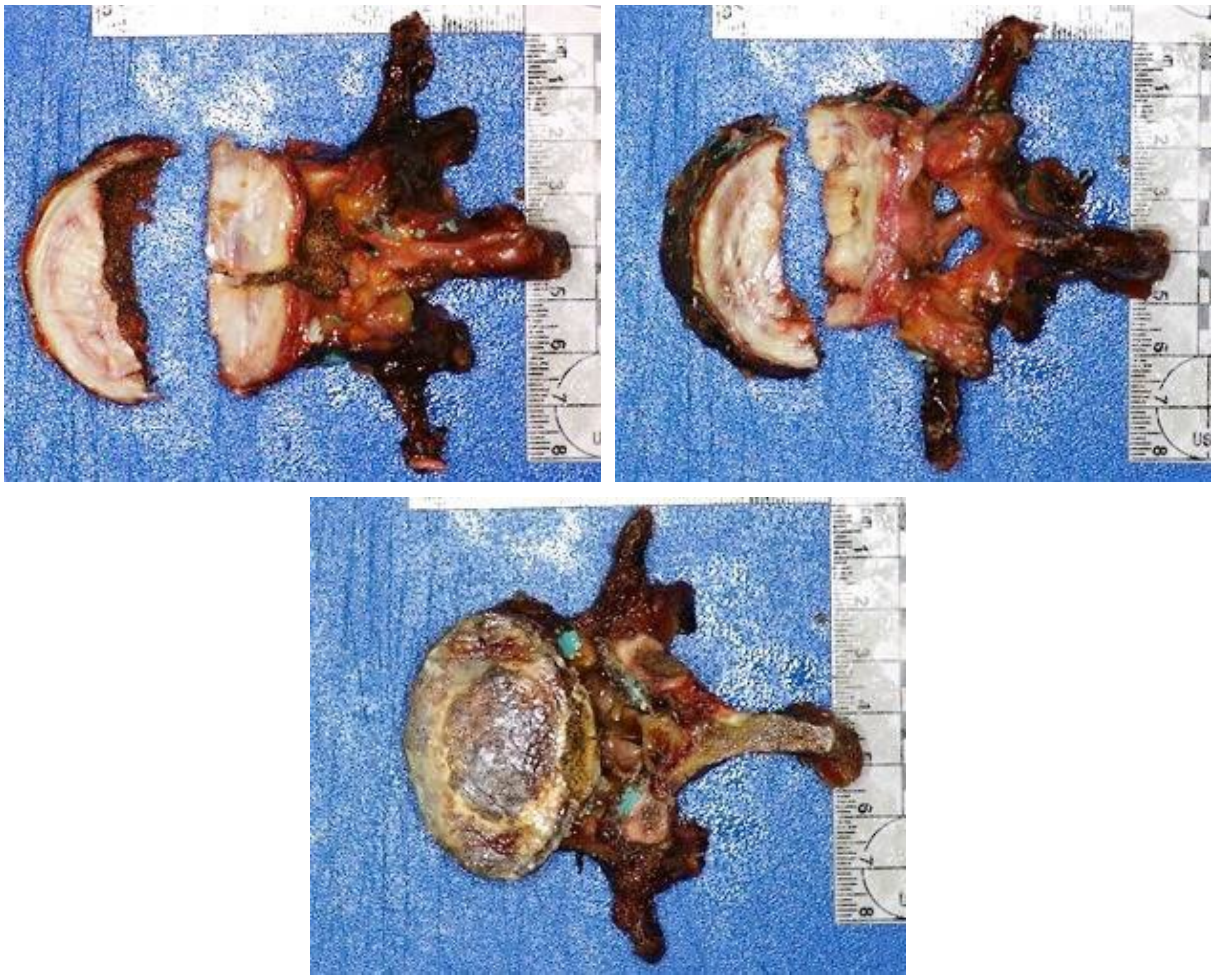

Figure C-10. Lumbar spine damage to PMHS7058: L2 inferior and superior perspectives (top left and right), and L4 inferior perspective (bottom)

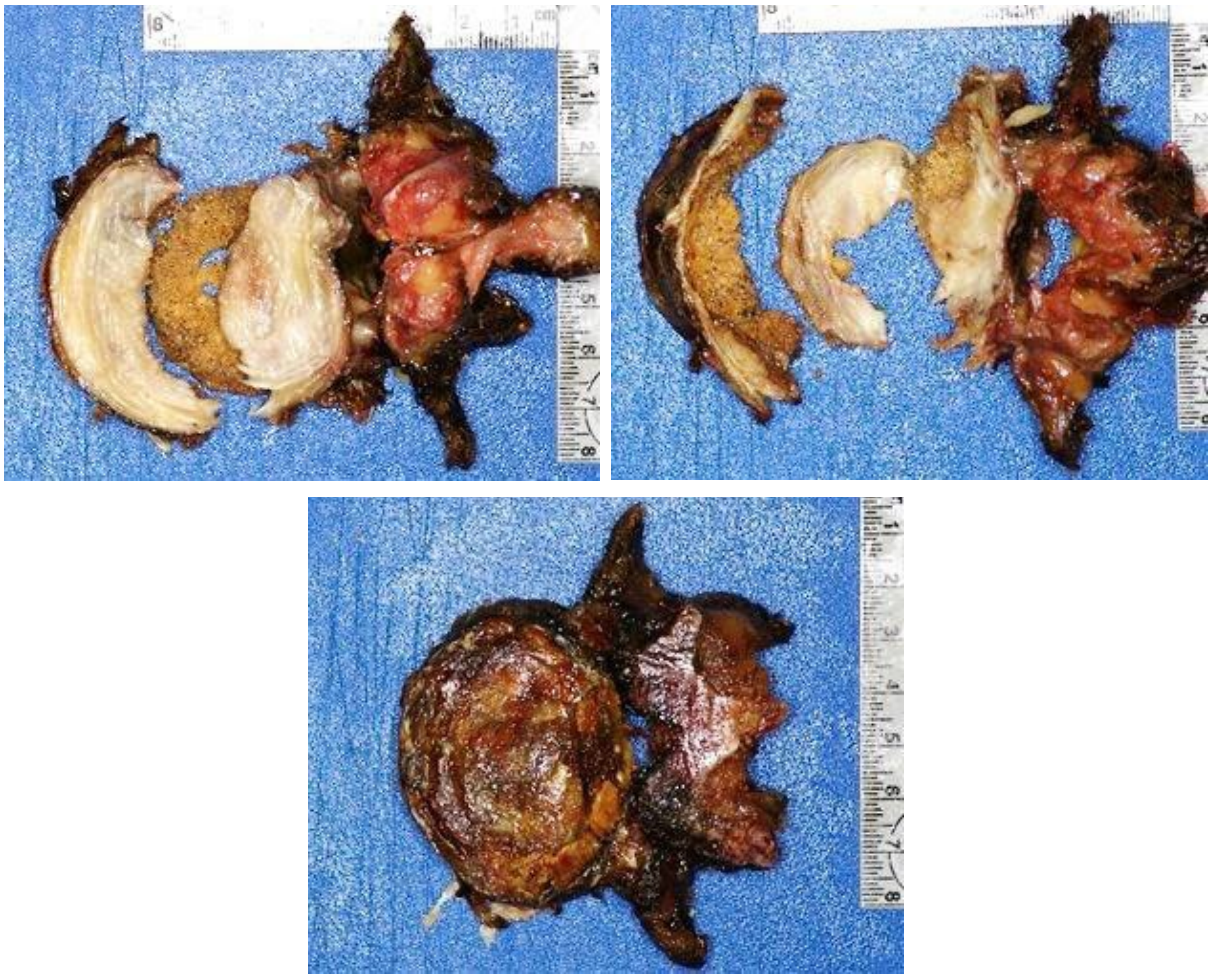

Figure C-11. Lumbar spine damage to PMHS7834: L2 inferior and superior perspectives (top left and right), and L4 inferior perspective (bottom)

Figure C-12. Lumbar spine damage to PMHS2366 and L4 superior perspective (TRR6)

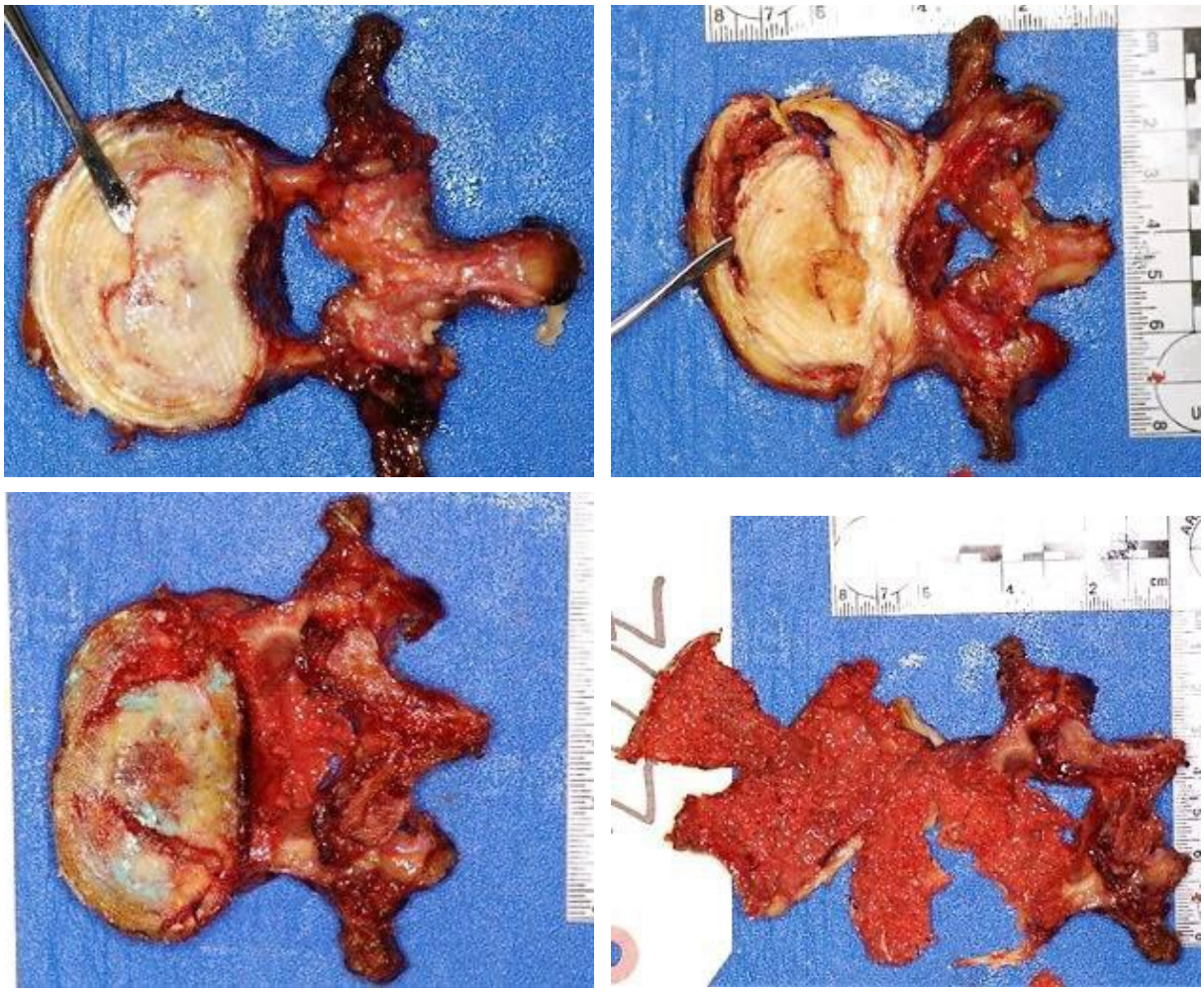

Figure C-13. Lumbar spine damage to PMHS7607: L2 superior perspective (top left), L4 superior perspective (top right), and two L4 inferior perspectives (bottom left and right)

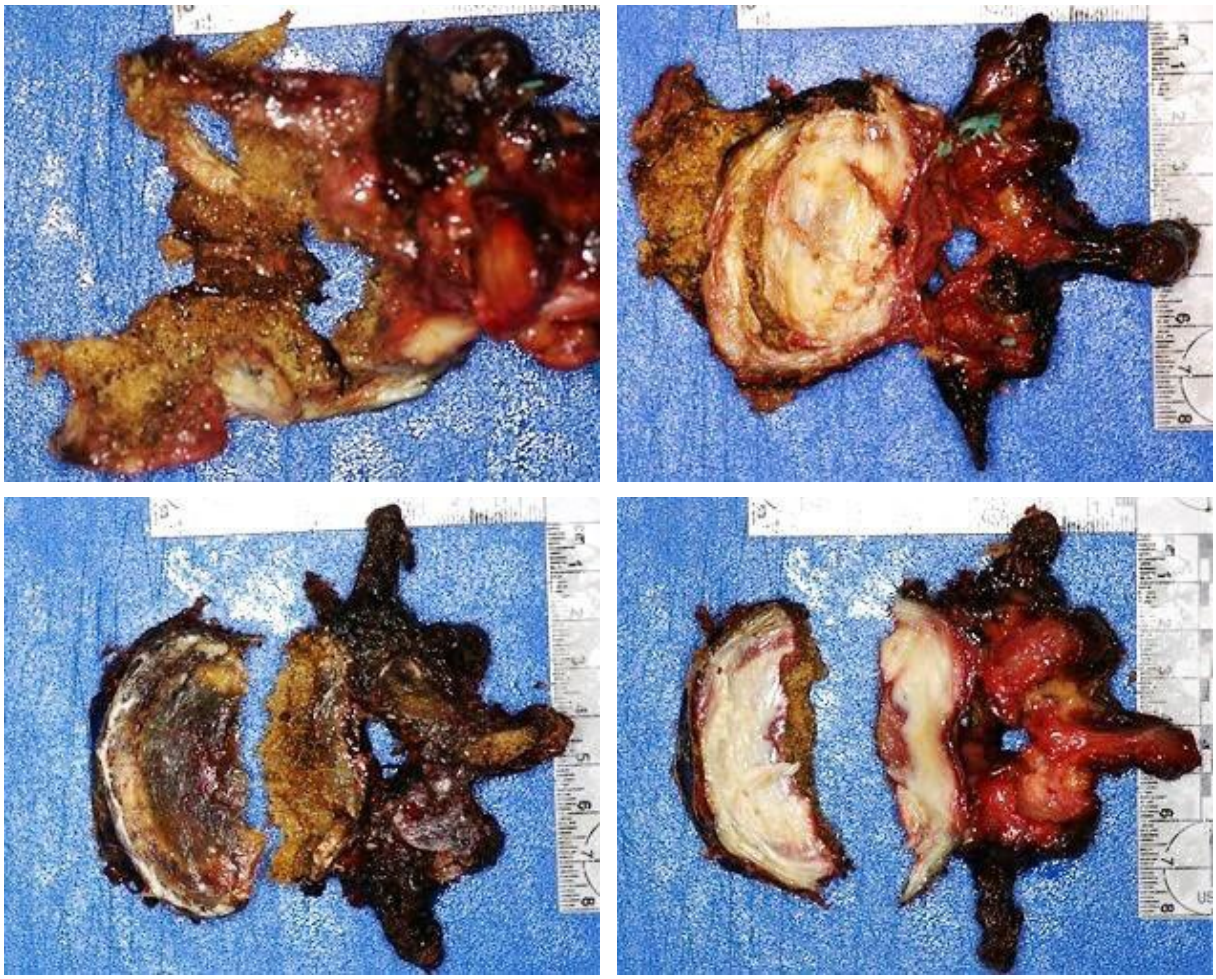

Figure C-14. Lumbar spine damage to PMHS7727: L2 inferior and superior perspectives (top left and right), and L4 inferior perspectives (bottom left and right)

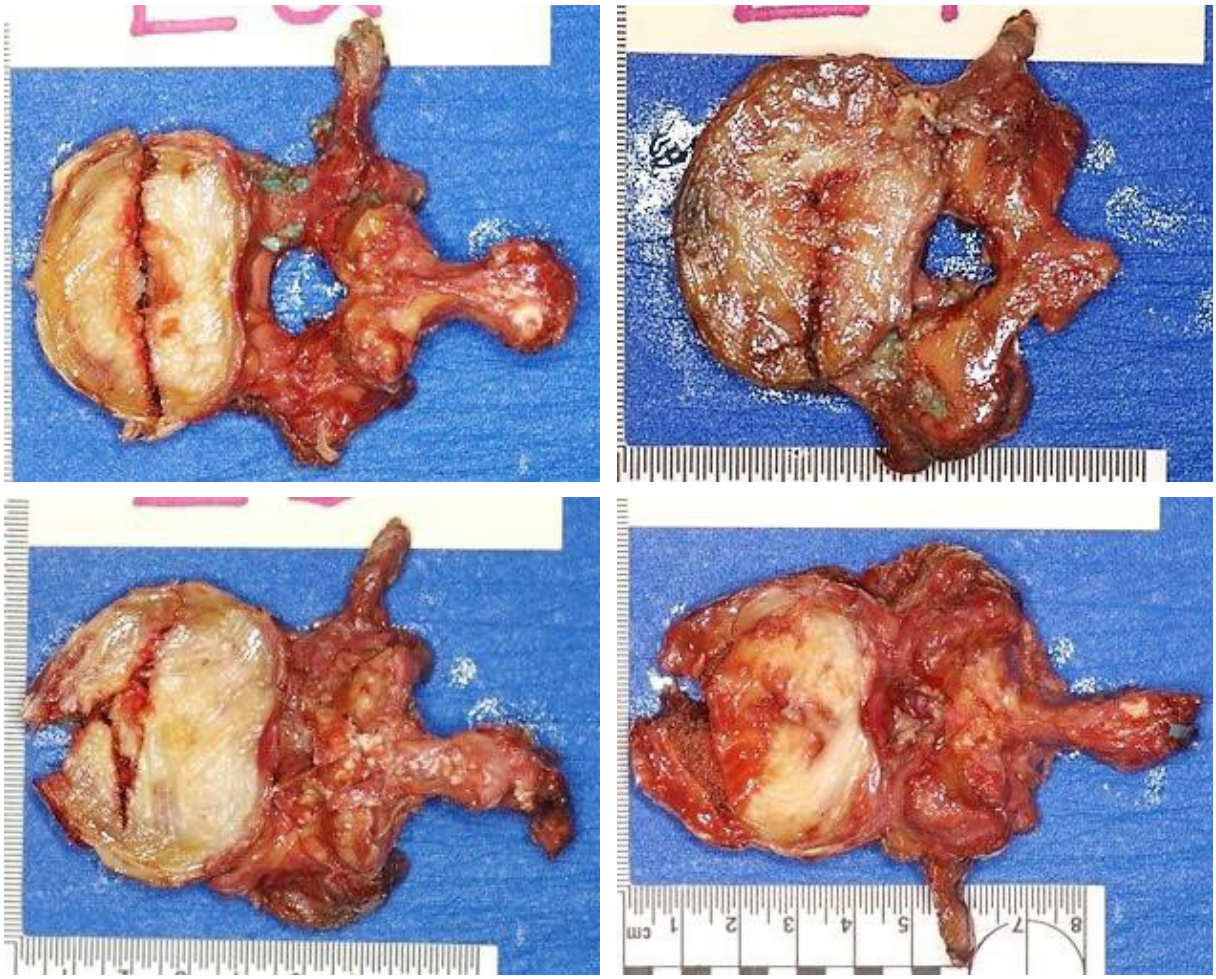

Figure C-15. Lumbar spine damage to PMHSL7034: L2 inferior perspective (top left), L4 inferior perspective (top right), and L3 inferior and superior perspectives (bottom left and right)

Appendix D – Catalog of Left Tibia Mid-diaphysis Fractures

Figure D-1. Early stages of left tibia mid-diaphysis fracture of PMHS7409

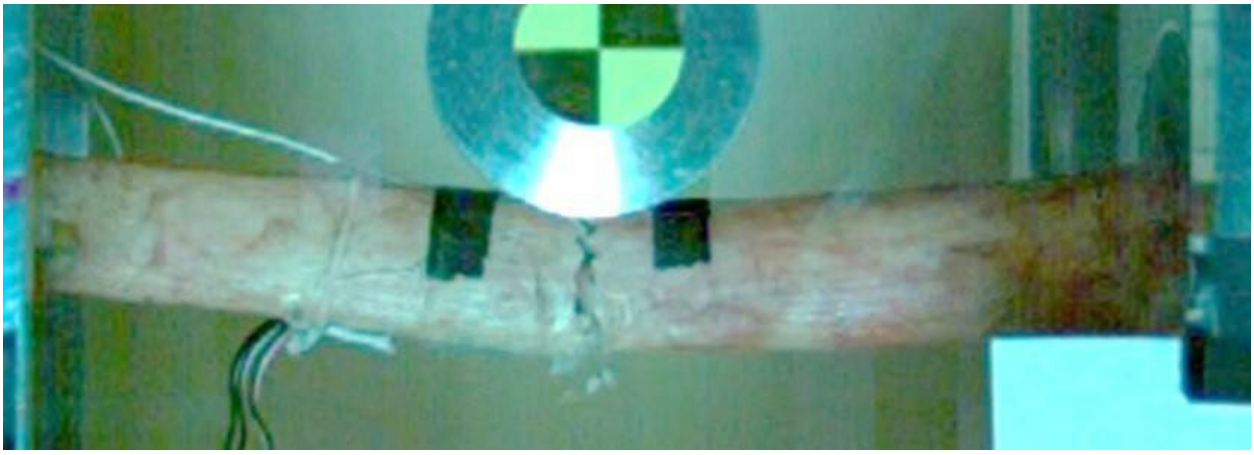

Figure D-2. Early stages of left tibia mid-diaphysis fracture of PMHS7575

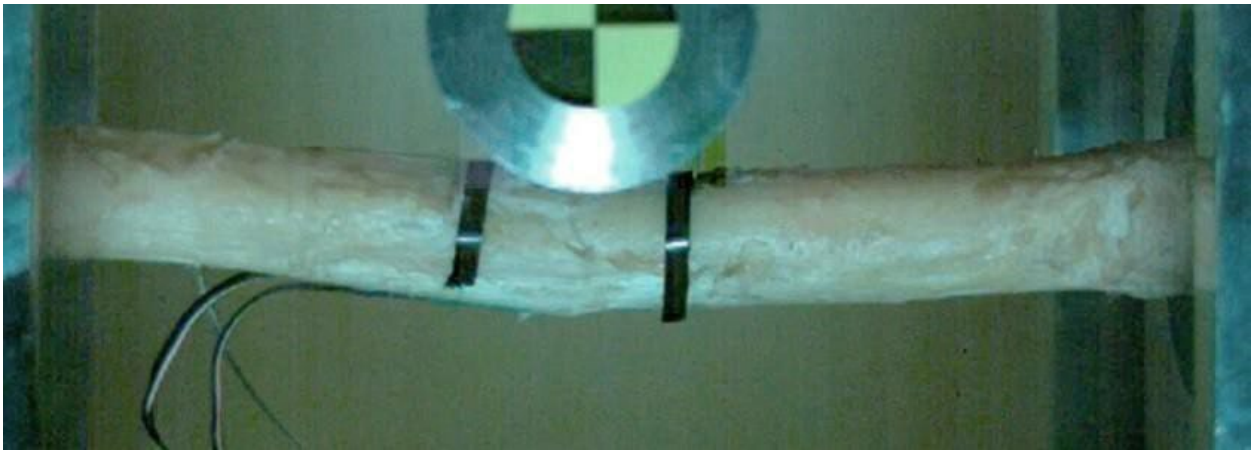

Figure D-3. Early stages of left tibia mid-diaphysis fracture of PMHS7542

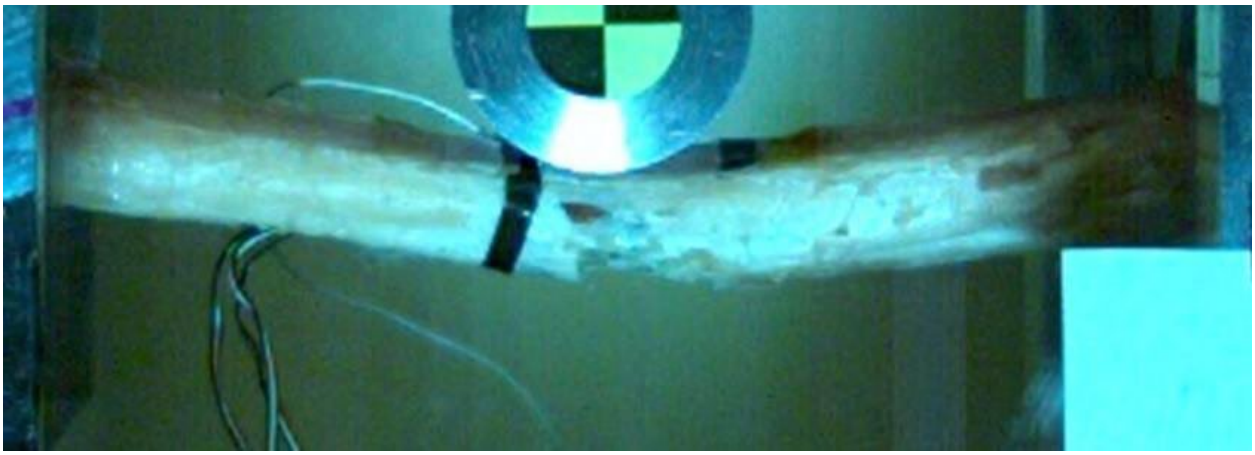

Figure D-4. Middle stages of left tibia mid-diaphysis fracture of PMHS7805

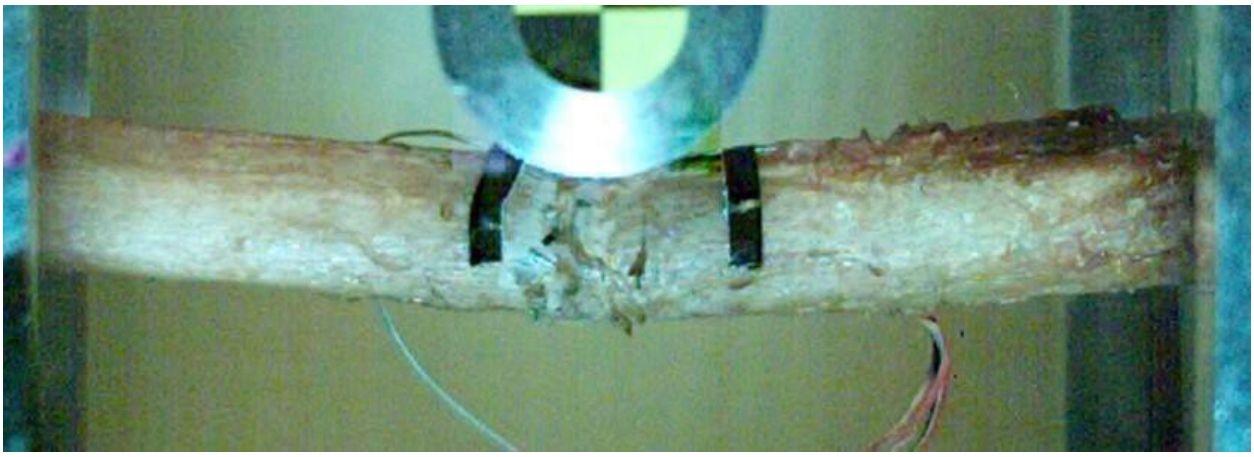

Figure D-5. Early stages of left tibia mid-diaphysis fracture of PMHS7406

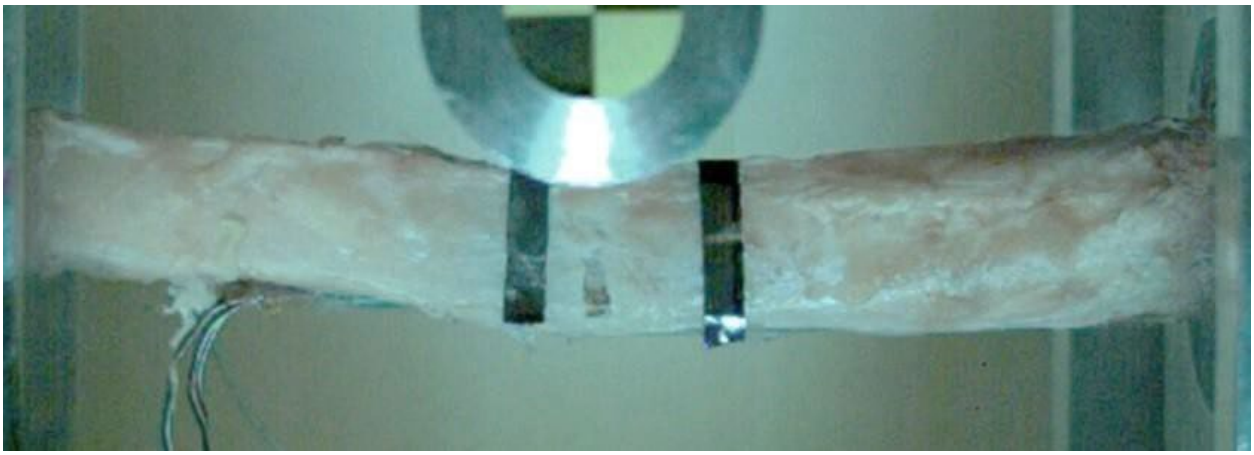

Figure D-6. Early stages of left tibia mid-diaphysis fracture of PMHS7849

Figure D-7. Early stages of left tibia mid-diaphysis fracture of PMHS9584M

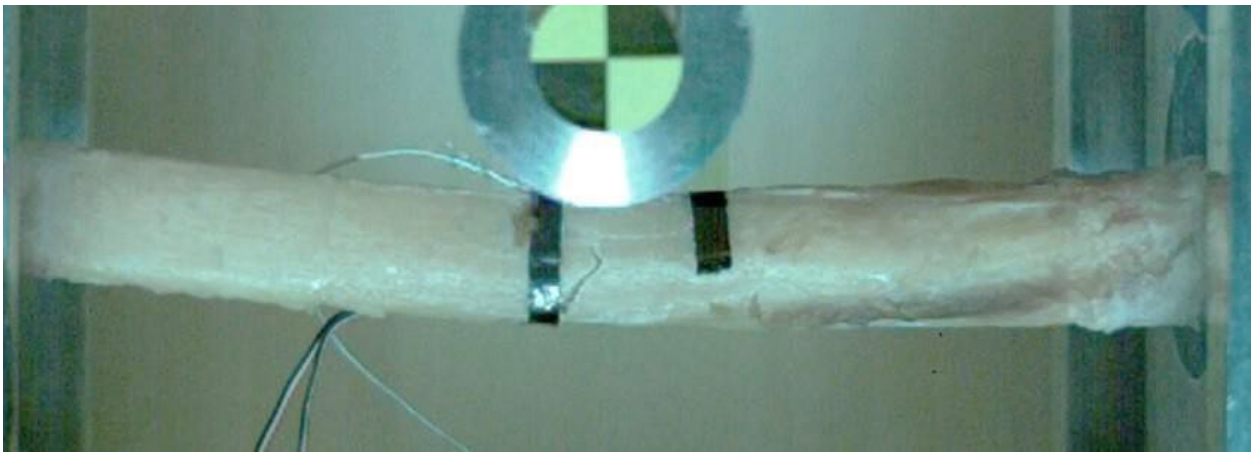

Figure D-8. Early stages of left tibia mid-diaphysis fracture of PMHS7654

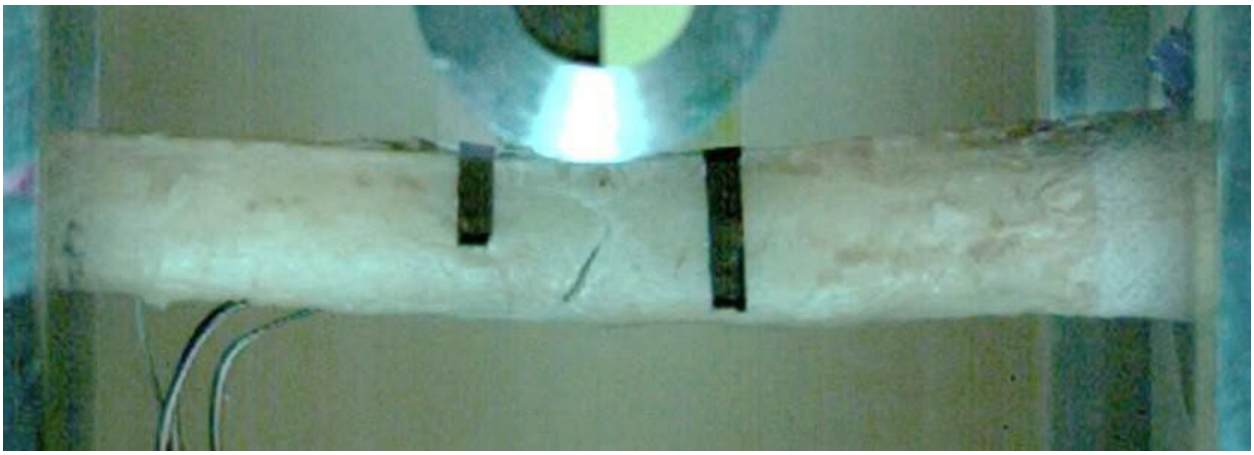

Figure D-9. Early stages of left tibia mid-diaphysis fracture of PMHS7282

Figure D-10. Early stages of left tibia mid-diaphysis fracture of PMHS7469

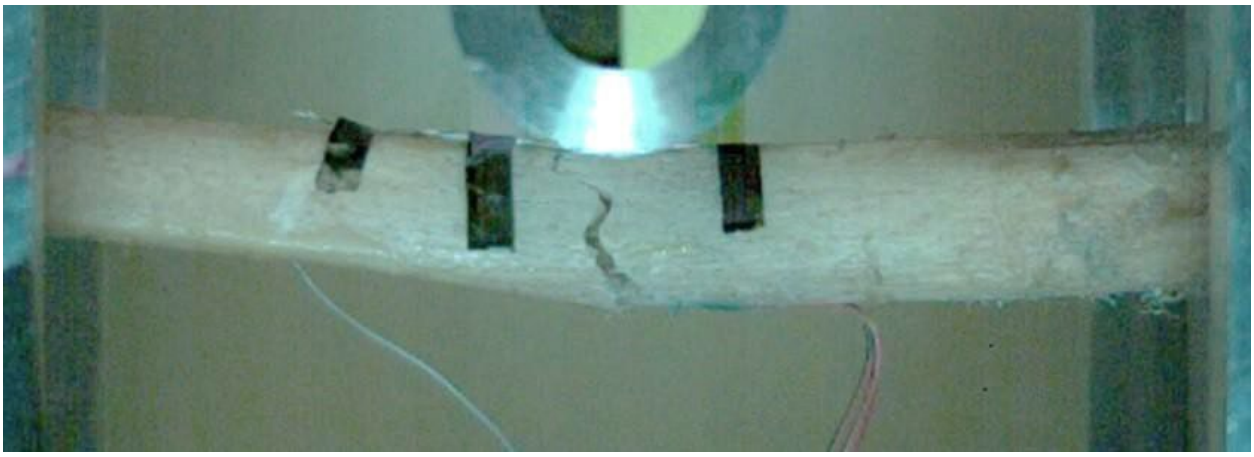

Figure D-11. Early stages of left tibia mid-diaphysis fracture of PMHS7618

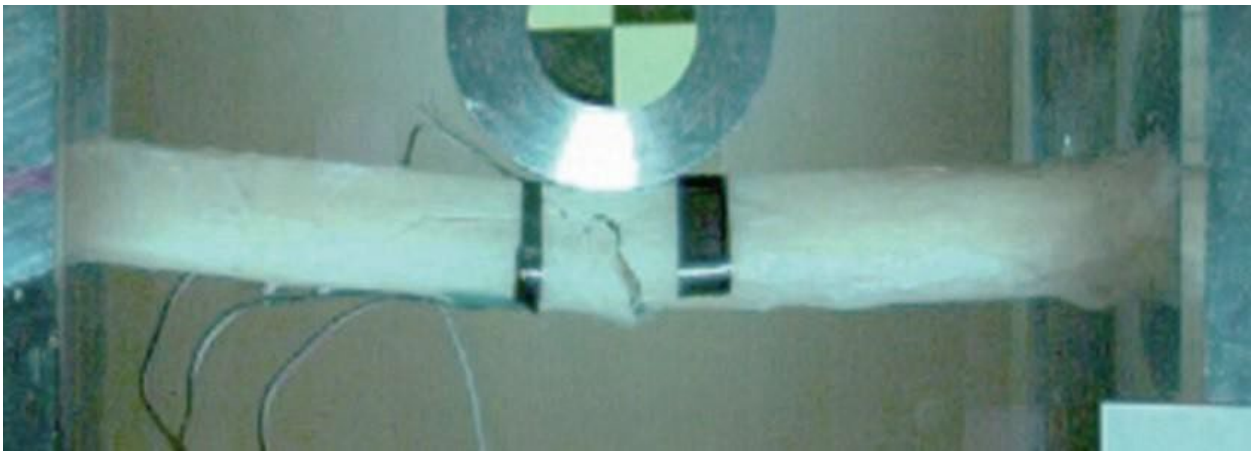

Figure D-12. Early stages of left tibia mid-diaphysis fracture of PMHS7058

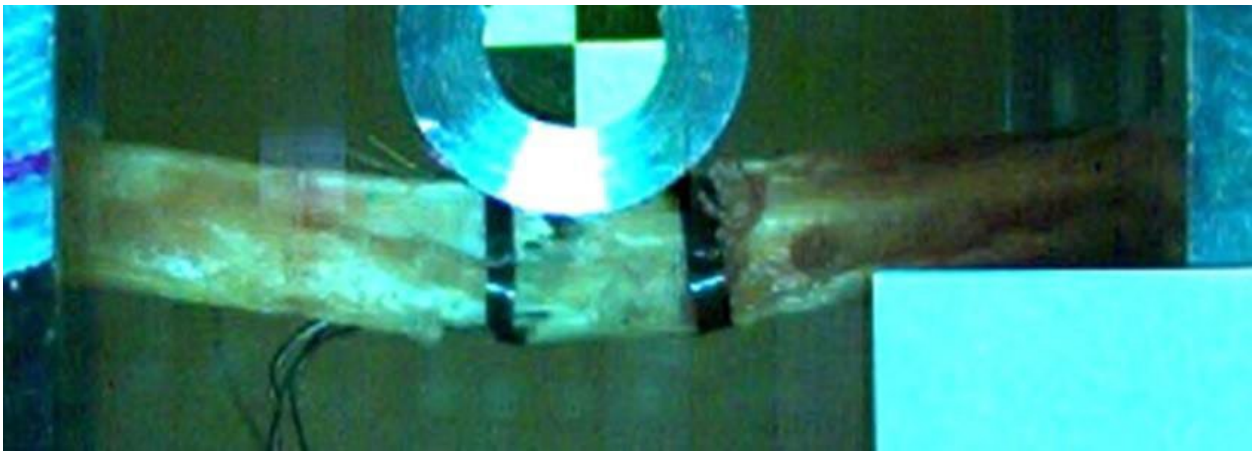

Figure D-13. Early stages of left tibia mid-diaphysis fracture of PMHS7834

Figure D-14. Early stages of left tibia mid-diaphysis fracture of PMHS2366

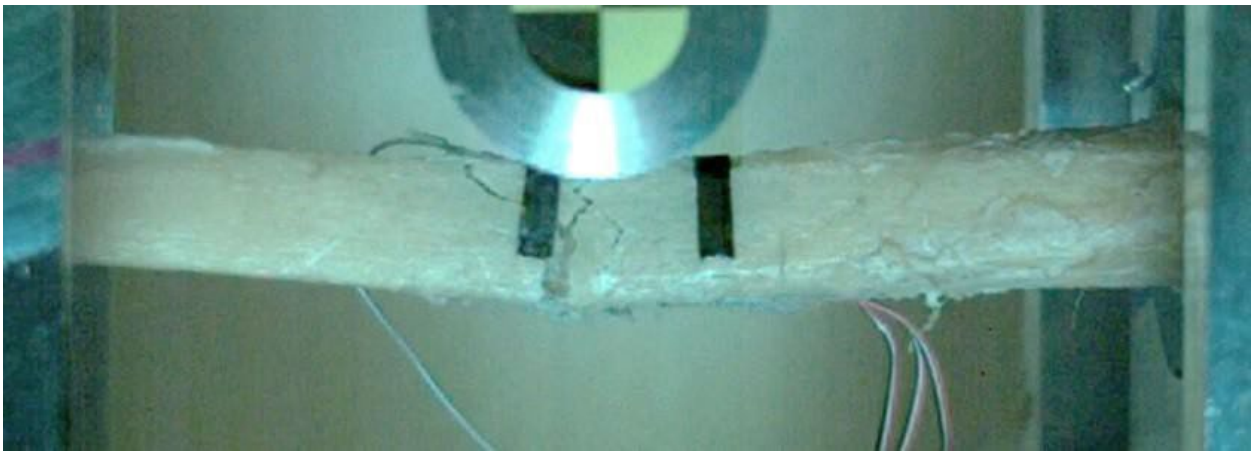

Figure D-15. Early stages of left tibia mid-diaphysis fracture of PMHS7607

Figure D-16. Early stages of left tibia mid-diaphysis fracture of PMHS7630

Figure D-17. Early stages of left tibia mid-diaphysis fracture of PMHS0509

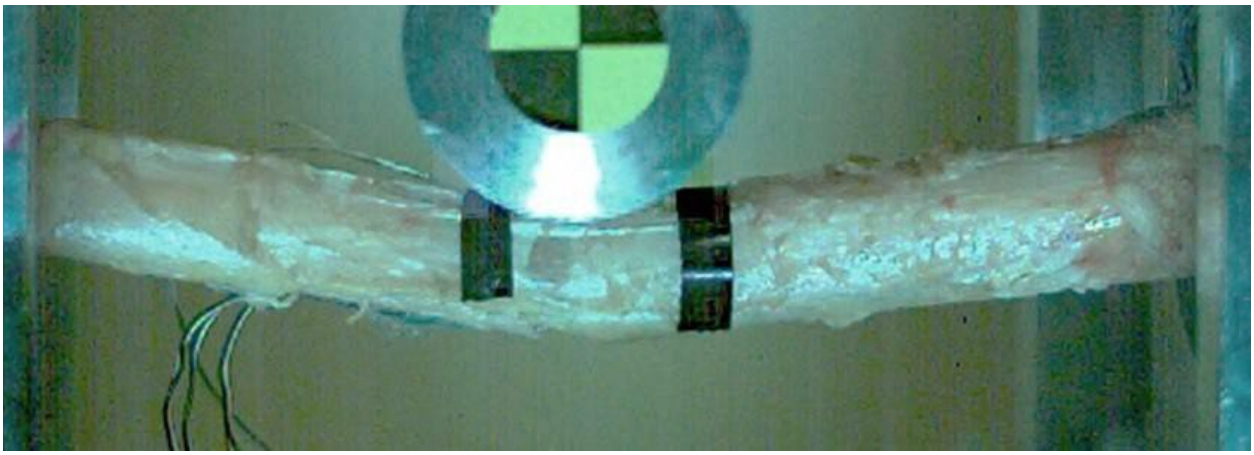

Figure D-18. Early stages of left tibia mid-diaphysis fracture of PMHS7727

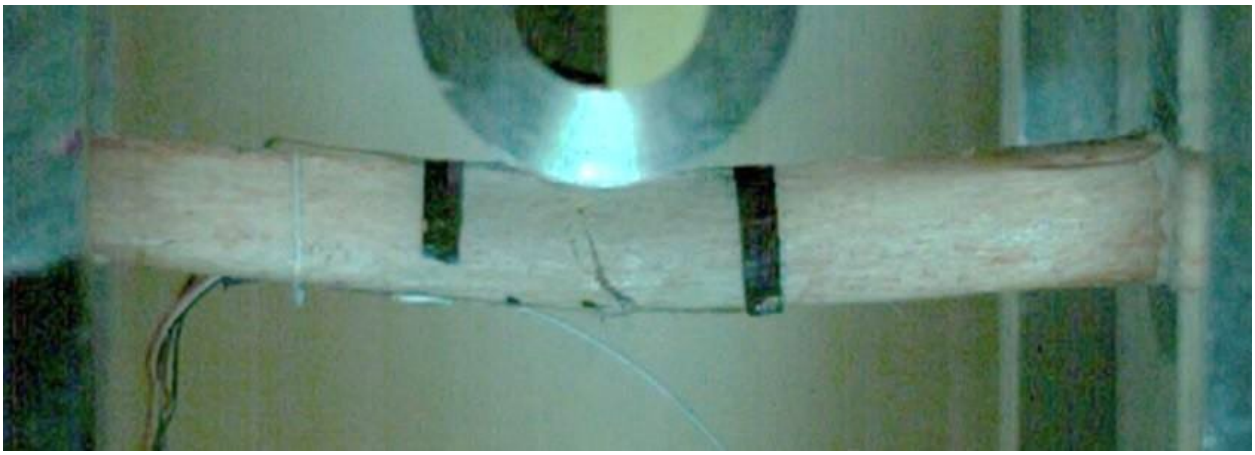

Figure D-19. Early stages of left tibia mid-diaphysis fracture of PMHSL7034

Appendix E – Catalog of Sacrum/Pelvis Fracture Characteristics

Table E-1. Sacrum/pelvis fractures and fracture sequence

Specimen		Damage
PMHS #	Sequence	
7654	1	L5/S1 compression
	2	Left costal elements
	3	Left alae
	4	Right alae
	5	Right costal elements
7575	1	Right costal elements
	2	Left costal elements
7542	1	Left costal elements
	2	Right SI joint involvement/Ilium
	3	Right costal elements and right alae
7849	1	Right costal elements, left alae
	2	Left and right alae near promontory
7406	1	L5 compressed, left alae
	2	Left alae near promontory
7282	1	Left inferior ramus, left ischium
7380	1	Bilateral alae, bilateral ilium
	2	Left costal elements
	3	Right costal elements
7618	1	Left costal elements
7834	1	Bilateral costal elements
	2	Bilateral alae
7607	1	Right costal elements, right alae
	2	Left costal elements, left alae
7630	1	Right costal elements
	2	Bilateral alae
	3	Left alae complete
	4	Left costal elements
7727	1	Left SI joint involvement, left ilium
L7034	1	Right costal elements
	2	Right alae, left alae near promontory
	3	Right alae/costal elements complete

Figure E-1. Sacrum/pelvis damage for PMHS7654: Pelvic perspective (top left), dorsal sacrum (top right), left costal elements (bottom left), and right costal elements (bottom right)

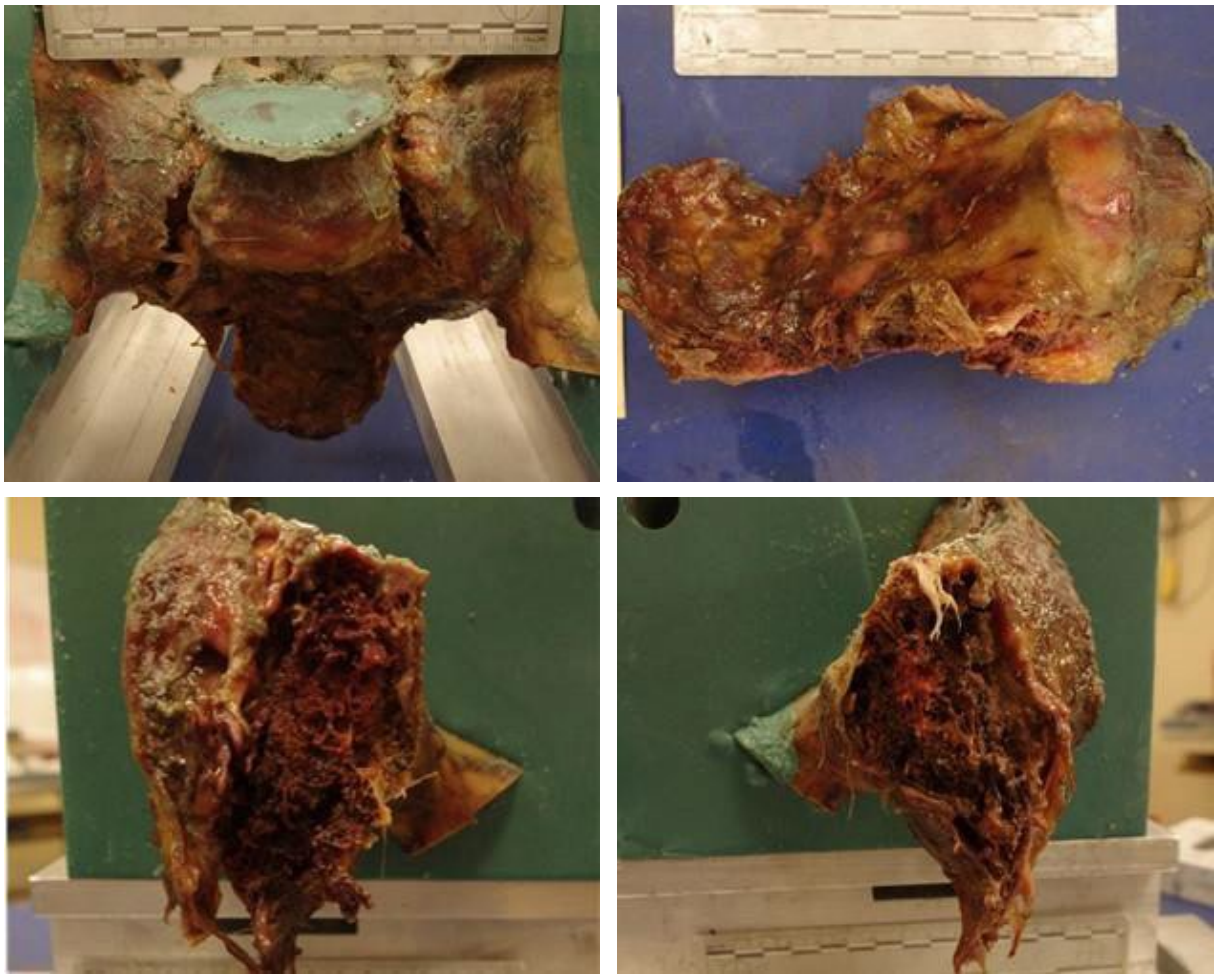

Figure E-2. Sacrum/pelvis damage for PMHS7575: Pelvic perspective (top left), pelvic sacrum perspective (top right), left costal elements (bottom left), and right costal elements (bottom right)

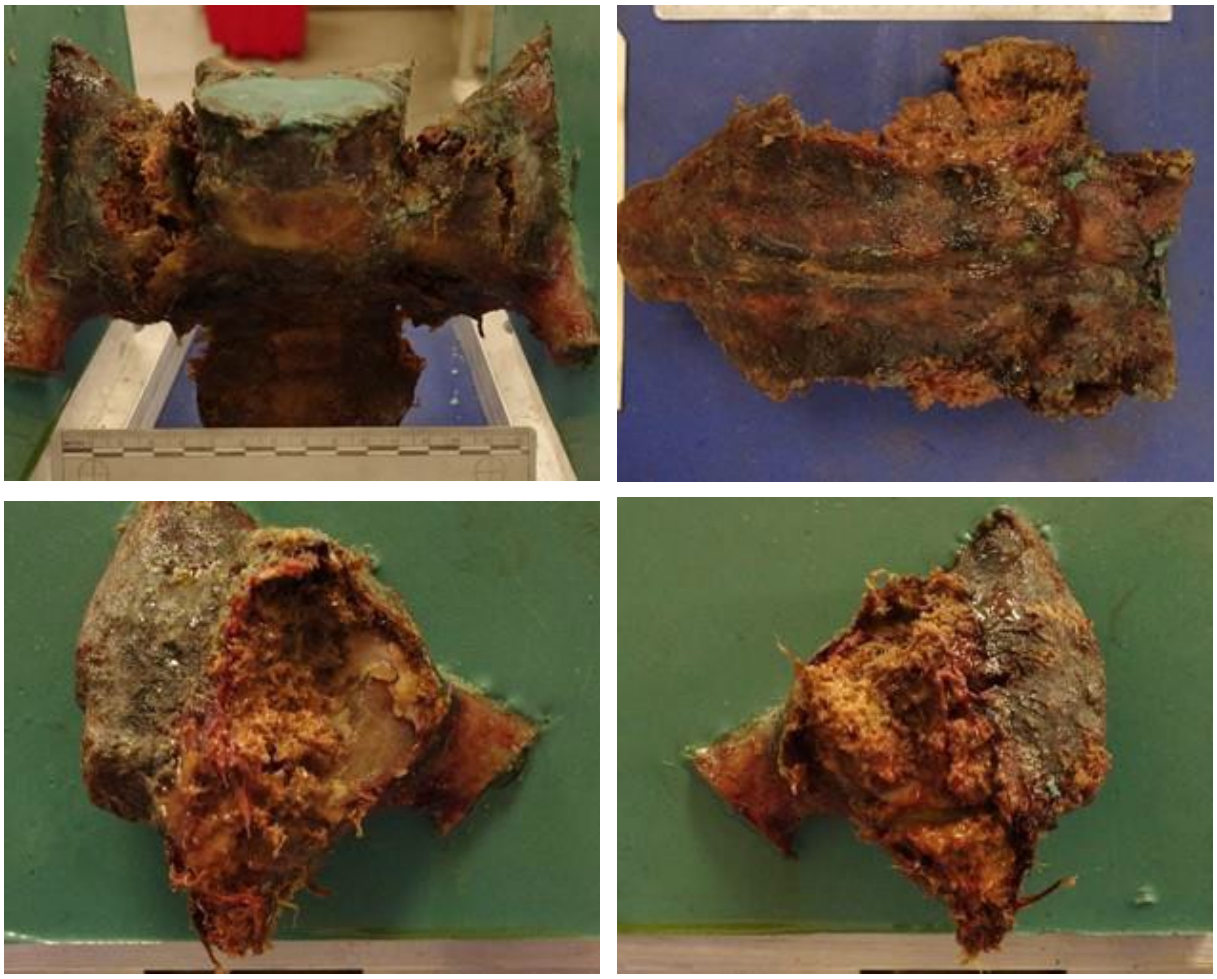

Figure E-3. Sacrum/pelvis damage for PMHS7542: Pelvic perspective (top left), dorsal sacrum perspective (top right), left costal elements (bottom left), and right costal elements (bottom right)

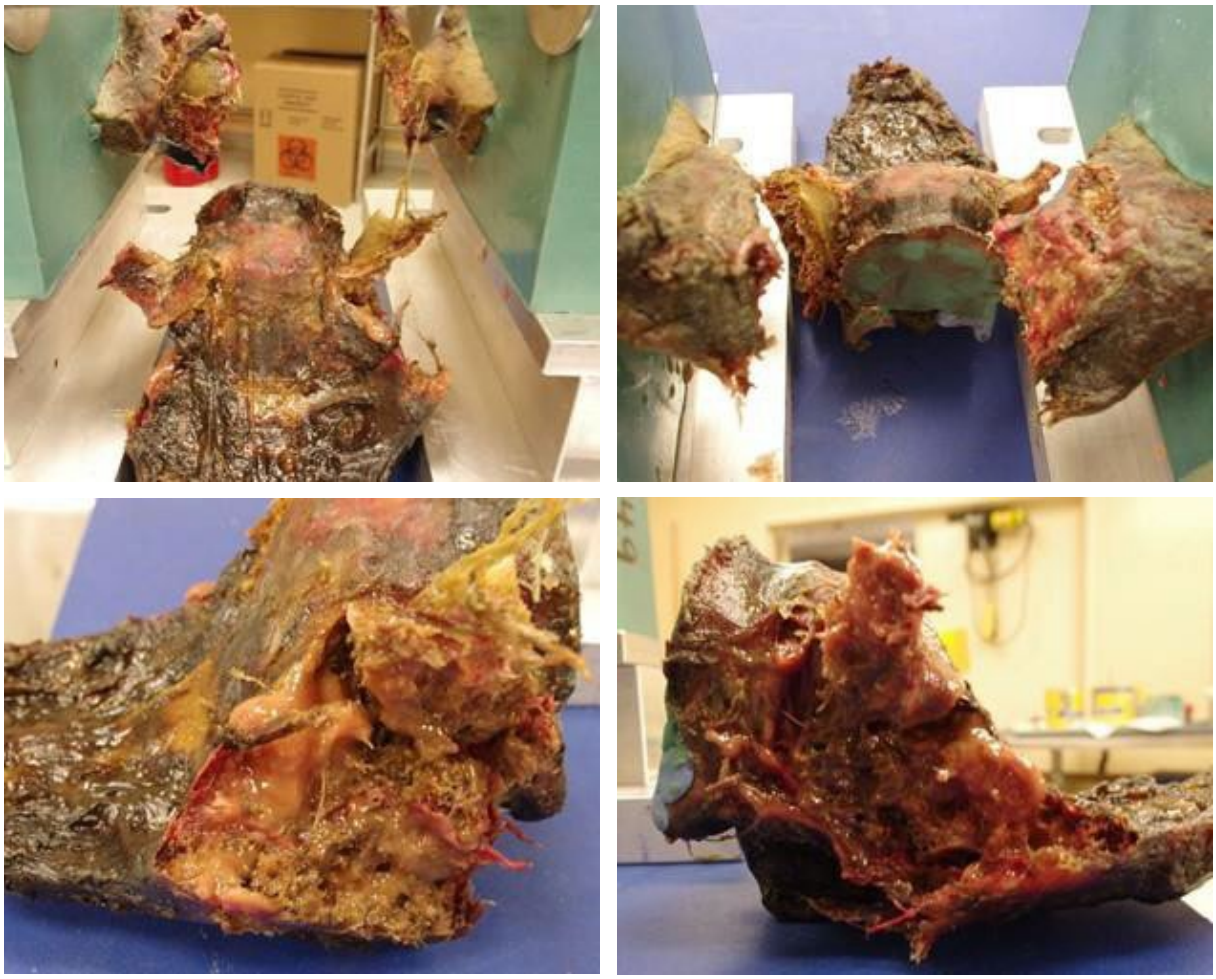

Figure E-4. Sacrum/pelvis damage for PMHS7849: Inferior pelvic perspective (top left), superior pelvic perspective (top right), left costal elements (bottom left), and right costal elements (bottom right)

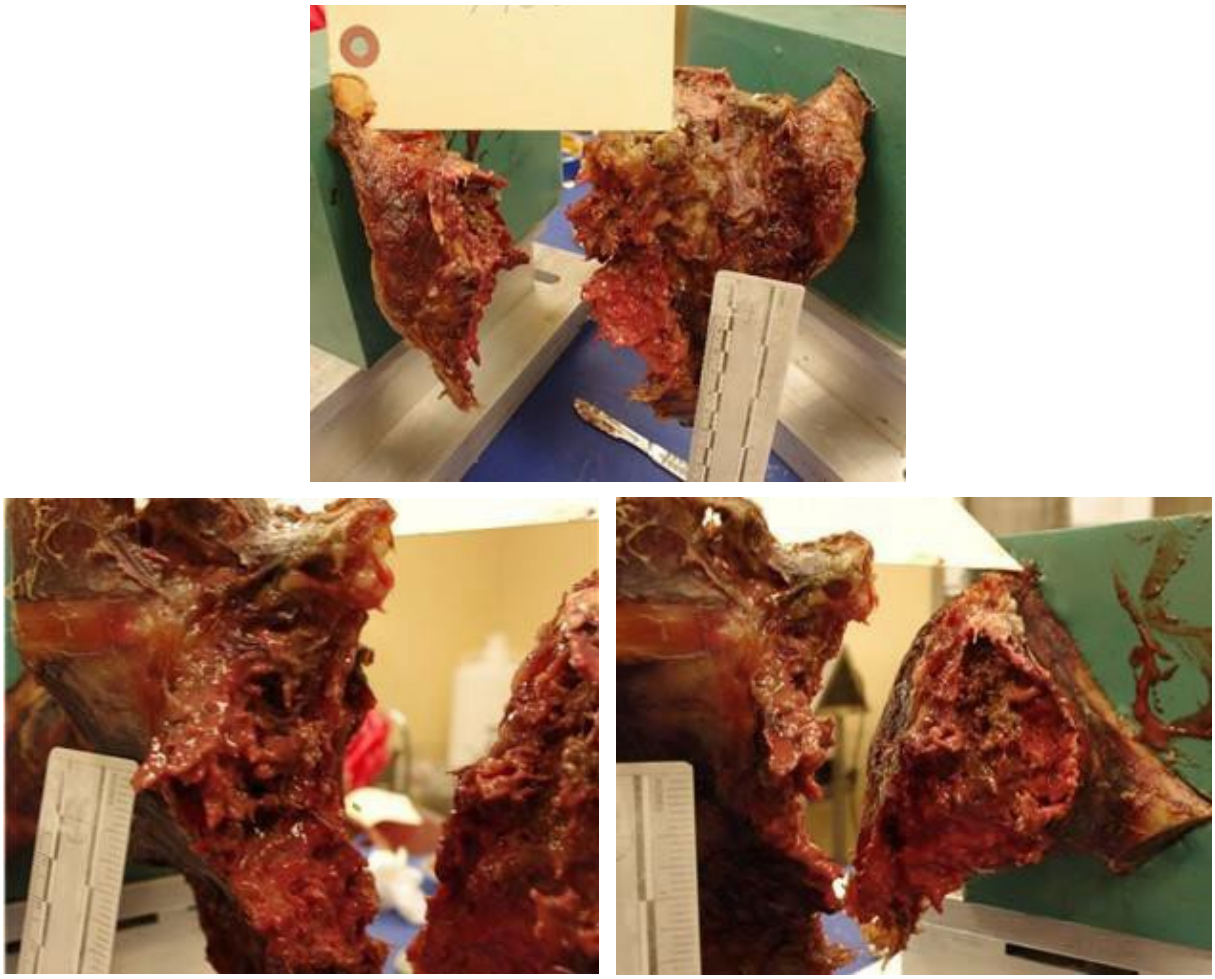

Figure E-5. Sacrum/pelvis damage for PMHS7406: Dorsal perspective (top), left costal elements (bottom left), and right costal elements (bottom right)

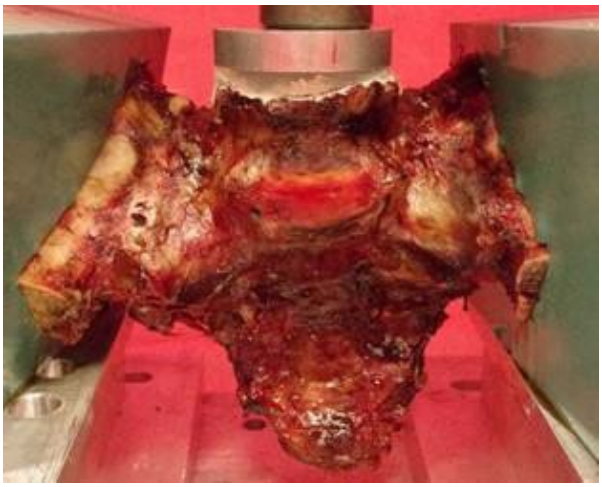

Figure E-6. PMHS7282 quasi-static loading to 5,160 N. Fracture of right alae.

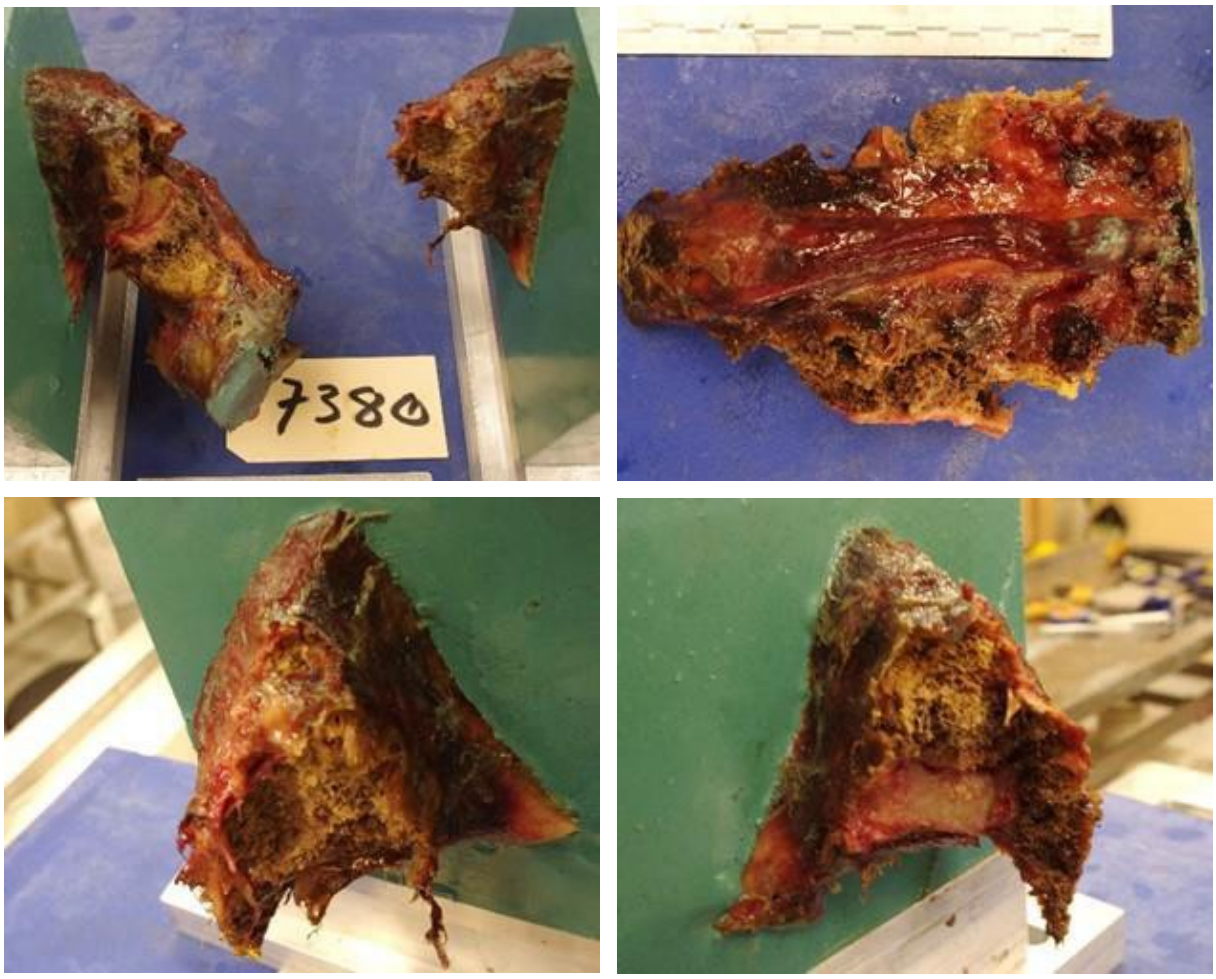

Figure E-7. Sacrum/pelvis damage for PMHS7380: Pelvic perspective (top left), dorsal sacrum perspective (top right), left costal elements (bottom left), and right costal elements (bottom right)

Figure E-8. Sacrum/pelvis damage for PMHS7618: Sacrum and ilium fragments (top left and right), left ilium (bottom left), and remaining potted right ilium (bottom right)

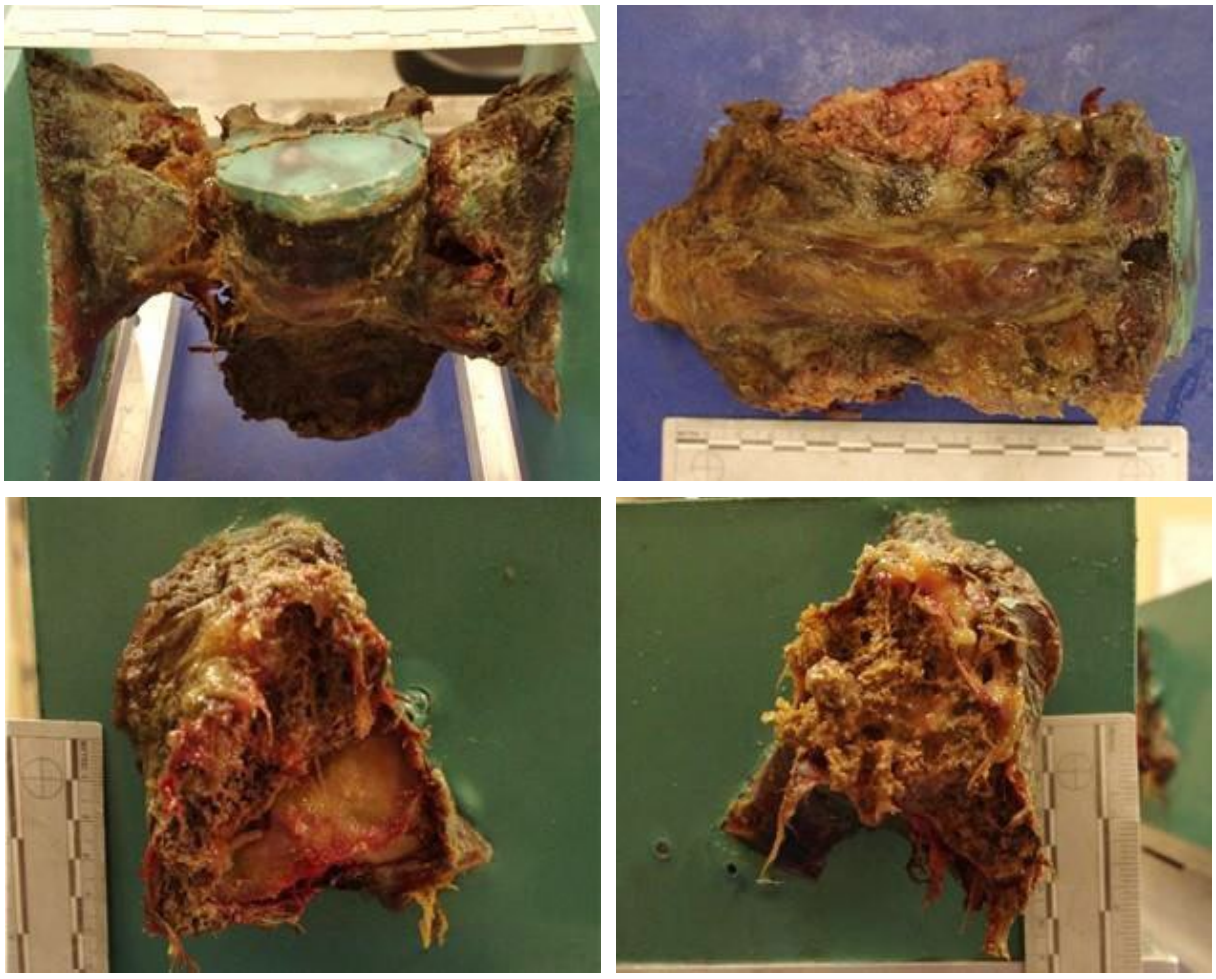

Figure E-9. Sacrum/pelvis damage for PMHS7834: Pelvic perspective (top left), dorsal sacrum perspective (top right), left costal elements (bottom left), and right costal elements (bottom right)

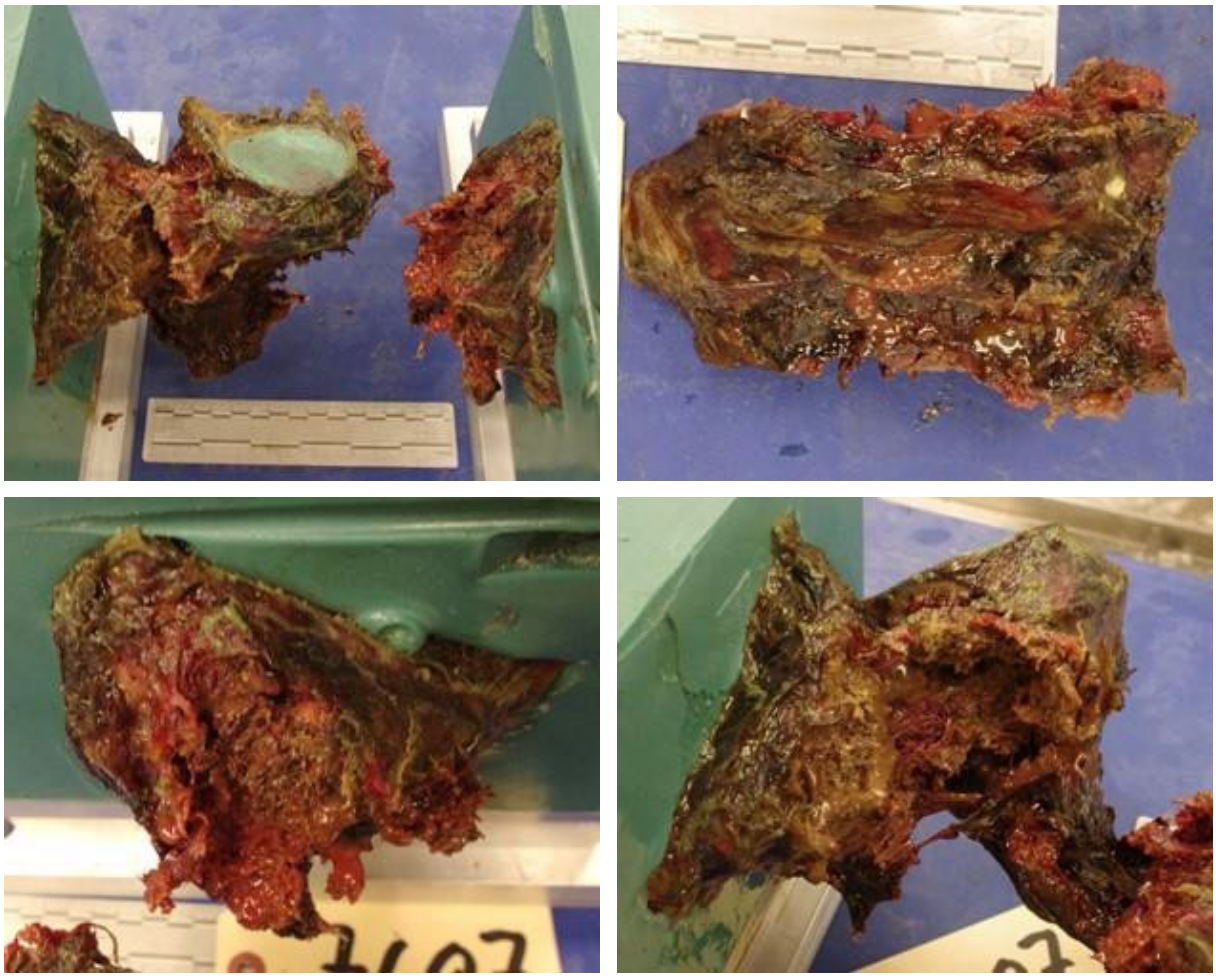

Figure E-10. Sacrum/pelvis damage for PMHS7607: Pelvic perspective (top left), dorsal sacrum perspective (top right), left costal elements (bottom left), and right costal elements (bottom right)

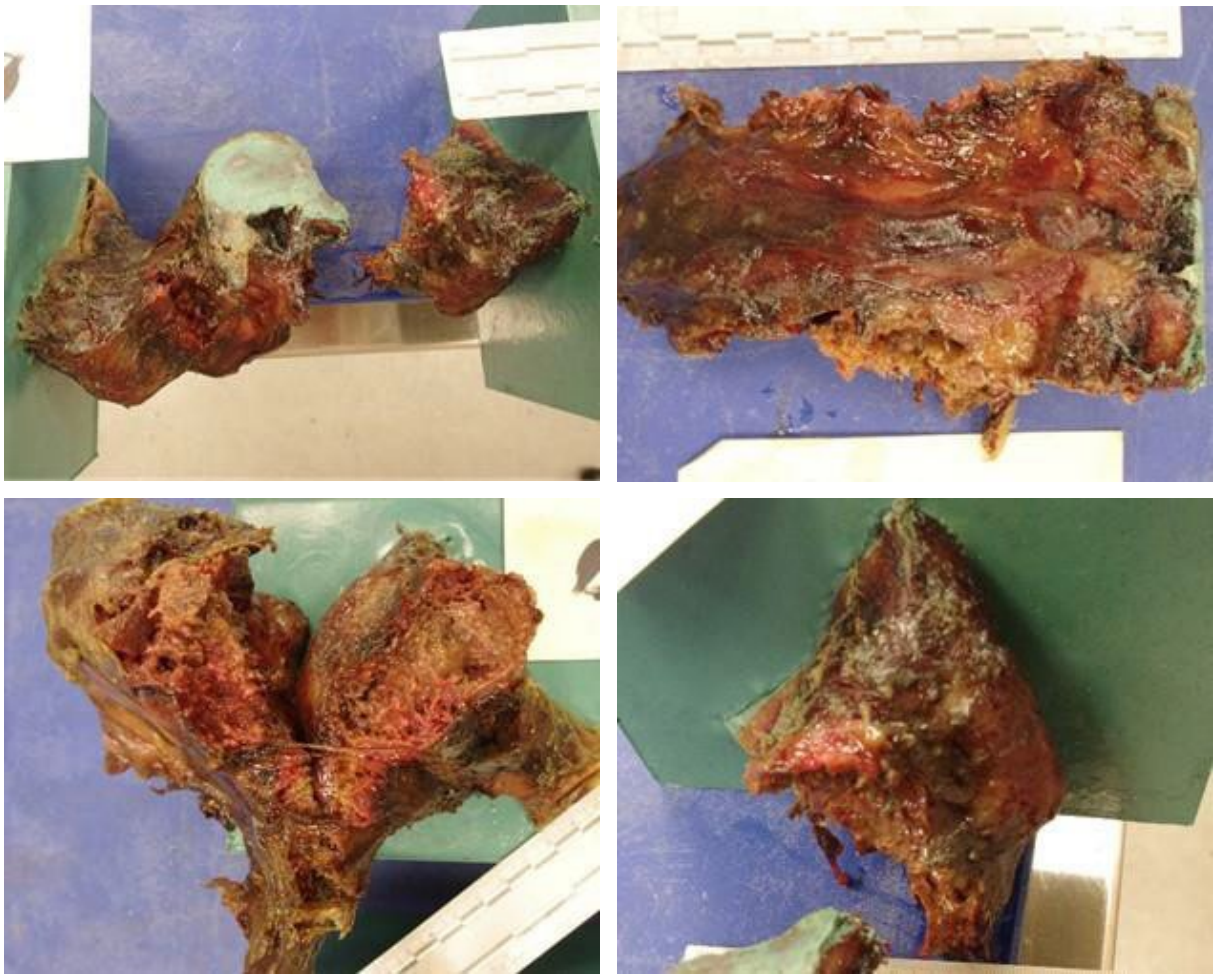

Figure E-11. Sacrum/pelvis damage for PMHS7630: Superior perspective (top left), dorsal sacrum perspective (top right), left costal elements (bottom left), and right costal elements (bottom right)

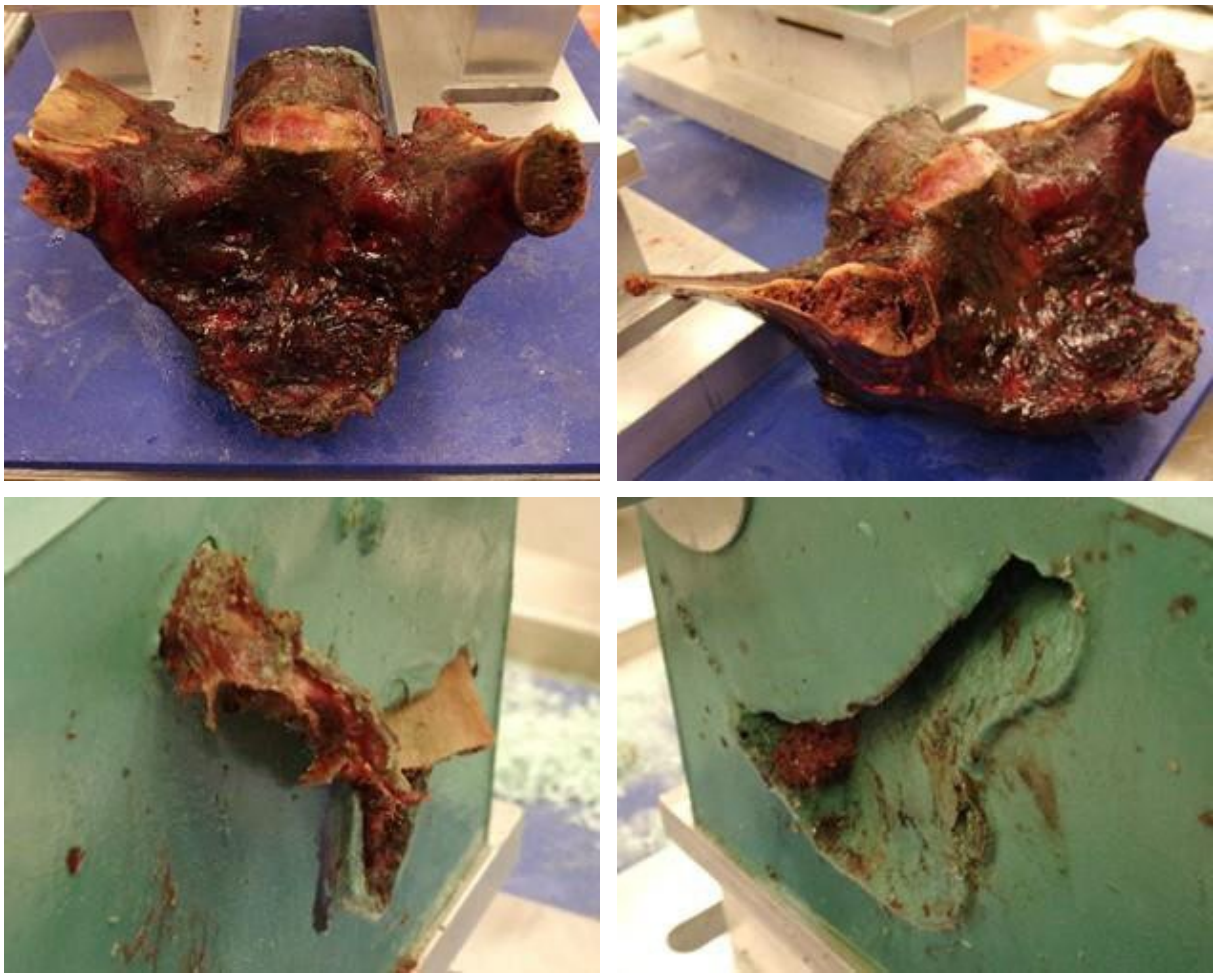

Figure E-12. Sacrum/pelvis damage for PMHS7727: Pelvic perspective (top left), oblique perspective (top right), left costal elements (bottom left), and remnants of right costal elements still potted (bottom right)

Figure E-13. Sacrum/pelvis damage for PMHSL7034: Pelvic perspective (top left), right sacral alae (top right), left sacral alae (bottom left), and right costal elements (bottom right)

LIST OF ACRONYMS

ANOVA	analysis of variance
APP3	Third Annual Program Plan
ATD	anthropomorphic test device
PMHS	postmortem human surrogate
TRR	Test Readiness Review
UBB	under-body blast
WIAMan	Warrior Injury Assessment Manikin

DISTRIBUTION LIST

DEVCOM Analysis Center
FCDD-DAG-S/K. Loftis
FCDD-DAG-S/M. Wassick
FCDD-DAG-S/D.R. Barnes
FCDD-DAG-S/K. Sandora
FCDD-DAG-S/G. Steiger
FCDD-DAG-S/B. Vanamburg
6896 Mauchly Street
Aberdeen Proving Ground, MD 21005

U.S. Army Evaluation Center
Survivability Evaluation Directorate
S. Swann
A Taylor
6617 Aberdeen Blvd.
Bldg 2202, 2nd Floor
Aberdeen Proving Ground, MD 21005-5071

U.S. Army DEVCOM Ground Vehicle Systems Center
FCDD-GVR-VMT/D. Weyland
FCDD-GVR-VMT/R. Scherer
6501 E. 11 Mile Rd
Detroit Arsenal, MI 48397-5000

Office of the Director, Operational Test and Evaluation
OSD DOT&E
LFT&E/J. Ivancik
1700 Defense Pentagon 1D548
Washington, DC 20301

DEVCOM Analysis Center
FCDD-DAD-TP/E. Chatterton
Redstone Arsenal
Huntsville, AL 35898

DEVCOM Army Research Laboratory
FCDD-RLB-CI/Tech Library
2800 Powder Mill Rd.
Adelphi, MD 20783

Defense Technical Information Center
ATTN: DTIC-O
8725 John J. Kingman Rd.
Fort Belvoir, VA 22060-6218